BLOOD FLOW SIMULATION USING SMOOTH PARTICLE HYDRODYNAMICS

Mohammed AL-SAAD

Ph.D. 2017

BLOOD FLOW SIMULATION USING SMOOTH PARTICLE HYDRODYNAMICS

Mohammed AL-SAAD

B.Sc., M.Sc.

(Mechanical Engineer)

Submitted for the degree of

Doctor of Philosophy

School of Engineering

Cardiff University, UK

2017

In the Name of God

the Most Compassionate and the Most Merciful

DECLARATION

This work has not been submitted in substance for any other degree or award at this or any other university or place of learning, nor is being submitted concurrently in candidature for any degree or other award.

Signed……(candidate) Date……

STATEMENT 1

This thesis is being submitted in partial fulfilment of the requirements for the degree of ……(insert MCh, MD, MPhil, PhD etc, as appropriate)

Signed……(candidate) Date……

STATEMENT 2

This thesis is the result of my own independent work/investigation, except where otherwise stated, and the thesis has not been edited by a third party beyond what is permitted by Cardiff University's Policy on the Use of Third Party Editors by Research Degree Students. Other sources are acknowledged by explicit references. The views expressed are my own.

Signed……(candidate) Date……

STATEMENT 3

I hereby give consent for my thesis, if accepted, to be available online in the University's Open Access repository and for inter-library loan, and for the title and summary to be made available to outside organisations.

Signed……(candidate) Date……

To my wife and my children

ACKNOWLEDGEMENT

It is a pleasure to be able to thank everyone who has inspired me and helped me on the journey of my doctoral studies.

Firstly, I would also like to thank my supervisor, Dr S. Kulasegaram and I would like to express every sincere appreciation and gratitude to him. He has always been helpful, and I am very grateful to him for our valuable discussions, his recommendations, and his advice during my research project. Without his help and his patience, I would not have been able to finish my doctoral thesis successfully. I have learned a lot from him.

I would like to express my great thanks and gratitude to my co-supervisor, Professor Boards. His kind advice and guidance during my thesis has been a constant source of inspiration. I am very grateful to him for sharing his valuable time and experience. He gave me the motivation and optimism to finish my studies.

Many thanks go to the staff at the Department of Mechanical Engineering for providing technical and administrative support throughout my PhD studies.

I would also like to thank Professor Saleh I. Najim and their whole family for their support and advise me.

I would like to acknowledge my government, as represented by the Ministry of Higher Education and Scientific Research, and the College of Engineering at the University of Basra who gave me this valuable opportunity to complete my PhD.

I am also grateful for my parents. They have also been a role model in my life. For giving their understanding and sacrifices throughout the years of my education, I cannot express enough gratitude. Although my father left me before this moment, I

believe that he has been and will continue to be my guiding light through life. I would also like to acknowledge my brothers and sisters for their support me during my PhD.

Finally, I am greatly indebted to my devoted wife Rawan for her support, encouragement, patience during my study and all the love of my children. They are the origin of my happiness. Their love and support, which has been given without any complaint or regret, has enabled me to complete this PhD. Rawan has constantly stood by my side throughout this journey; she has been my rock and my best friend.

ABSTRACT

Blood flow rheology is a complex phenomenon, and the study of blood flow in the human body system under normal and pathological conditions are considered to be of great importance in biomedical engineering. Consequently, it is important to identify the key parameters that influence the flow behaviour of blood. The characterisation of blood flow will also enable us to understand the flow parameters associated with physiological conditions such as atherosclerosis. Thrombosis plays a crucial role in stopping bleeding when a blood vessel is injured. Developing tools that can successfully study the influences of hemodynamics on thrombus formation in arteries and vessels are considered to be essential.

This thesis describes the steps taken to develop computational tools that focus on using the meshless particle-based Lagrangian numerical technique, which is named the smoothed particle hydrodynamic (SPH) method, to study the flow behaviour of blood and to explore flow condition that induces the formation of thrombus in blood vessels. A weakly-compressible SPH method is used here to simulate blood flow inside vessels. The basic governing equations solved in the SPH are the mass and momentum conservation equations. Due its simplicity and effectiveness, the SPH method is employed here to simulate the process of thrombogenesis under the influence of various blood flow parameters. In the present SPH simulation, blood is modelled by particles that have the characteristics of plasma and platelets. To simulate a 3-dimensional coagulation of platelets which form a thrombus, the adhesion and aggregation process of platelets are modelled by an effective inter-particle force model. With these models, platelet motion in the flowing blood and platelet adhesion and aggregation are effectively coupled with viscous blood flow. In this study, the adhesion and aggregation of blood particles are performed inside vessels with various geometries and with different flow velocity scenarios. The capabilities of this strategy were evaluated by comparing the simulation results with existing numerical and experimental results. All of these cases realistically model the formation of thrombus including thrombus collapse and partial separation. This thesis is considered to be the first work that is dedicated to the SPH simulation of thrombus formation inside blood vessels with various geometries and under different flow conditions.

PUBLICATIONS

1- **Al-SAAD, M.,** Kulasegaram, S., Bordas, S., (2017) Blood Flow Simulation Using Smooth Particle Hydrodynamics 3-Dimensional, Proceedings of the 25th UKACM Conference on Computational Mechanics, Birmingham, UK.

2- **Al-SAAD, M.,** Kulasegaram, S., Bordas, S., (2016). Blood Flow Simulation Using Smooth Particle Hydrodynamics **II**, ECCOMAS Congress 2016 VII European Congress on Computational Methods in Applied Sciences and Engineering. Greece.

3- **Al-SAAD, M.,** Kulasegaram, S., Bordas, S., (2016) Blood Flow Simulation Using Smooth Particle Hydrodynamics **I**, Proceedings of the 24th UK Conference of the Association for Computational Mechanics in Engineering. Cardiff, UK.

TABLE OF CONTENTS

LIST OF FIGURES

NOMENCLATURE

General information

- The following list of symbols is not considered detailed exhaustive. However, other symbols will be defined when required
- Most of the used symbols in the following sections are listed
- Meaning of symbols is given at least when introduced in the thesis
- Sometimes the same symbol is used to indicate different things
- Symbols for vectors and matrices are generally written in boldface

SYMBOSL

$\mathbf{n}$	Unit vector
h	Smoothing length
W	Weight function called *Smoothing function or Kernel*
V	Volume
N	Total number of particles
$\widetilde{W}$	Corrected Kernel function
$\widetilde{\nabla}$	Gradient correction
P	Pressure
ρ	Density
$\boldsymbol{d}$	Rate of Deformation
μ	Dynamic viscosity
t	Time
$\boldsymbol{\tau}$	Shear stress
$\mathbf{v}$	Velocity Vector
$\mathbf{x}$	Position vector
c_s	Speed sound
M	Mach number
v	Kinematic viscosity
B	Bulk modules
Δt	Numerical integration time step
Re	Reynold number
$\boldsymbol{F}_{ad}$	Adhesive force

$\boldsymbol{F}_{ag}$ Aggregate force

K Spring constant

r_o Natural length of spring

d_{ad} Adhesion area

d_{ag} Aggregation area

Δx Initial distance between particles in *x*-axis

Δy Initial distance between particles in *y*-axis

$\nabla \mathbf{v}$ Gradient velocity

T Temprature

$\rho_\circ$ Reference density

γ Power coefficient

∇ Vector operator

S Control surface

$\mathbf{F_s}$ Surface force

$\mathbf{F_b}$ Body forces

σ Total stress tensor

Ω Support domain

$\delta_{xx'}$ Dirac delta

m Mass

i Local particle

j Neighbouring particle

ACRONYMS AND ABBREVIATIONS

CFD	Computational fluid dynamic
SPH	Smoothed Particle Hydrodynamics
FD	Finite difference
FV	Finite volume
FE	Finite element
FEM	Finite element method
CEL	Couple Eulerian Lagrangian
ALE	Arbitrary Lagrange Eulerian
IBM	Immersed Boundary Method
CSM	Computational solid mechanics
MD	Molecular dynamic
MLS	Moving least square
EFG	Element free Galerkin method
SD	Stokesian dynamics method
PIC	Particle in cell method
DPD	Dissipative particle dynamics method
LGA	Lattice-gas automata
CFL	Courant–Friedrichs–Lewy condition
ISPH	Incompressible Smoothed Particle Hydrodynamics
B.C.	Boundary Conditions
PDE	Partial Differential Equation
WCSPH	Weakly-Compressible Smoothed Particle Hydrodynamics
ODEs	Ordinary differential equations
PDEs	Partial differential equations
PDF	Pair distribution function
ADT	Alternative tree

BD	Brownian dynamics
RHS	Right hand side
XSPH	Extended SPH
RBCs	Red blood cells
WBCs	White Blood cells
vWF	Von willebrand factor
hRBC	Height of Red blood cell
DRBC	Diameter of Red blood cell

Chapter 1

Introduction

1.1 Introduction

Various diseases can be considered as the major cause of human death worldwide. The cardiovascular is one of those diseases that leads to large number of fatalities every year. Basically, cardiovascular diseases (CVD) involve the heart and vessels in human body, in which heart attacks and strokes are considered as the most common accidents. Moreover, these diseases may occur without any symptoms and can cause sudden death.

Thrombosis has been proved, through various studies, as a major cause of CVD. Thrombosis may occur in different parts of human body. This might cause plug in the artery or vessel and restrict blood flow. Therefore, it is vital to understand the correlation between thrombus formation and hemodynamic to identify the causes of thrombosis.

A number of experimental and theoretical studies have been carried out to understand and to interpret the causes of thrombosis and to find how it is influenced by the haemodynamics of blood flow. To overcome the obstacles that may be encountered in an experimental study, numerous computational models have been introduced to investigate the process of thrombogenesis. The computational modelling of thrombus formation provides us with a wide range of tools that can be considered as non-invasive and more conducive for repetitive analysis.

Numerical simulations have significantly expanded our knowledge of physical phenomena in many areas including science and engineering. In comparison with analytical techniques, computational methods generally need less unrealistic assumptions and suppositions. Computational modelling is also considered to be a

good substitute for experimental studies, which are in most cases considered to be more expensive and time consuming. Consequently, numerical simulations have been widely used to uncover wide range of physical phenomena in many emerging fields of research.

Biomedical engineering is an emerging multidisciplinary field that integrates engineering and medical sciences. It involves several academic disciplines and professional specialisations, and it aims to develop better quality of healthcare diagnosis and methods of treatment. It combines the design and problem solving skills of engineering with medical and biological expertise.

The study of blood flow system under normal and pathological conditions is of great importance in the field of biomedical engineering. It is well-known that incessant blood circulation is very important for the healthy functioning of bodily organs. Therefore, hemodynamics is considered to be one of the major systems in the human body. It is, therefore, essential to develop tools that can successfully study the hemodynamic of arteries or blood vessels to investigate the hemodynamic complications encountered with cardiovascular diseases. In addition, the developed tools can explore alternative surgical procedures and evaluate their clinical impact on the hemodynamic condition of the patient. Furthermore, it can help one to understand any specific process associated with thrombosis and can raise the awareness of blood components involved in this process. At present, a large number of clinical researchers are forced to depend on personal experience and *in vitro* facilities.

It is, therefore, important to develop *in silico* tools that are capable of simulating hemodynamic of blood. Despite the significant improvements in computational methods and computer capabilities, solving these problems using conventional mesh-

based methods is complex. However, these methods have demonstrated good capabilities in simulating hemodynamic flows and have generated interesting results with considerable clinical and practical implications.

The main ingrained limitation of mesh-based methods is their dependence on the task of mesh generation. In addition, some important characteristics of hemodynamic flows, mainly under pathological conditions, are considered to be difficult to capture using mesh-based methods, including flow in complex geometries, tracking history of fluid properties, thrombus formation, the break-up of red blood cells (microcirculation) and so on. The simulation of such characteristics can be easily modelled with computational fluid dynamic (CFD) methods that are based on a Lagrangian approach instead of an Eulerian approach. Considering these facts, it is envisaged that simulating blood flow using Lagrangian meshless particle methods may alleviate a number of obstacles encountered by traditional mesh-based methods. As the name suggests, meshless methods do not require significant efforts with generation or regeneration of the mesh network or creation of connectivity between the nodes, which are challenging tasks in the case of flow domains with complex shapes.

Due to its simplicity and robustness, Smooth Particle Hydrodynamics (SPH), a fully Lagrangian mesh-free method, is chosen in this thesis to model blood flow simulation and thrombosis. SPH was originally used in astrophysical simulation in the late-1970s. Since the early-1990s, the SPH method was progressively used in modelling various engineering applications. The SPH method has several advantages, including a truly mesh-free nature, simplicity in handling complex geometries and it is naturally convenient for parallel computation.

In the SPH method, a continuum will be discretised into a set of particles. Each particle is assigned relevant individual physical properties. Numerical discretisation interpolates the value of a physical property for a given particle based on the properties of its neighbouring particles using an interpolating function. More details regarding the SPH method are provided in the later chapters.

1.2 Research Objectives

The aims of this thesis are as follows:

Traditional mesh-based methods generally encounter a number of obstacles in modelling flow process within complicated geometries due to their limitations associated with mesh generation. In contrast to mesh-based methods, the mesh-free or meshless methods can be easily used in discretising complicated geometries. Given that arteries and veins in human body have complicated geometries, meshless methods can serve as an efficient tool to model such complicated geometries. SPH is a true meshless method that is both robust and simple. The overall aim of this thesis is to explore the application of SPH method in simulating blood flow and thrombus formation. This research is primarily focused on developing suitable computational procedures to fully exploit the attractive properties of SPH method in modelling blood flow and thrombus formation. To achieve this overall objective, this research is subdivided into following tasks:

- To model the behaviour of the blood flow using SPH method and to investigate the accuracy of the employed numerical procedure.
- To study the influence of flow parameters for various flow conditions and vessel geometries.

- To investigate the applicability and efficiency of SPH method for modelling thrombus formation during blood flow inside vessels with different geometries.
- To assess the influence of various parameters, such as flow velocity and vessel geometry, on thrombus formation and separation.

1.3 Research Methodology

To achieve the above objectives, research is undertaken in the following stages:

- First, the relevant mathematical models and related governing equations to be adopted for the numerical simulation of blood flow were investigated.
- Second, a two–dimensional Lagrangian flow model, based on SPH method, was developed to understand the blood flow behaviour.
- Third, the developed code was validated in various flow simulation cases to explore the accuracy and stability of the numerical method.
- Fourth, the SPH blood flow model with thrombus formation algorithm was developed and evaluated using both two and three-dimensional flow test cases.

1.4 Outline of This Thesis

The work reported in this thesis mainly focuses on the SPH simulation of hemodynamic flows in arteries or vessels with various flow characteristics. A brief overview of the structure of this thesis is outlined below:

Chapter 2 presents a brief overview of properties and constituents of blood flow. A literature review on analytical and computational methodologies developed in the past for modelling blood flow is also provided in this chapter.

Chapter 3 highlights a suitable modelling strategy for blood flow simulations. In addition, SPH method is introduced in this chapter by providing the justifications for choosing the method in this work to simulate blood flow. The definition and mathematical formulations of SPH method are also presented.

Chapter 4 describes the fundamental governing equations to be used for numerical modelling. Moreover, this chapter details the SPH discretisation of the governing Navier-Stokes equations, time integration technique and the overall numerical procedure adopted.

Chapter 5 validates the accuracy of the numerical methodology developed in Chapter 4. Primarily, the accuracy and convergence characteristics of the proposed methodology is verified in standard numerical tests, which are generally used in computational fluid mechanics. Following these numerical experiments, the developed methodology is then applied to study the blood flow in human bifurcation artery. In this test, the results of the numerical simulations are compared with the experimental observations reported in literature.

Chapter 6 explores the feasibility of modelling the formation of thrombus using SPH method. First, the computational methods used in the past to model thrombus formation are highlighted. Next, a computational model which is adopted in the present work to simulate the thrombus formation is described. Finally, the results of

the numerical simulations are compared with experimental and numerical results reported in the literature.

Chapter 7 presents overall concluding remarks and points out possible future research directions for this work.

Chapter 2

Literature Review

2.1 Introduction

It is believed that the concept of circulation of blood was first described by William Harvey in 1628. A large number of researchers have since tried to understand the mechanism of blood circulation in the human body, and they have proposed numerous physical and mathematical models to study the blood flow phenomena. This chapter presents a brief overview of physiological characteristics of blood flow and thrombosis. In this section also provides a comparison between the computational mesh-based and mesh-free method. Finally, various mathematical models adopted in the past to understand and simulate blood flow and thrombosis are presented.

2.2 Characteristics of Blood flow

The circulatory system in the human body consists of a continuous circular network of blood vessels, the heart, and blood itself. William Harvey considered that the blood moves in a loop inside the human body (Harvey 1957). Blood flow in normal physiological conditions as well as in diseased conditions is an important field of study. Blood is a complex mixture of cells, proteins, lipoproteins, and ions which transports nutrients and wastes within the human body. In order to understand the behaviour of blood flow, it is essential to investigate the main role of blood in the human body. The circulatory or cardiovascular system circulates the blood in order to distribute oxygen (O_2), carbon dioxide (CO_2), nutrients, hormones etc. Oxygenated blood is transferred from the lungs to the tissues primarily via the arteries. Generally, there are three major types of blood vessels in the human body: the first type is called the arteries, which are part of the circulatory system, and their

task is to carry the blood away from the heart; the second is capillaries, which are the smallest of the blood vessels and are part of the microcirculation; and, the third is the veins. In addition, the arteries are further divided into smaller arterioles and then into the smallest blood vessels, the capillaries. The principal exchange of nutrients and oxygen from the blood to the tissues takes place in the capillaries. Thereafter, the primarily deoxygenated blood can be transferred from the capillaries to the venules, the veins, and in the last stage to the heart. The heart is considered to be the main part of the circulatory system and it pumps the blood around the body. In a healthy adult human, about 5 litres of blood are transported per minute through this process or over 7,000 litres per day. While the measurement of the diameter of the veins and arteries is in the cm to mm range, the arterioles and venules have diameters in the order of tens of μm, and the capillaries are only a few μm wide. Consequently, blood circulation in arterioles, venules and capillaries is called microcirculation (Pocock et al. 2013). Blood is mostly made of plasma, which amounts to about 55% of the blood volume and contains basically water (95% by volume). In addition, blood contains three types of so-called formed elements, red blood cells (RBCs), white blood cells (WBCs), and platelets (see Figure 2.1). Blood also includes proteins and other solutes (e.g., nutrients and hormones) (Pocock et al. 2013).

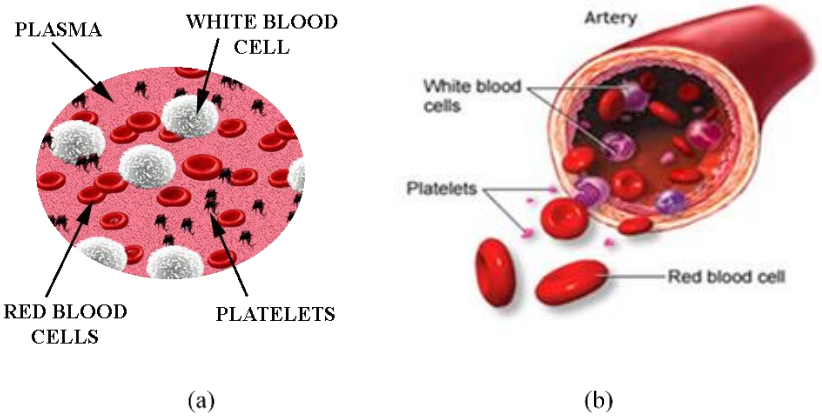

Figure 2.1 Blood elements: (a) blood cell (left), and (b) blood flow inside an artery (right)

RBCs, or erythrocytes, represent the majority of blood cells and account for about 5 × 10^6 per µl. The volume fraction of RBCs, called the haematocrit, is 37% to 54%, which varies between males and females, respectively (Pocock et al. 2013).

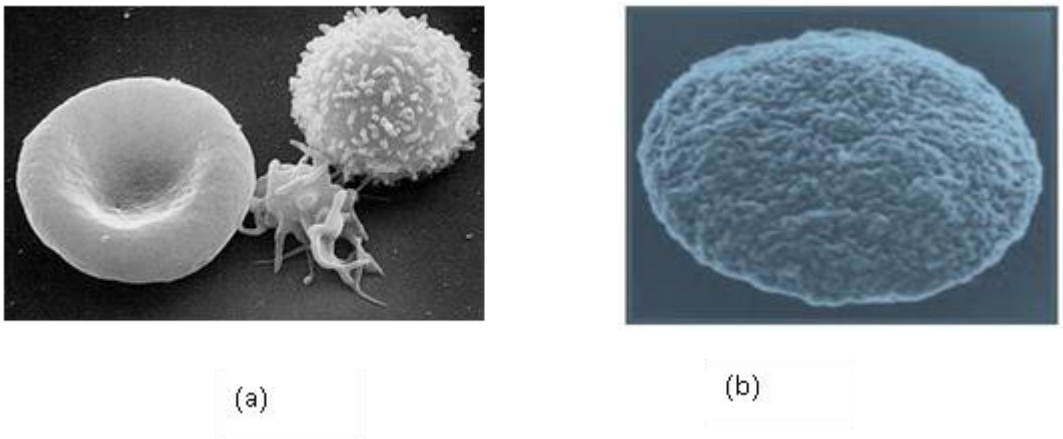

Figure 2.2 Scanning electron microscopy (EM) images of formed blood elements: (a) RBC (left), activated platelet (middle), and WBC (right) and (b) non-activated platelet. Source of the image (a): The National Cancer Institute at Frederick (NCI-Frederick). The image (b after (Michelson 2007) Copyright (2007)

RBCs are cells without a nucleus and they consist of water and haemoglobin, which gives blood its red colour. Normally, the RBCs are generated in the bone marrow and they remain in the blood for 100 to 200 days. Basically, RBCs transport O_2 from the lungs to the tissue and they then transfer part of the CO_2, a waste product from cell metabolism, back to the lungs. Their discocyte (biconcave disc-like) shape (see the EM image in Figure 2.2 (a)) is appropriate for the fast exchange of O_2, which is

performed by diffusion. The large surface area to volume ratio increases the speed of the O_2 uptake and release (Jones 1979; Vandegriff and Olson 1984). On average, the RBCs have 7.5 μm diameter and 2 μm height, which allows them to pass through the small capillaries, with a typical diameter of 5 μm to 8 μm. The elasticity of RBCs is considered to be one of their most important characteristics (Pocock et al. 2013). The viscous membrane of RBC basically consists of a lipid bilayer and a cytoskeleton, which is a network formed from spectrin proteins linked by short actin filaments to the inner monolayer (see Figure 2.3). The lipid bilayer is area preserving and the non-compressible inner cytosol is volume preserving. Because of the attached spectrin network and the lipid, the RBC membrane is considered to be a viscoelastic membrane (Fung 2013). WBCs, or leukocytes, represent about 7×10^3 per μl (Pocock et al. 2013). WBCs have a nucleus and are almost spherical, as shown in Figure 2.1 (a). WBCs vary in diameter vary from 6−20 μm, depending on the category. WBCs have the ability to recognise foreign substances and infectious agents, and are considered to be part of the immune system (Springer 1995; Pocock et al. 2013). As illustrated in Figure 2.1 (b), the platelet or thrombocyte is considered to be the smallest formed element in blood. The platelets are thin cellular fragments without a nucleus and with a disc-like shape. Their diameters vary between 2 μm and 4 μm and they possess a thickness of about 0.5 μm (Pocock et al. 2013). After platelets are produced from the megakaryocyte cell in the bone marrow, they can stay in the blood for a short period from 7 to 10 days. In addition to their outer membrane, they have an internal cytoskeleton, which is composed of polymers of actin and tubulin. In contrast to RBCs, platelets are stiffer (Michelson 2007; Zhao and Shaqfeh 2011). The average number of platelets in the human body is 150×10^3

− 400 × 10^3 per µl. The platelets are considered to be one of the most important elements for haemostasis (Broos et al. 2011; Nuyttens et al. 2011).

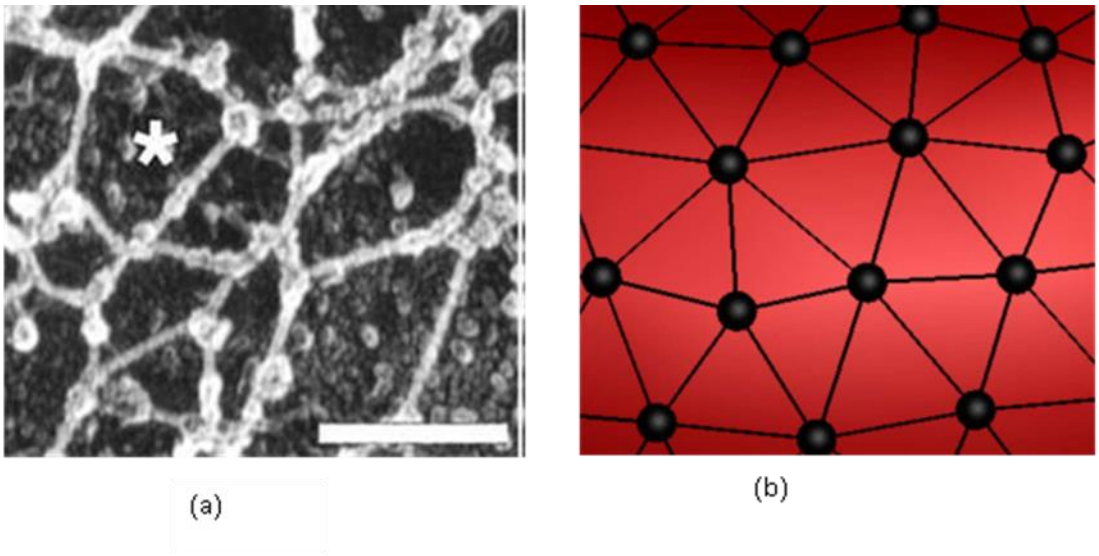

Figure 2.3 Illustration of a spectrin network. (a) Electron micrographs of RBC membrane skeleton from mice. The bar gives the reference length of 200 nm. (after ((Moyer et al. 2010). (b) Illustration of a spectrin network structure

A thrombosis is characterised as a pathological consequence of the normal haemostatic process, which leads to the formation of a thrombus in diseased vessels that prevents blood flow. A thrombus can be defined as a coagulated mass of blood corpuscles that stops bleeding or atherosclerosis in arteries. In other words, a thrombus can cause a blockage of blood vessels as a result of haemostasis dysfunction. Haemostasis is considered to be a necessary reaction to prevent and stop blood loss. However, malfunctioning of the haemostatic system can lead to potentially deadly accidents, such as myocardial infarction or ischemic stroke when the damaged arteries are the coronary or the carotids, respectively (Fuster et al. 1988; Epstein et al. 1992; Naylor et al. 2002).

There are two distinct types of thrombi. The first is called a red thrombosis and is found in areas with low shear rate and very low flow, usually in the veins (Bark Jr 2007). A coagulation cascade can be developed in these regions resulting in a

thrombus, which mostly consists of platelets and fibrin reticulum trapping many RBCs. A red thrombus is usually formed in the recirculation region of the vein valves. The name red thrombus is derived from the fact that it contains a significant amount of RBC in the thrombus. The second is called a white thrombosis and it occurs in areas with high shear rate, usually in the arteries (Bark Jr 2007). This type of thrombus can be formed under high shear stress, unlike red thrombus, and its constituents are densely packed. The contents of the white thrombus essentially consist of platelets, fibrin and plasma proteins. This is called a white thrombus because it contains very few RBCs. A thrombus is normally assumed as white thrombus when it is not classified. Meanwhile, a red thrombus is referred to as a coagulation (Bark Jr 2007).

In the normal condition of blood circulation, the platelets have no intent to adhere to the wall of the blood artery/vessels, to other cells, or to each other. In other words, they act as inert particles. The platelets or thrombocytes are considered to be the smallest formed element in blood. If the wall of a blood vessel is damaged, then platelets will rapidly adhere and accumulate on the damaged wall. Physiologically, this process of increase in the adhesiveness of platelets describes normal haemostasis. Pathologically, it may cause an acute thrombosis, particularly in larger arteries which are diseased but likewise in small arterioles which supply tissue grafts (Begent and Born 1970). The aggregation of platelets and blood coagulation is considered to be an intricate process (Panteleev et al. 2014). Haemostasis can be divided into three different phases. In the first stage, the vascular phase is aroused by damage in the blood vessel wall, which leads to smooth muscle contraction and this decreases the diameter of the vessel at the damaged area. The second stage is called the platelets phase, which starts when the platelets are attached to the damaged area

(see Figure 2.4 (a)) and is activated due to many factors, such as adenosine diphosphate (ADP) and tissue characteristics. The last stage is called the coagulation phase, which can begin 30 seconds or more after damage to the wall (Flannery 2005). A thrombosis is a disordered arrangement of platelets and plasma proteins. To understand the mechanism of thrombus formation inside the human body, development of thrombus is portrayed by three platelet deposition phases namely adhesion, activation, and collection Wootton and Ku (Wootton and Ku 1999). Furthermore, Wootton and Ku (Wootton and Ku 1999) reported that platelets deposition could be presented in three phases, as shown in Figure 2.4(b), based on an experimental study performed by (Markou et al. 1993).

There are many factors and biological conditions affect the process of thrombosis. For example, the local mechanics of flow can influence the process of thrombosis by affecting the diffusion of the materials in the blood which can disrupt the platelet aggregation and clotting and the supply of platelets and other cells to a site of thrombosis. Similarly, it was observed that hemodynamics could extremely affect the formation and growth of thrombus as well as thrombogenesis (Aarts et al. 1983; Cadroy and Hanson 1990; Reasor et al. 2013).

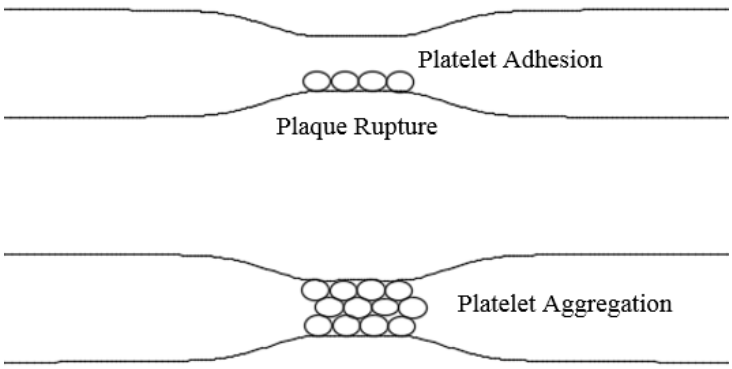

(a)

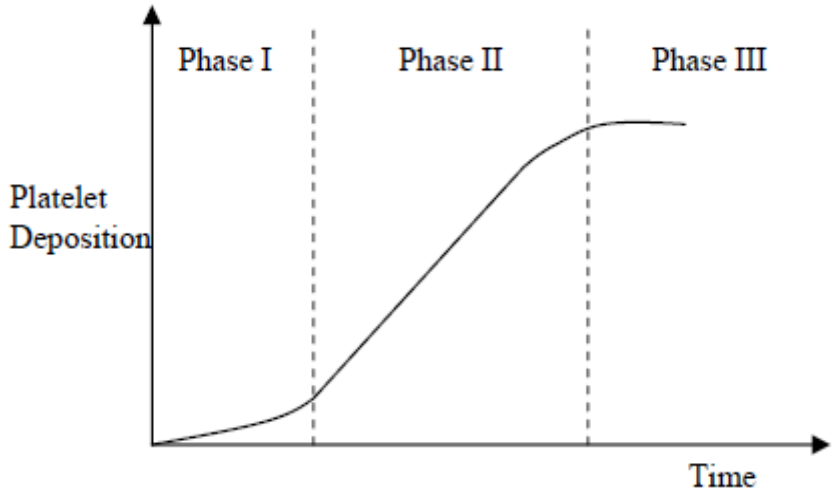

(b)

Figure 2.4 (a) Adhesion and platelet aggregation (b) Rate of platelet deposition characteristics (Markou et al. 1993)

Figure 2.5 (a) schematically describes the platelets adhesion, activation and aggregation phases and illustrates the dominating factors involved in thrombus formation. The platelets are activated under the agonists and shear stress. They are bounded by vWF and fibrinogen, in addition to more permanent binding to the vessel surface by vWF. Figure 2.5(b) shows agonist production from activated platelets.

As it can be noted from the description above, that the blood contains various elements in addition to so-called formed elements. A brief summary of factors involved in thrombus formation is presented above. However, for the purpose of conciseness, only the main and relevant elements are described in this chapter. More details on blood composition can be found in the plethora of literature (Bronzino 1999; Caro 2012; Fung 2013; Pocock et al. 2013).

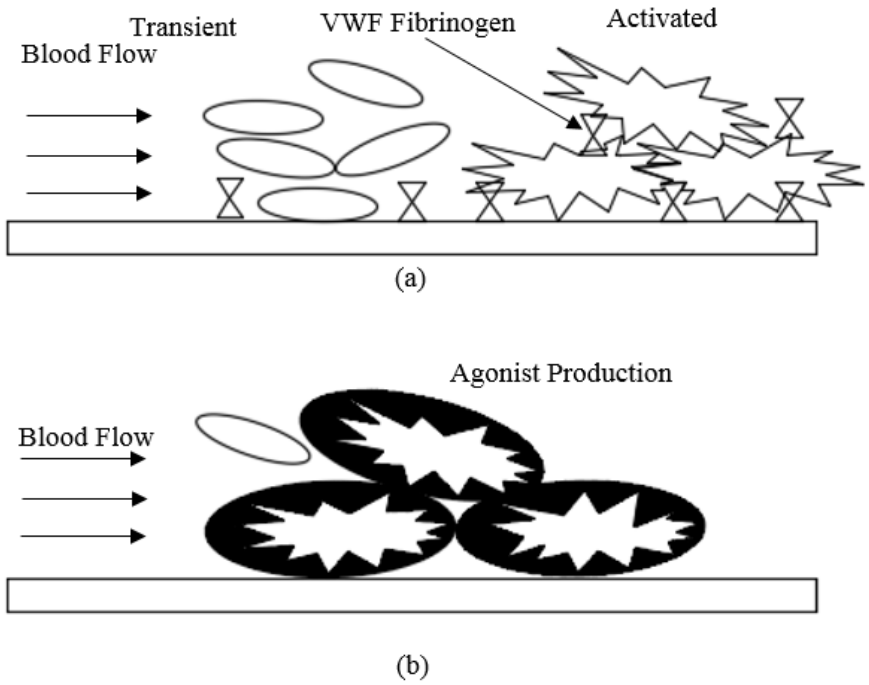

Figure 2.5 Diagram of platelet adhesion and aggregation (a) Platelet adhesion and aggregation vWF and fibrinogen attach to the collagen and activated platelets (b) Agonist production near activated platelets. Platelets entering the region can become activated

2.3 The Review of Existing Methodologies in Blood Flow Simulation

A vast amount of research has been focused on the study of understanding and measuring the characteristics of blood flow. At the eighteenth century, a mathematical model was applied by Bernoulli and Euler, which was the first attempt to describe the blood flow phenomenon. They proposed the idea of conservation of momentum and energy of blood flow. Euler tried to simulate blood as an incompressible and inviscid fluid through an elastic conduit. He used a mathematical model to simulate blood flow in an arterial segment. The pressure and flow wave transmission in the arterial system can be calculated by Euler's equations. However, he could not find a suitable close form solution (Stergiopulos 1990). Following that, an experimental investigation was performed by a French physician named J. L. M.

Poiseuille introduce one of the most famous equations in hemodynamics (fluid mechanics in general) which is known as Poiseuille's law, to calculate the pressure drop of blood through blood vessels and capillaries. Steady laminar flow through cylindrical and rigid conduits was proposed by Hagen and Poiseuille. In 1846, they developed Poiseuille's law, which was a well-known equation in hemodynamics and fluid mechanics, in general. Poiseuille's law states that:

$$\frac{\Delta p}{l} = \frac{8\mu}{\pi R^4} Q \tag{2.1}$$

where $\frac{\Delta p}{l}$ is the pressure drop over an arterial segment of length l, μ is the dynamic viscosity of the fluid, R is the internal radius of the artery, and Q is the volume rate of flow. Poiseuille's law was extensively used in the past to model blood flow. This provides an accurate model that relates mean pressure and flow values to the frictional resistance of the arterial segment. The effects of viscous resistance which was not addressed by the Euler equations (Stergiopulos 1990) were modelled by Poiseuille's law. The Navier-Stokes equations were introduced by Navier (1785-1822) and by Stokes (1819-1845), which were the most important equations of motion of a viscous fluid. These non-linear differential equations that are derived from the Navier-Stokes equations are written in, as follows:

$$\rho\left(\frac{\partial \mathbf{v}}{\partial t} + (\mathbf{v}.\nabla)\mathbf{v}\right) = -\nabla P + \nabla.\boldsymbol{\tau} + \mathbf{F}\,. \tag{2.2}$$

And along with the continuity equation,

$$\nabla.\mathbf{v} = 0 \tag{2.3}$$

In the above equations, ρ, t, $\mathbf{v}$, P, $\mathbf{F}$ and $\boldsymbol{\tau}$ represent the fluid particle density, time, velocity, pressure, external body force, and shear stress, respectively. The term $\mathbf{v}.\nabla$ is called the convective derivative which represents the physical term of the time rate of change where the fluid element moves from one place to another in the flow field.

In the general case of arterial flow the non-linear form of the Navier-Stokes equations is applied. Researchers then simplified the assumptions of the Navier-Stokes equations to obtain analytic solutions for reduced forms of the Navier-Stokes equations (Stergiopulos 1990).

The first endeavours to model flow in blood vessels were made during the 1950s. The equation of viscous, laminar flow of a Newtonian and incompressible fluid within a long and circular pipe was solved by Womersley (Womersley 1955). Where, he calculated the flow rate and velocity in arteries which were based on using the gradient pressure that was developed by Hale et al. (Hale et al. 1955), which used Fourier series to obtain the velocity profile. Hypotheses that were adopted in this study assumed large arteries as rigid circular tubes and introduced periodic pressure gradient to obtain pulse wave velocity. The wall distensibility was used in the same model (Womersley 1957) to describe a thin, uniform, and linearly elastic wall. A two-dimensional and straight sided model of the trifurcation to study the flow in renal arteries was reported by O'Brien and Ehrlich . (O'Brien and Ehrlich 1977). While a linear form of the Navier-Stocks equation was used by Avolio (Avolio 1980), who used a multi-branched model in a human arterial system to model wave propagation in arteries. He made a very good advancement in this work (Avolio 1980) when he compared it with previous studies performed by other researchers (Noordergraaf et al. 1963; Westerhof and Noordergraaf 1970).

Numerical simulations were also used in the past to describe the behaviour of blood flow under both normal and pathological conditions. Many researchers tried to develop a perfect method to simulate blood flow. For example, a study of pulsatile flow in elastic arteries with one-dimensional wave propagation was reported by Reuderink et al. (Reuderink et al. 1989), who used linear and non-linear theory in blood vessels. The results obtained were compared with the experimental data. Their linear model was found to be more convenient and was able to compute the damping of the waves. Meanwhile, the non-linear term used in the formulation was proved not to be very beneficial. In addition, a number of clinically relevant models were qualitatively and quantitatively estimated the blood flow field using the Finite Element Method (FEM) models developed by Taylor et al. (Taylor et al. 1998a, b). In these models, it was found that the velocity profiles could be acquired under resting and exercise conditions.

Pries et al. (Pries et al. 1990) developed a theoretical model to simulate blood flow and tested it through a large microcirculatory network, which assessed the consistency of viscosity of blood flow in vessel diameter and haematocrit (i.e. the ratio of the volume of RBCs to the total volume of blood). Following that, a numerical study was presented by Henry and Collins (Henry and Collins 1993) to create a general model for the flow in large arterial vessels. They focused on modelling artificial ventricles and included the effect of wall distensibility of blood vessels. They fixed the values of pressure at a certain value and compared their results with an analytical solution.

At the same period, Fung (Fung 1993) described the phenomenon of atherosclerosis by reducing arterial lumen size through plaque formation and arterial wall

thickening, which occurs at specific arterial sites. This is related to hemodynamics and to wall shear stress (WSS) distribution. Perktold and Rappitsch (Perktold and Rappitsch 1995) examined the effect of the distensible artery wall and calculated the mechanical stresses within it using a theoretical procedure based on FEM. This method uses three-dimensional framework with an incompressible and non-Newtonian fluid model. The aim of this work was to use a numerical method to determine the influence of the principle stresses in the artery and to simulate pulsatile flow in a carotid bifurcation. A numerical analysis for an axisymmetric domain was presented by Rappitsch and Perktold (Rappitsch and Perktold 1996) to describe the impact of flow patterns, such as WSS and reversed flow on the mass transport. Meanwhile, Steinman et al. (Steinman et al. 1996) observed a good agreement between measurement of blood velocity profile by magnetic resonance imaging (MRI) and numerical simulation performed from their study. After that, Ku (Ku 1997) showed that the RBCs were small and semisolid particles that can increase the viscosity of blood, which in turn can influence the behaviour of the blood flow. He observed that the viscosity of blood can be approximately equal to four times that of viscosity of water. Furthermore, blood can appear as a non-Newtonian fluid in the microcirculatory system because the viscosity of blood is not constant at all flow rates. The blood in small branches and capillaries are considered to behave as a non-Newtonian fluid. Meanwhile, blood is shown to behave as Newtonian fluid in most arteries (Ku 1997). Bathe and Kamm (Bathe and Kamm 1999) modelled pulsatile flow in stenotic arteries by using an iterative method over each time step. They used stenosis with varying degrees (i.e. various sizes and shapes) within arteries for their study. They concluded that the pressure drop across stenosis of the artery would depend on the severity of stenosis. Nevertheless, some studies in the past focused on

the influence of non-Newtonian properties of blood flow in large arteries. For example, Gijsen et al. (Gijsen et al. 1999) studied the influence of shear thinning on the velocity distribution by using laser Doppler anemometry experiments and FE simulation of steady flow in a three-dimensional model of the carotid bifurcation. However, properties such as the viscoelasticity of blood were overlooked in this study. Gijsen et al. (Gijsen et al. 1999) concluded that there was a high level of agreement in observed velocity profiles for both Newtonian and non-Newtonian fluids. The hemodynamic in a carotid bifurcation was further investigated by Botnar et al. (Botnar et al. 2000), who compared numerical simulation and in *vitro* MRI measurements. This study demonstrated the importance of numerical simulations to predict complex flow behaviour in vessels where atherosclerotic plaques may form. In recent years, there have been a significant amount of three-dimensional studies performed to investigate blood flow behaviour. For instance, the relationship between the fluid forces acting on walls and development of intimal thickening in grafts was investigated in blood vessel by a number of researchers (Hofer et al. 1996; Keynton et al. 2001; Loth et al. 2002; Giordana et al. 2005). Normally, blood flow is classified as a laminar flow but due to some specific physiological conditions, a part of the cardiac cycle can produce blood flow of turbulent nature. He and Jackson (He and Jackson 2000) focused on this type of flow and demonstrated that turbulence power is reduced in accelerating phases and is increased in decelerating phases of the cardiac cycle, which is mainly associated with the radial propagation of turbulence. In addition, Darbeau et al. (Darbeau et al. 2000; Stangeby and Ethier 2002) tried to interpret deposit formation in terms of local WSS variations by analysing the transport and accumulation of macromolecules.

In recent years, computational methods have been increasingly applied to predict the blood flows in vessels. Initial computational methods were mostly limited to one or two-dimensional models. The transition to three-dimensions was needed to know the capability of computational hardware which had ability to understand the problems more than two-dimensions. An approach to mix between one-dimensional and three-dimensional models of blood flow were reported by Formaggia et al. (Formaggia et al. 2001, 2002). The influence of Newtonian fluid and non-planarity of an arterial bifurcation on the flow and WSS was studied by Lu et al. (Lu et al. 2002). They concluded from this study that haemodynamic within the vessel considered above was useful in vascular biology and pathobiology. Taylor et al. (Taylor et al. 2002) presented an investigation on exercise, which was considered as one of the most important mechanisms to increase blood flow and WSS, and which could protect from atherosclerosis. Lee and Chen (Lee and Chen 2002) used a different way to simulate the flow in the abdominal aorta and its peripheral based on the finite volume method (FVM). Meanwhile, Dzwinel et al. (Dzwinel et al. 2003) focused their research more specifically on the properties of blood. Some numerical studies also examined the turbulent flow in a stenosed pipe to predict the flow profile in the stenosis region. For instance, Varghese and Frankel (Varghese and Frankel 2003) used a numerical study to analyse the pulsatile turbulent flow in the rigid wall of a stenosed tube. The authors investigated the influence of stenosis on WSS values at both upstream and downstream of the stenosis.

Grotberg and Jensen (Grotberg and Jensen 2004) found that arterial wall deformation can be governed by WSS; such that arteries enlarge in response to high shear stress. It can be concluded that the formation of atherosclerotic plaques was especially limited to the locales of low shear stresses but not in the regions of higher

shear stresses. Therefore, decreased shear stress induces intimal thickening in vessels which have adapted to high flow. In addition, Chen and Lu (Chen and Lu 2004) performed a similar analysis for non- Newtonian fluid and non-planarity by using FEM in a three-dimensional model. Modelling of arterial wall to examine the relationship between arterial wall stress and vessel wall diseases (Tafazzoli-Shadpour 1999; Matsumoto et al. 2004) was another important topic of research in the past. In another study that was performed to describe the characteristics of blood flow, Yokoi et al.(Yokoi et al. 2005) used a numerical algorithm to compute flows in blood vessels with complex geometries. An algorithm based on regular Cartesian grid was proposed in this study. The results showed that the flows in complex geometries, such as a bifurcation and multiple aneurysms, could be dealt with by this method. Tsubota et al. (Tsubota et al. 2006) compared the geometry of the pulsatile flow and steady flow, and analysed the motion of a deformable RBC in flowing blood plasma. For this study, they used a mesh-free technique named moving particle semi-implicit method (MPS). The purpose of this study was to describe the motion of a deformable RBC and its interaction with blood flow by using a particle method for blood flow simulation. In this study, a two-dimensional simulation of blood flow between parallel plates was performed. Meanwhile, other researchers have used the Lattice Boltzmann method to achieve a suitable accuracy in a human abdominal aorta such as Artoli et al. (Artoli et al. 2006).

A large number of studies have tried to understand the major cause for atherosclerosis in the human body. For example, some researchers (Bharadvaj et al. 1982; Zarins et al. 1983; Gnasso et al. 1997) presented a study to examine the relationship between plaque location and WSS by analysing blood flow. Meanwhile, efforts were also made to calculate the circumferential stress distribution in

atherosclerotic vessels, which concentrated on correlation between maximal stress and plaque rupture (Tang et al. 2005; Baldewsing et al. 2006). A simulation model with realistic boundary conditions in vessels with different degrees of stenosis was explored by Li et al. (Li et al. 2007) , using fluid-structure interaction (FSI) and a turbulent model. Carneiro et al. (Carneiro et al. 2008) presented a numerical study that calculated the effect of blood properties in the abdominal aorta bifurcation. They believed that their study play an important role in the atherosclerosis lesions. Some studies were also performed to investigate blood flow in different parts of the human body. For example, Bernsdorf and Wang (Bernsdorf and Wang 2009) simulated the blood flow in cerebral aneurysms in domains created from medical image. The objective of this research was to perform an accurate numerical simulation of flow properties, particularly the difference in WSS between Newtonian and non-Newtonian fluids. Additionally, a three-dimensional FE simulation was developed by Kim et al. (Kim et al. 2010) that predicts blood flow in epicardial coronary artery. They discovered that their research could be useful in predicting cardiovascular diseases. While, Obidowski and Jozwik (Obidowski and Jozwik 2010) compared the computer simulation results of the hydrodynamics of blood flow through three different kinds of vertebral artery geometries with ultrasonography measurements to obtain a better insight into the flow behaviour. Their study showed that a good agreement for results obtained in the central region of the artery.

A parallel two-level method for simulating blood flows in branching arteries with the resistive boundary condition was introduced by Wu and Cai (Wu and Cai 2011). Notably, the zero-traction outflow boundary condition was enhanced by the presence of a resistive boundary condition. This was further examined in a report on the simulation of blood flow using subject-specific geometry and spatial varying wall

properties by Xiong et al. (Xiong et al. 2011), who investigated image segmentation dealing with braces, including a deformable model and the level set method. In their study, Xiong et al. (Xiong et al. 2011) applied an idealised cylindrical model and two subject-specific vascular models with thoracic and cerebral aneurysms. The results from this study demonstrated the possibility of obtaining blood properties in deformable models.

According to a numerical study by Sousa et al. (Sousa et al. 2012), some enhancements of blood flow were achieved by using bypass systems with different geometries. Further, Montecinos et al. (Montecinos et al. 2014) modelled blood flow in vessels with walls having viscoelastic properties and solved a time dependent, one-dimension system. Additionally, Chnafa et al. (Chnafa et al. 2014) computed a human-specific left heart flow using a numerical framework which described the blood flow by its transition nature to generate a complex cyclic flow.

Reorowicz et al. (Reorowicz et al. 2014) improved the modelling of blood flow based on computer tomography images. Their objective was to analyse the hydrodynamics of blood flow in cerebral region, or Circle of Willis (COW), using three different patient-specific artery anatomies. In this study, the physicians diagnosed patients of different ages and various anatomical arterial structures.

In the past, a number of different approaches were used to analyse blood flow. Many researchers studied the flows of fluids in tubes of more complex sections while only a few studies considered multilayer flows in rectilinear and circular tubes of various cross-sections. Khomasuridze and Zirakashvili (Khomasuridze and Zirakashvili 2015) considered stationary multilayer flows of a viscous incompressible fluid in tubes. The results of this study demonstrated that the model was able to determine

the critical parameters in micro vessels which are caused by friction, such as: liquid viscosity (more exactly, apparent viscosity), dynamical haematocrit, and resistance force. Jahangiri et al. (Jahangiri et al. 2015) concentrated on the turbulent pulsatile blood flow through stenosed arteries considering the elastic property of the wall. Their results were compared with experimental data and they showed that the flow was laminar up to 70% stenosis, while for 80% stenosis the flow became turbulent. Nevertheless, Marth and Voigt .(Marth and Voigt 2015) reported a numerical study that investigated the margination of WBCs. In this study, Marth and Voigt .(Marth and Voigt 2015) dealt with a mesoscopic hydrodynamic Helfrich-type model and found that the margination of WBCs was less significant with increasing Reynolds number of the flow.

It is also worth noting other research work carried out using computational modelling to investigate blood flow in bio-mechanical systems (Peskin 1977; Cho and Kensey 1991; Chen and Lu 2004; Johnston et al. 2004; Morris et al. 2005; Duraiswamy et al. 2007; Mukundakrishnan et al. 2008; Sultanov and Guster 2008; Sultanov et al. 2008; Sultanov and Guster 2009; Nithiarasu 2016; Shi et al. 2017).

This section has attempted to provide an overview of various methodologies adopted for modelling blood flow in general. As one of the aims of this thesis is to model thrombus formation, the next section intends to provide a literature review on the simulation of thrombus formation. The next section will serve as a preamble for the novel numerical techniques to be introduced in Chapter 6 to perform numerical simulation of thrombus formation in this thesis.

2.4 The Simulation of Thrombus

As discussed above thrombogenesis plays a crucial role in human physiological condition which occurs in blood vessels according to certain mechanical and chemical stimuli and it is vital to understand how thrombus formation is related to hemodynamic. There are a wide variety of computational models that have been used in the past to simulate and investigate the process of thrombogenesis.

Many Eulerian based studies (Stubley et al. 1987; Eckstein and Belgacem 1991; Sorensen et al. 1999; Woodside et al. 2001; Goodman et al. 2005) have analysed the role of a hemodynamics in thrombogenesis. However, capabilities of these studies were limited and not adequate to fully describe platelets motion and their behaviour. A continuum model of platelet aggregation to analyse platelet-mediated thrombogenesis, while considering platelet transport activation by a single lumped agonist and bulk aggregation, was introduced in Fogelson (Fogelson 1992), which was extended in (Fogelson 1993) by introducing the capability for modelling multiple platelet agonists as described by (Stubley et al. 1987; Eckstein and Belgacem 1991; Sorensen et al. 1999; Woodside et al. 2001; Goodman et al. 2005). Moreover, Merten et al. (Merten et al. 2000) used a Lagrangian descriptions to investigate and demonstrate how platelets are adapted and activated. Meanwhile, Kuharsky and Fogelson (Kuharsky and Fogelson 2001) presented a model which takes into account plasma-phase, subendothelial-bound and platelet-bound enzymes and zymogens as well as activated and unactivated platelets. They considered the physical and chemical process associated with platelet motion and coagulation events that occur in a thin layer called the reaction zone, and its location just above a small vascular injury. A numerical study which is based on combining the discrete element

method (DEM) and Stokesian dynamics method (SDM) was presented by Miyazaki and Yamaguchi (Miyazaki and Yamaguchi 2002) to analyse the mechanism of platelet adhesion. Tamagawa and Matsuo (Tamagawa and Matsuo 2004; Ouared and Chopard 2005) used a Lattice Boltzmann method to model red thrombus formation that depended on transport phenomenon which can be used to deal with shear stress dependent thrombogenesis probability. Ding and Aidun (Ding and Aidun 2006) used the Lattice Boltzmann method to model red cell motion, including the formation and degradation of particle clusters. A three-dimensional thrombus formation model was introduced by Pivkin et al.(Pivkin et al. 2006), who treated each platelet as a spherical object and the suspension of RBCs was treated as a continuum. Meanwhile, Immersed-boundary-type models were reported in Fogelson and Guy (Fogelson and Guy 2008) to demonstrate the effect of thrombus development on the flow and the influence of fluid forces on thrombus growth. A study presented in Xu et al. (Xu et al. 2008) set out to explain the blood flow influenced platelet aggregation and the size/geometry of the thrombus using two-dimensional multi-scale model. Mori et al. (Mori et al. 2008) used Stokesian dynamics to deal with the effect of RBCs on thrombus formation. Leiderman Gregg and Fogelson (Leiderman Gregg and Fogelson 2009) presented a spatial-temporal model which coupled partial differential equations to describe multiple spatial and temporal processes, including coagulation biochemistry. The motivation behind this model was to investigate how the impact of the wall shear rate and near-wall enhanced platelet concentration affect the growing thrombi.

Recently, a new class of Lagrangian technique called particle-based methods were developed to investigate the behaviour of corpuscles and their interactions in blood flow (Boryczko et al. 2003; Filipovic et al. 2008). A mechanical model is proposed

in Filipovic et al. (Filipovic et al. 2008) that uses the dissipative particle dynamics (DPD) method to demonstrate the accumulation of platelets and their behaviour in blood flow. Meanwhile Kamada et al. (Kamada et al. 2010; Kamada et al. 2011) used a particle-based technique described as moving particle semi-implicit (MPS) method to simulate the formation of thrombogenesis in both two and three-dimensional settings. Fogelson and Neeves (Fogelson and Neeves 2015) presented an overview to describe the thrombus stability and factors regulating the hindered transport through thrombus.

Researchers showed the presence of stenosis, stent, and grafts plays an important role in the thrombus formation. They found through the experimental and numerical examinations of platelet deposition in stenosed vessels that normally the highest level of platelet accumulation exists near the stenosis apex (Ku et al. 1985; Lassila et al. 1990; Strony et al. 1993; Mailhac et al. 1994; Siljander and Lassila 1999; Wootton and Ku 1999; Goodman et al. 2000; Longest and Kleinstreuer 2003; Liu et al. 2008; Bark et al. 2012; Bark and Ku 2013; Para and Ku 2013; Casa and Ku 2014; Stiehm et al. 2016).

In summary, this literature review demonstrates the importance of numerical simulation of thrombus formation and various techniques used in the past to overcome the difficulties associated with accurate modelling of such processes. Hence, this study proposes to use meshless particle-based Lagrangian numerical technique, named the smoothed particles hydrodynamic (SPH) method to study the flow behaviour of blood and to explore the flow condition that induces the formation of thrombus in a blood vessel. Due to its simplicity and effectiveness, SPH has been chosen as a better alternative to simulate blood flow and thrombus formation. As a

Lagrangian particle-based method, SPH can provide a number of advantages in modelling including ease of point generation (i.e. mesh generation) for complicated geometries.

2.5 Concluding Remarks

This chapter has provided an overview on the properties of blood and various methodologies adopted to understand and model blood flow and thrombus formation. The discussion presented in the previous sections highlighted only a number of key approaches used in modelling blood flow and thrombus formation. The list of methodologies presented above is by no means complete and more computational methodologies and related information can be found in the literature. The next chapter will focus on the numerical methodology adopted in the present work to model blood flow.

Chapter 3

Introduction of SPH method

3.1 Introduction

Computational modelling of any physical or biological system must have a suitable and logical strategy to produce successful numerical simulations that can replace expensive experimental and save time, efforts and materials. As highlighted in the previous chapters, modelling blood flow to explore flow conditions has increasingly become an important tool in investigating the human body system to improve the understanding and treatment of dangerous diseases, such as thrombosis. Due to the complex geometries of arteries and vessels involved in the blood circulation, it is assumed that a simple and robust technique based on SPH meshless method would be an ideal computational method for modelling blood flow and thrombosis. This chapter outlines the essential concepts, mathematical formulations, and numerical implementation of the SPH method.

3.2 SPH Method

The SPH method is a fully Lagrangian mesh-free method which is considered to be one of the computational methods that is widely used to describe the hydrodynamics of a fluid. The SPH was originally developed to study non-axisymmetric phenomena in astrophysics. In this method, a set of particles are used to discretise the physical domain, in which the physical properties of the domain are represented by these particles. The neighbouring particles of any given particle are used in numerical discretisation to approximate the physical properties of each particle. The SPH method was first developed in the late-1970s to understand the behaviour of the astrophysical system, for which the (Eulerian) mesh-based methods were found to be quite unsuitable due to the lack of defined boundaries (Gingold and Monaghan 1977; Lucy 1977). During the early developmental stage, the SPH methods was used to

simulate viscous and heat conducting flow by Monaghan (Monaghan 1983). Following, Monaghan (Monaghan 1994) then introduced the SPH method in a free surface incompressible or nearly compressible flow and developed an appropriate boundary treatment to represent rigid boundaries that avoid the fluid particles from crossing solid boundaries. These applications further demonstrated the potential of SPH method in simulating fluid flow and have since been used without any difficulties for many applications in free surface flows. Later, the consistency and accuracy of SPH discretisation techniques were improved by using symmetrisation of formulations (Monaghan 1982; Monaghan and Lattanzio 1985; Monaghan 1992). Following these early developments, numerical simulations of various engineering and physical problems were undertaken using the SPH method (Takeda et al. 1994; Koshizuka 1995; Welton 1998; Monaghan and Kos 1999). The consistency and accuracy of the SPH method were further improved by various numerical algorithms (Swegle et al. 1995; Dyka et al. 1997; Bonet and Lok 1999; Chen et al. 1999; Dilts 1999; Bonet and Kulasegaram 2000a, b; Monaghan 2000; Dilts 2000a).

Due to the improved accuracy and stability, the application of SPH method has been extended to the simulation of industrial die casting processes (Cleary et al. 2002; Kulasegaram et al. 2002), multi-phase flows(Ritchie and Thomas 2001; Hu and Adams 2006), viscoelastic flows (Ellero et al. 2002) and interfacial fluid flows(Monaghan and Kos 1999; Colagrossi and Landrini 2003). The SPH simulation of free surface flows was also introduced in coastal engineering (Shao and Gotoh 2004; Dalrymple and Rogers 2006; Ting et al. 2006; Violeau and Issa 2007).

A brief overview of SPH literature above highlights some of the early research work carried out in the development of SPH method. To avoid any distraction, only fluid flow simulations performed using SPH method are highlighted here. In recent years,

the SPH method has been used in a significant number of challenging scientific and engineering fluid flow applications (Shahriari et al. 2012), (Kulasegaram and Karihaloo 2012), (Deeb 2013), (AL-Rubaye et al. 2017). The use of SPH in the literature is ever-growing and, therefore, only the literature relevant to the present work will be cited in this thesis.

3.2.1 The Concept Of SPH

Fluid continuum in SPH is described by a finite number of particles, N, each particle, 'a' carries various properties of the fluid, including mass m_a, velocity v_a, position x_a, density ρ_a, pressure P_a, temperature T_a and internal energy E_a depending on the fluid and the type of flow. Every physical quantity will be updated in every time step, although the mass will be kept constant. These properties are integrated by functions called 'kernel functions', which use the particles to express a physical property by replacing the integration of the field variable with the summation for the same property of the particles in a local domain, which is called a support domain, as shown in Figure 3.1. This means that any physical property at any particle (particle 'a' in the case of Figure 3.1) can be obtained by summing the same property of particles that are inside the support domain Ω, as follows:

- **Adaptive:** The particle summation is executed at every time step and the contributions of the particles are based on their current locations which govern the weighting factor of the kernel function.
- **Lagrangian:** The particle approximation is executed on all terms related to the field variables to make a set of ordinary differential equations (ODEs) in a discretised form with respect to time.

3.2.2 SPH Support Domain

The support domain for a particle '*a*' is considered as the domain where all the information (properties or field variables) of all particles inside this domain are used to calculate the information at the point '*a*' (see Figure 3.1). This means that any physical property of any particle '*a*' is obtained by summing the same property of the particles that is inside the support domain Ω (which lies within a radius *kh* of the particle *'a'*). While computing the property of particle '*a*' the contribution of neighbouring particles are multiplied by a suitable weighting (kernel or smoothing) function before the summation. The parameter *k* represents a scaling constant related to the smoothing function. Generally, the smoothing length, *h*, is small for a high-density region and large for a low-density region. Usually the average number of the neighbouring particles with in a support domain varies between 30 to 80 depending on the size of the problem domain (Kalssen 2002).

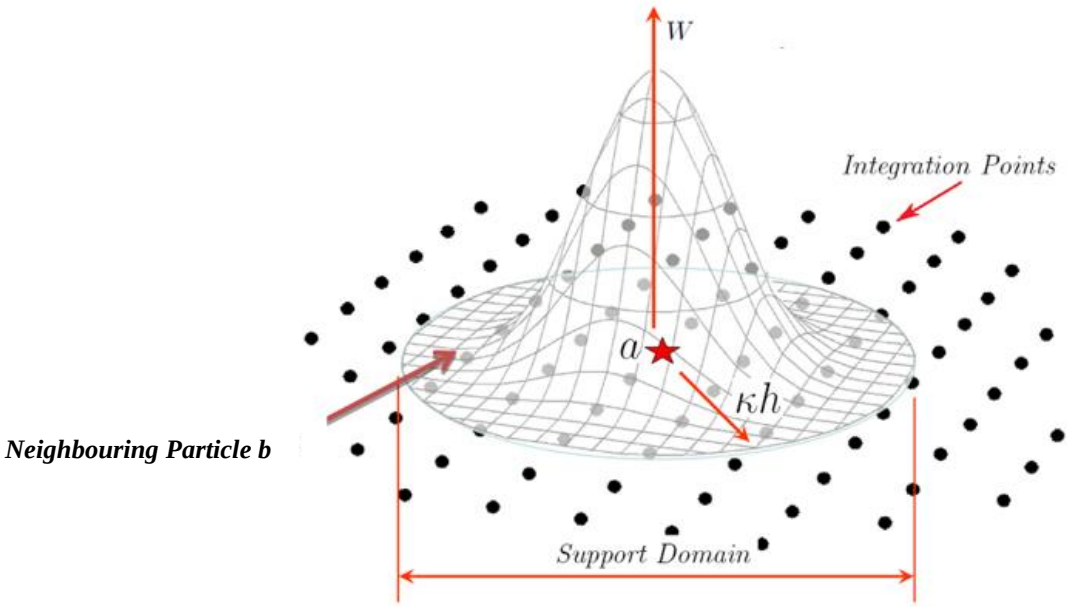

Figure 3.1 The support domain and smoothing function in two dimension for a particle a (after (Williams et al. 2011))

The smoothing radius *kh* is considered to be a key parameter in SPH interpolation. Given that the distance between particles which interact with each other is known or, in other words, the distance with a non-zero value of the smoothing kernel is known, the value of the constant, *k*, is then calculated by the choice of the smoothing kernel. In general, the value of *k* is chosen as 2. This means that particles which are separated by a distance greater than two times of smoothing length *h* will have no or very little influence on the parameters at the current particle.

Figure 3.1 presents the support domain of any particle '*a*' and all of the neighbouring particles that share the same support domain. Logically, the particles which are closer to centre (or particle '*a*') have a greater contribution to the property of particle '*a*' compared to the particles which are located far from particle '*a*'. Therefore, the influence area of each particle will be defined using the kernel function.

There are two main steps to obtain the SPH formulation and discretisation (which will be described in more detail in the subsections that follow):

- Kernel approximation can be included in the integral representation of a function and its derivatives.
- Discrete or particle interpolation.

3.2.3 Kernel Approximation

The SPH uses the following identity to represent any arbitrary function $\phi(\mathbf{x})$ in an integral form,

$$\phi(\mathbf{x}) = \int_{\Omega} \phi(\mathbf{x}')\, \delta(\mathbf{x} - \mathbf{x}') d\mathbf{x}' \tag{3.1}$$

Where the integral is evaluated over the volume Ω and $\delta(\mathbf{x} - \mathbf{x}')$ is the Driac delta defined by,

$$\delta(\mathbf{x} - \mathbf{x}') = \begin{cases} 1 & \mathbf{x} = \mathbf{x}' \\ 0 & \mathbf{x} \neq \mathbf{x}' \end{cases} \tag{3.2}$$

The Dirac delta can be replaced by an interpolation function W, so that the integral representation of $\phi(\mathbf{x})$ can be approximated as,

$$\phi(\mathbf{x}) \approx \int_{\Omega} \phi(\mathbf{x}') W(\mathbf{x} - \mathbf{x}', h) d\mathbf{x}' \tag{3.3}$$

where, W is the so-called kernel (interpolation or smoothing) function which should be differentiable, satisfy the unity condition and converge to Delta function.

Kernel W has the following properties:

1. Normalisation or unity condition states that;

$$\int_{\Omega} W(\mathbf{x}-\mathbf{x}',h)d\mathbf{x}' = 1 \tag{3.4}$$

2. Dirac delta property is observed when the smoothing length approaches zero

$$\lim_{h\to 0} W(\mathbf{x}-\mathbf{x}',h) = \delta(\mathbf{x}-\mathbf{x}') \tag{3.5}$$

3. Compact condition

$$W(\mathbf{x}-\mathbf{x}',h) = 0 \quad if \ \left|\mathbf{x}-\mathbf{x}'\right| > kh \tag{3.6}$$

where k is a scaling factor, as defined earlier. This parameter defines the domain where the smoothing function is effectively non-zero. This effective area is called the support domain and is given by

$$\left|\mathbf{x}-\mathbf{x}'\right| \leq kh \tag{3.7}$$

Here, the length parameter h has a similar interpretation to that of element size in the FEM.

3.2.4 SPH Kernel

The choice of the smoothing or kernel function is considered to be very important in SPH, and is used to determine the accuracy of the interpolated functions and the overall computations. A wide range of kernel functions, ranging from Gaussian to polynomial functions, have been used in SPH method. The kernels can be mainly classified into four types of kernels: bell shaped, parabolic shaped, hyperbolic shaped, and double hump shaped. Figure 3.2 illustrates some of the kernel functions and their derivatives. Approximately 20 types of kernel were investigated by Fulk and Quinn (Fulk and Quinn 1996) to assess their accuracy and it was concluded that the bell shaped kernels performed better than the other types of kernel.

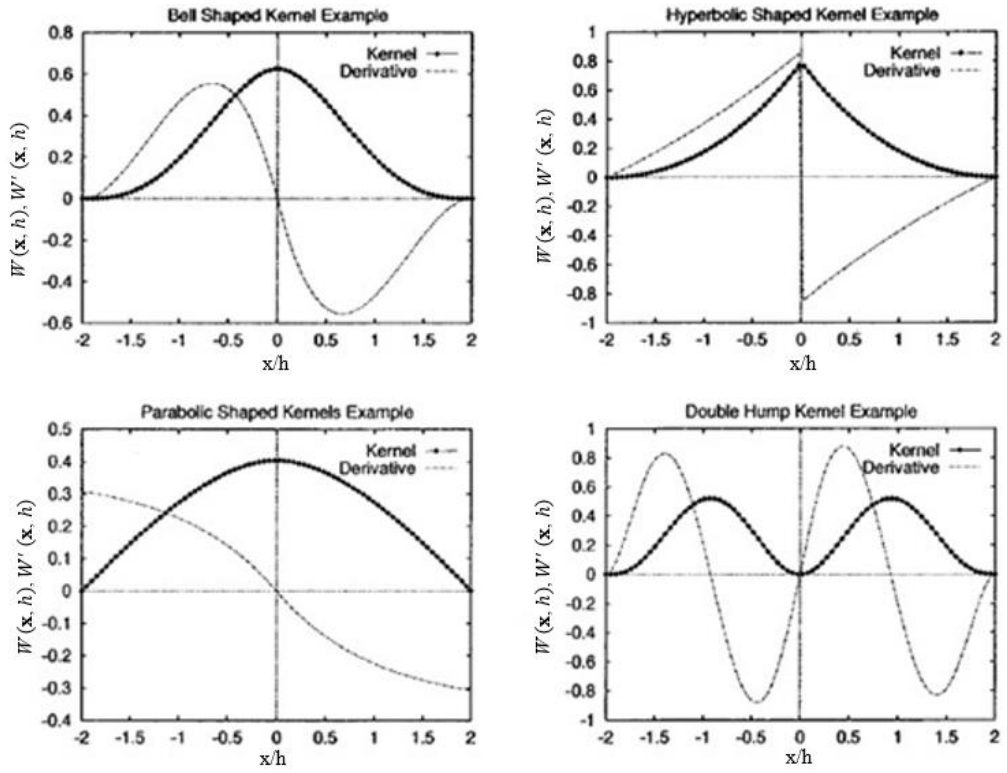

Figure 3.2 General and different shapes of kernels studied after (Fulk and Quinn 1996)

The most commonly used kernel functions are defined below:

Gaussian kernel: This is a very stable and accurate kernel. As this function asymptotically approaches zero, it is not considered to have a compact support domain. Due to this, Gaussian kernel is computationally more expensive. Equation (3.8) represents the Gaussian kernel function:

$$W(\mathbf{x}-\mathbf{x}',h)=\begin{cases}\frac{1}{\sqrt{2\pi}h}e^{-\xi^2} & \\ \frac{1}{2\pi h^2}e^{-\xi^2} & ;\ \xi=\frac{\|\mathbf{x}-\mathbf{x}'\|}{h}\\ \frac{1}{(\sqrt{2\pi}h)^n}e^{-\xi^2} & \end{cases}\qquad \begin{matrix}1d\\2d\\nd\end{matrix} \tag{3.8}$$

where, *d* is the dimension, and *h* is the smoothing length of the Gaussian kernel. As shown in Figure 3.3.

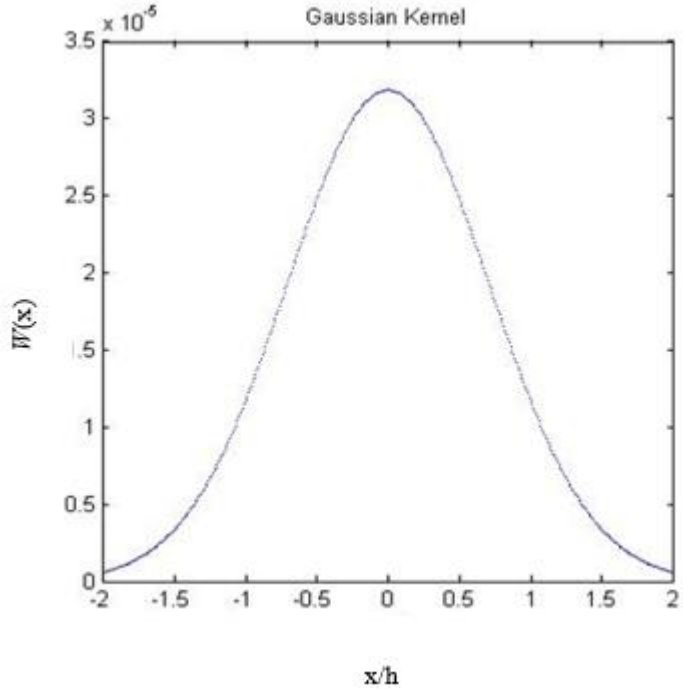

Figure 3.3 The Gaussian kernel

Cubic spline kernel: This is much narrower and has compact support. The outer edges are well defined at a distance *h* from the particle at the centre; therefore, outside these edges kernel function is defined as zero. Using the spline kernel function, Equation (3.9) represents the kernel function:

$$W(\mathbf{x}-\mathbf{x}',h)=\frac{c}{h^d}\begin{cases}1-\frac{3}{2}\xi^2+\frac{3}{4}\xi^3 & \xi\le 1\\ \frac{1}{4}(2-\xi)^2 & 1<\xi\le 2\\ 0 & \xi>2\end{cases};\xi=\frac{\|\mathbf{x}-\mathbf{x}'\|}{h} \qquad (3.9)$$

where *d* is the number of dimensions of the problem, *c* is a scaling factor for normalising the kernel function and *h* is the length parameter (smoothing length), which has a similar interpretation to that of element size in FEM. Figures 3.4 and 3.5 shown the cubic kernel and its derivative.

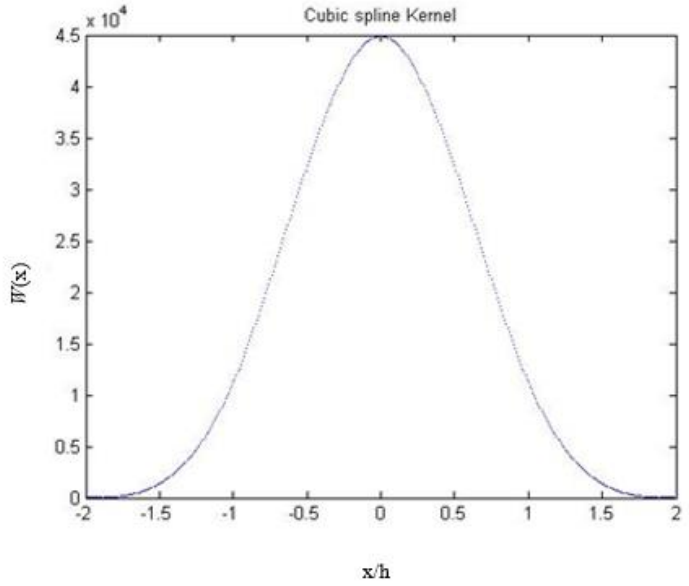

Figure 3.4 The Cubic Spline Kernel

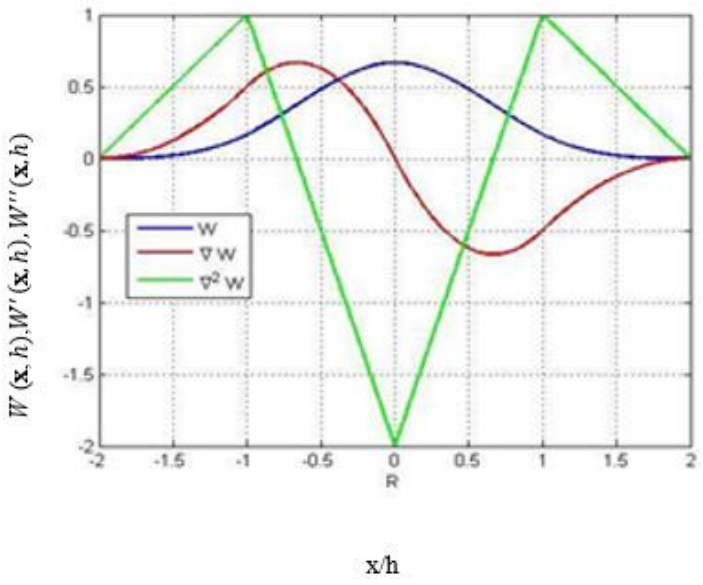

Figure 3.5 Cubic kernel derivatives

The quartic spline: This is a higher order kernel function. The quartic spline was introduced by Morris et al. (Morris et al. 1997) and is defined here in Equation (3.10). The quartic spline is more stable and closely approximates the Gaussian kernel. Unlike Gaussian, quartic spline has a compact support.

$$W(\mathbf{x}-\mathbf{x}',h)=c\begin{cases}(\xi-2.5)^4-5(\xi+1.5)^4+10(\xi+0.5)^4 & 0\le\xi<0.5\\(2.5-\xi)^4-5(1.5-\xi)^4 & 0.5\le\xi<1.5\\(2.5-\xi)^4 & 1.5\le\ \xi<2.5\\0 & \xi\ge 2.5\end{cases} \quad (3.10)$$

Where, *c* is a scaling factor.

The quintic spline: The most commonly used kernel function in SPH is a quantic spline function. This is very similar to cubic spline function, however has higher order of accuracy.

$$W(\mathbf{x}-\mathbf{x}',h)=\frac{c}{h^d}\begin{cases}(2-\xi)^5-16(1-\xi)^5 & \xi\le 1\\(2-\xi)^5 & 1<\xi\le 2\\0 & \xi>2\end{cases} \quad (3.11)$$

where, *d* is the number of dimensions of the problem, *c* is a scaling factor for normalising the kernel function and *h* is a length parameter.

3.2.5 Particle Interpolation

The particle approximation in SPH involves discretising the entire domain of the given problem into a number of particles *N*, and then approximately calculating all the field variables on these particles. First, the infinitesimal volume $d\mathbf{x}'$ at the location of particle 'b' can be approximately replaced by the finite volume of the particle V_b where, $V_b=\frac{m_b}{\rho_b}$. This embodiment of the density ρ_b and mass m_b makes SPH the ideal numerical solution to simulate the dynamic fluid flow applications. Moreover, the continuous integral in Equation (3.3) can be converted to a discretised form of summation over all the particles *N* in the support domain Ω.

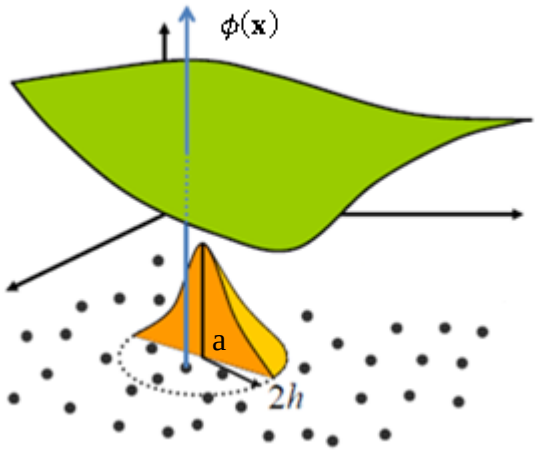

Figure 3.6 particle approximation of function $\phi(\mathbf{x})$ (after (Kulasegaram et al. 2002)

Therefore, the discretised numerical equivalent to Equation (3.3) is obtained by approximating the integral interpolation into a summation approximation given as:

$$\phi(\mathbf{x}) = \sum_{b=1}^{N} V_b \phi_b W(\mathbf{x} - \mathbf{x}_b, h) \tag{3.12}$$

Where b is taken over all the particles, and V_b is the volume attributed implicitly to particle b, $\mathbf{x}_b$ is the position, and ϕ_b is the value of any quantity ϕ at $\mathbf{x}_b$. The following relation between volume, mass, and mass-density is assumed,

$$V_b = \frac{m_b}{\rho_b} \tag{3.13}$$

where m_b is the mass and ρ_b the mass-density of particle 'b'. Replacing the volume of particle b in Equation (3.12) by Equation (3.13) yields the basis formulation of the SPH method as;

$$\phi(\mathbf{x}) = \sum_{b=1}^{N} \phi_b \frac{m_b}{\rho_b} W(\mathbf{x} - \mathbf{x}_b, h) \tag{3.14}$$

The gradient of any quantity ϕ can be approximated using SPH discretisation in the following form,

$$\nabla\phi(\mathbf{x}) = \sum_{b=1}^{N} V_b\, \phi(\mathbf{x}_b)\nabla W_b \tag{3.15}$$

where, the quantity ∇W_b denotes the gradient of the kernel. The application of Equation (3.12) to calculate the approximate value for the density of a continuum leads to the classical SPH equation:

$$\rho(\mathbf{x}) = \sum_{b=1}^{N} m_b W_b(\mathbf{x}) \tag{3.16}$$

3.2.6 Corrected SPH Integration

The basic SPH approximations as given by Equation (3.14) and (3.15) do not accurately reproduce or approximate the function $\phi(\mathbf{x})$ and its derivative $\nabla\phi(\mathbf{x})$. Therefore corrected SPH equations were developed to address these issues (Bonet and Lok 1999; Bonet and Kulasegaram 2000a).The main aim of the correction techniques is to satisfy the conservation of angular momentum which, unlike the linear momentum, is not automatically satisfied. In order to correct the SPH algorithms, some work was done on the gradient of the kernel directly (Bonet and Lok 1999; Bonet and Kulasegaram 2000a), whereas others have modified the kernel function itself (Liu and Liu 2003). Another possible way is to mix the kernel and gradient corrections (Bonet and Lok 1999; Bonet and Kulasegaram 2000a).

Using the corrected gradient of the corrected kernel, the SPH equations (3.14) and (3.15) can be re-written as:

$$\phi(\mathbf{x}) = \sum_{b=1}^{N} V_b\, \phi(\mathbf{x}_b)\widetilde{W}_b(\mathbf{x}) \tag{3.17}$$

$$\nabla\phi(\mathbf{x}) = \sum_{b=1}^{N} V_b\, \phi(\mathbf{x}_b)\widetilde{\nabla}\, \widetilde{W}_b(\mathbf{x}) \tag{3.18}$$

where, $\widetilde{W}_b(\mathbf{x})$ refers to the kernel function that is corrected to fully satisfy the consistency conditions (see Appendix A), and b is the neighbouring particle of position '$\mathbf{x}$' within the support domain. In addition, $\widetilde{\nabla}$ in Equation (3.18) indicates that the gradient is corrected to reproduce the linear consistency. The gradient correction of the kernel used in the present work is adopted from the mixed kernel and gradient correction to minimise the computational efforts associated with evaluating corrected gradients of relevant field variables. More details on corrected SPH integration can be found in the Appendix A.

3.2.7 The Nearest Neighbour Search

One of the most important factors in the SPH method is to identify the particles which interact with the others. At each time step, for every particle '*a*', a list of the entire neighbouring particles should be defined. This procedure is considered to be computationally demanding when searching for the neighbouring particles at every time step during the numerical simulation (Bayraktar et al. 2009). Therefore, it is essential to adopt efficient searching algorithms to minimise the computational efforts at this step. Many attempts were made in the past to reduce the time spent in the search of neighbouring particles. For instance, Wróblewski et al. (Wróblewski et al. 2007) compared two methods of neighbourhood search for the SPH algorithm, the Constant Cut-off Radius method and the Constant Number of Neighbours; the simulation results obtained by both methods were practically indistinguishable, while the computational costs favoured Constant Cut-off Radius. Many other methods have

been also reported such as Bucket Sort Algorithm method (Monaghan and Lattanzio 1985), All Pair search and Linked-List methods (Liu and Liu 2003). The method adopted here is the Alternating Digital Tree (ADT) which was used by Bonet and Peraire (Bonet and Peraire 1991) for geometric searching algorithms and shown to be efficient for three-dimensional problems.

3.2.8 Treatment of Boundary Conditions

The SPH method has suffered from particle deficiency near or on the boundary which affects the accuracy of the kernel estimation of field variables. Due this, imposing boundary conditions in SPH method is not straight forward as that of traditional mesh-based methods. In SPH, boundary conditions should be imposed to ensure balancing the inner particle forces thus preventing those particles from penetrating the wall. A number of approaches to enforce boundary conditions have been proposed in the SPH method so far. These methods mainly aimed to solve the issues associated with particle deficiency along the boundaries. For example, the repulsive force method (Monaghan 1994), mirror (or ghost) particles method (Takeda et al. 1994);(Cummins and Rudman 1999) and dummy particles method (Dalrymple and Knio 2000; Shao and Lo 2003); (Lee et al. 2008); (Amini et al. 2011) are some of the most commonly used numerical techniques to implement boundary conditions in SPH method. Figure 3.7 illustrates the aforementioned procedures for implementing boundary conditions in SPH method.

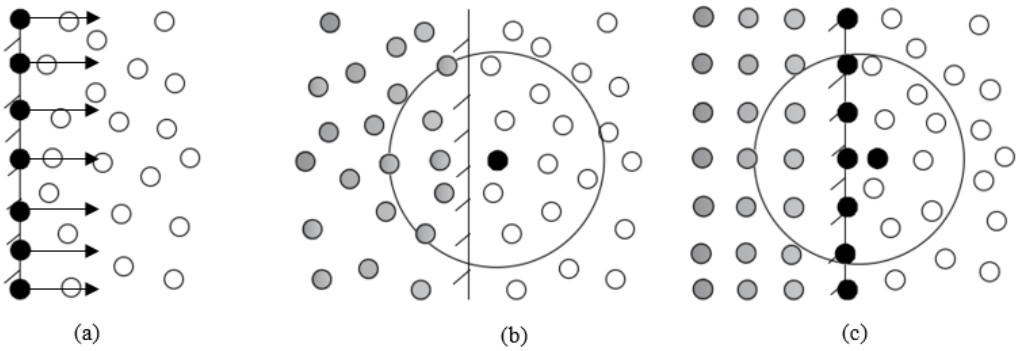

Figure 3.7 (a) Repulsive force (b) Mirror particles and (c) Dummy particles

Repulsive forces: In this method one layer of particles is added on the boundary to represent the boundary conditions (Monaghan 1994). These particles constitute the boundary that exerts high fictitious central forces on the fluid particles to prevent the particles from penetrating the wall (Zheng and Duan 2010). One of the disadvantages of this method is that it lacks accuracy when representing the interaction between the fluid and the solid. In spite of this, this method is considered to be easier to implement (Amini et al. 2011).

Mirror particles: The boundaries will be represented by set of particles with equal velocity to the fluid velocity but in an opposite direction i.e. $v_{fluid} = -v_{mirror}$, as proposed by Cummins and Rudman (Cummins and Rudman 1999). These mirror particles can be placed symmetrically or asymmetrically to fluid particle positions. One of the disadvantages of this method arises when dealing with different shapes such as curved, or cornered boundaries, because the spacing between the particles will change as a result; and this leads to a variation in density (Robinson 2009). However, (Morris et al. (Morris et al. 1997) presented a new method to deal with the curve boundary condition that used artificial velocity for the boundary particles to simulate a no-slip boundary condition.

Dummy particles: This type of boundary treatment is generally used to impose non-slip boundary condition. In this method, several layers of fixed particles which are identical to the moving ones but with zero velocity are added (Dalrymple and Knio 2000; Robert A. Dalrymple 2000). Dalrymple et al. (Dalrymple and Knio 2000; Robert A. Dalrymple 2000) used two rows of dummy particles to represent boundaries in their study. Shao and Lo (Shao and Lo 2003) in their popular approach, indicated that boundaries in dummy particles could be represented by 4 lines of static particles. The velocity of these particles is set to be zero representing non-slip boundary conditions. The pressure on the particles along the boundary edge and normal to the boundary wall surface are identical to the pressure at the fixed particles. This approach does not need any extra computational or programming steps especially when dealing with irregular boundary contours (Lee et al. 2008). The dummy particles based boundary treatment can satisfy all the fluid flow equations (momentum and continuity equations), but they retain their positions at the end of the loop if the problem involves a fixed boundary, or they change their positions in a prescribed manner if the boundary is moving, for instance at a gate (Amini et al. 2011). The accuracy of dummy particle approach can be improved by increasing the number of dummy particles increases.

Surface Particles: Along the free surface boundaries, when the support domain is truncated as shown in Figure 3.8, the number of neighbouring particles representing the support domain will be smaller. In this case pressure boundary condition is imposed where, the pressure of the surface particles will be assumed to be equal to atmospheric pressure (Lee et al. 2008).

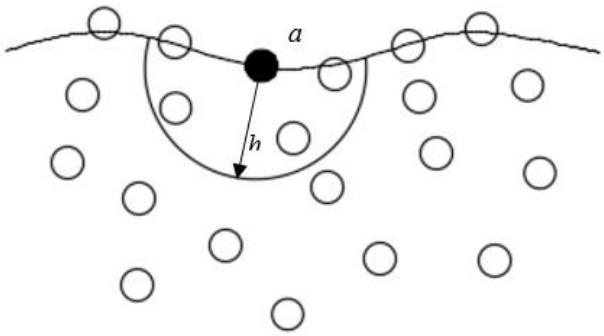

Figure 3.8 Free Surface Particles

3.2.9 Pressure Evaluation in SPH Approach

In the SPH method, the incompressibility of fluid flow is enforced generally by two different methods namely weakly or quasi compressible (WCSPH) method (Monaghan 1994; Lee et al. 2008) and fully or truly incompressible (ISPH) method (Shao and Lo 2003). Both of these approaches have their own merits and demerits. The next chapter will detail the methodology adopted in the present work to enforce the incompressibility of the fluid under investigation.

3.3 Conclusions

This chapter has defined and described the SPH numerical methodology which is to be used for modelling blood flow in the present work. The simplicity and Lagrangian nature of SPH method together with its recent developments make it an encouraging candidate to be applied in blood flow modelling in the present research. A suitable and efficient computational strategy using the SPH method will be introduced in Chapter 4 to set up the computational procedures for simulating blood flow and thrombus formation in two-dimensional and three-dimensional scenarios. It is, however, important that the developed computational techniques are able to identify

the influence of different parameters on thrombosis within arteries or vessels with various geometrical shapes and sizes.

Chapter 4

SPH for Modelling Blood Flow

4.1 Introduction

This chapter will focus mainly on the concepts relating to discretization of the governing equations using SPH method and their application on modelling blood flow and thrombus formation. Firstly, the governing equations of the mass and momentum conservation will be discussed in this Chapter. Next, the governing equations will be cast in discretised form using SPH method. Finally, the treatment of the boundary conditions and the computational procedure adopted in the present work will be outlined.

4.2 The Governing Equations

The mass and momentum conservation laws were introduced by Navier and Stokes, and they represent the fundamental physical principles of fluid flow. The governing equations of fluid flow can be described in either Eulerian form or Lagrangian form. Both of these descriptions have a number of advantages and disadvantages. However, due to numerous advantages, the Lagrangian description is a natural choice for discretisation technique used in the present work. Therefore, in this section, the mass and momentum conservation equations in the Lagrangian frame of reference will be used (see appendix B). Normally, the derivations of governing equations utilise either the concept of finite control volume or the concept of an infinitesimally small element moving with the fluid. To obtain the governing equations in Lagrangian form, from physical principles, it is convenient to use the concept of infinitesimally small element moving with the fluid. The sections 4.2.1 and 4.2.2 focus on the derivation of governing equations.

4.2.1 The continuity equation

Let us consider an infinitesimal moving fluid element with fixed mass δm and volume, so that

$$\delta m = \rho \delta V \tag{4.1}$$

where, ρ is the mass-density of the fluid.

Since the mass is conserved, we can state that the time-rate-of-change of the mass of the fluid element is zero as the element moves along with the flow, i.e.

$$\frac{D(\delta m)}{Dt} = 0. \tag{4.2}$$

The substantial derivative in Equation (4.2) can be expanded using Equation (4.1) as

$$\frac{D(\delta m)}{Dt} = \frac{D(\rho \delta V)}{Dt} = \delta V \frac{D\rho}{Dt} + \rho \frac{D(\delta V)}{Dt} = 0 \tag{4.3}$$

Rearranging Equation (4.3) gives:

$$\frac{D\rho}{Dt} + \rho \frac{1}{\delta V} \frac{D(\delta V)}{Dt} = 0 \tag{4.4}$$

The second term in Equation (4.4) is the divergence of the velocity $\nabla . \mathbf{v}$ which is the time rate of change of the volume of a moving fluid element per unit volume (see Appendix B). Hence, the Equation (4.4) can be re-written as,

$$\frac{D\rho}{Dt} + \rho \nabla . \mathbf{v} = \mathbf{0} \tag{4.5}$$

Equation (4.5) expresses the continuity equation or the mass conservation equation in the Lagrangian form.

4.2.2 The momentum equation

The momentum equations are the fundamental governing equations that describe flow of fluids by applying Newton's second law of motion which states that the total force on a fluid element is equal to its mass *m* times the acceleration of the considered fluid element. From this equation of motion, the necessary governing equation for conservation of momentum can be obtained in the Lagrangian form (see Appendix B).

Thus, the momentum conservation equations can be given as

$$\frac{D\mathbf{v}}{Dt} = -\frac{1}{\rho}\nabla P + \frac{1}{\rho}\nabla.\boldsymbol{\tau} + \mathbf{F}\,. \tag{4.6}$$

where ρ, t, $\mathbf{v}$, P, $\boldsymbol{\tau}$ and $\mathbf{F}$ represent the fluid particle density, time, velocity, pressure, shear stress, and external body force (e.g. gravity) , respectively.

For the complete description of physical principles of flow, the governing equations for conservation of energy in the Lagrangian form can also be added to the system of governing equations. However, as in the present work only isothermal flows are considered, governing equations concerning conservation of energy are ignored.

In the present work, the blood flow is regarded as a viscous Newtonian fluid. The fundamental flow equations to be used for modelling the blood flow is isothermal, Lagrangian mass and momentum conservation equations introduced above. It is believed that the assumptions proposed above are reasonable for the flow problems addressed here.

These Equations represent both Newtonian and non-Newtonian fluid flows. Since blood contains a high percentage of water, as indicated above, the blood flow is assumed as a Newtonian fluid in the present work.

For Newtonian fluids, the shear stress is generally written as;

$$\boldsymbol{\tau} = 2\mu\boldsymbol{d} \tag{4.7}$$

where μ is viscosity $\boldsymbol{d}$ is the rate of deformation tensor given by,

$$\boldsymbol{d} = \frac{1}{2}(\nabla\boldsymbol{v} + \nabla\mathbf{v}^{\mathrm{T}})\,; \quad \nabla\mathbf{v} = \nabla\otimes\mathbf{v} \tag{4.8}$$

Where, $\nabla\mathbf{v}$ is the velocity gradient and superscript T denotes a transpose. In Cartesian co-ordinate system $\boldsymbol{d}$ can be written as,

$$\boldsymbol{d} = \begin{pmatrix} \frac{\partial v_x}{\partial x} & \frac{1}{2}\left(\frac{\partial v_x}{\partial y} + \frac{\partial v_y}{\partial x}\right) & \frac{1}{2}\left(\frac{\partial v_x}{\partial z} + \frac{\partial v_z}{\partial x}\right) \\ \frac{1}{2}\left(\frac{\partial v_y}{\partial x} + \frac{\partial v_x}{\partial y}\right) & \frac{\partial v_y}{\partial y} & \frac{1}{2}\left(\frac{\partial v_y}{\partial z} + \frac{\partial v_z}{\partial y}\right) \\ \frac{1}{2}\left(\frac{\partial v_z}{\partial x} + \frac{\partial v_x}{\partial z}\right) & \frac{1}{2}\left(\frac{\partial v_z}{\partial y} + \frac{\partial v_y}{\partial z}\right) & \frac{\partial v_z}{\partial z} \end{pmatrix} \tag{4.9}$$

The mass and momentum conservation Equations can be further simplified and presented in Cartesian co-ordinate system.

Multiplying both sides of Equation (4.5) by ρ and noting that the essential derivative (or total time derivative) of density, $\frac{D\rho}{Dt}$ can be decomposed into the normal derivative $\frac{\partial\rho}{\partial t}$ and the convective derivative $\mathbf{v}.\nabla\rho$. This can be written as:

$$\left(\frac{\partial\rho}{\partial t}\right) + \mathbf{v}.\nabla\rho + \rho\nabla.\mathbf{v} = \left(\frac{\partial\rho}{\partial t}\right) + \nabla.(\rho\mathbf{v}) \tag{4.10}$$

For a steady-state flow, ρ does not change with respect to time and, hence, the term $\frac{\partial \rho}{\partial t}$ vanishes. Therefore, in Cartesian co-ordinates, Equation (4.10) can be rewritten as

$$\frac{\partial(\rho v_x)}{\partial x} + \frac{\partial(\rho v_y)}{\partial y} + \frac{\partial(\rho v_z)}{\partial z} = 0 \tag{4.11}$$

Additionally, if the flow is incompressible, ρ is constant and does not change with respect to space; therefore, Equation (4.11) is further simplified into:

$$\frac{\partial v_x}{\partial x} + \frac{\partial v_y}{\partial y} + \frac{\partial v_z}{\partial z} = 0 \tag{4.12}$$

Now, by multiplying both sides of Equation (4.6) by ρ and noting that the essential derivative (or total time derivative) of velocity $\frac{D\mathbf{v}}{Dt}$ can be decomposed into a normal derivative $\frac{\partial \mathbf{v}}{\partial t}$ and a convective derivative ($\mathbf{v}.\nabla\mathbf{v}$), the Equation (4.6) can be re-written as:

$$\rho\left(\frac{\partial \mathbf{v}}{\partial t}\right) + \rho(\mathbf{v}.\nabla\mathbf{v}) = -\nabla P + \rho\mathbf{F} + \nabla.\boldsymbol{\tau}' \tag{4.13}$$

where, in Cartesian co-ordinates, three vector components of Equation (4.9) can be written explicitly as

$$\rho\left(\frac{\partial v_x}{\partial t} + v_x\frac{\partial v_x}{\partial x} + v_y\frac{\partial v_x}{\partial y} + v_z\frac{\partial v_x}{\partial z}\right) = -\frac{\partial P}{\partial x} + \rho \mathrm{F}_x + \mu\left(\frac{\partial^2 v_x}{\partial x^2} + \frac{\partial^2 v_x}{\partial y^2} + \frac{\partial^2 v_x}{\partial z^2}\right) \tag{4.14}$$

$$\rho\left(\frac{\partial v_y}{\partial t} + v_x\frac{\partial v_y}{\partial x} + v_y\frac{\partial v_y}{\partial y} + v_z\frac{\partial v_y}{\partial z}\right) = -\frac{\partial P}{\partial y} + \rho \mathrm{F}_y + \mu\left(\frac{\partial^2 v_y}{\partial x^2} + \frac{\partial^2 v_y}{\partial y^2} + \frac{\partial^2 v_y}{\partial z^2}\right) \tag{4.15}$$

$$\rho\left(\frac{\partial v_z}{\partial t}+v_x\frac{\partial v_z}{\partial x}+v_y\frac{\partial v_z}{\partial y}+v_z\frac{\partial v_z}{\partial z}\right) = -\frac{\partial P}{\partial z}+\rho \mathrm{F}_z+\mu\left(\frac{\partial^2 v_z}{\partial x^2}+\frac{\partial^2 v_z}{\partial y^2}+\frac{\partial^2 v_z}{\partial z^2}\right) \quad (4.16)$$

Where, as defined earlier, μ is the dynamic viscosity of the fluid which is constant in the case of a Newtonian fluid.

4.3 Discretisation of The Governing Equations in SPH

In the SPH method, a group of variables and their gradients are generally interpolated from values at a discrete set of particles by using the standard approximations as in Equations (3.17) and (3.18). The governing equations of flow (i.e. Equations 4.5 and 4.6) should now be discretised in the SPH formulation to perform the numerical simulations. The numerical discretisation of individual terms in the governing equations are detailed below.

4.3.1 Divergence of velocity

The divergence of the velocity field can be obtained by identifying $\phi(\mathbf{x})$ in Equation (3.18) (see Chapter 3) with the velocity term, where

$$(\nabla.\mathbf{v})_a = \sum_{b=1}^{N} V_b \mathbf{v}_b . \widetilde{\nabla}\widetilde{W}_b(\boldsymbol{x}_a) \quad (4.17)$$

In the above equation, 'a' and 'b' denote the particle (or node) at which the divergence of velocity is numerically computed and its neighbouring particle, respectively. V_b is the volume of material assigned to particle 'b'. The $\widetilde{\nabla}\widetilde{W}_b(\boldsymbol{x}_a)$ here denotes the corrected gradient of the corrected kernel (see Chapter 3 and Appendix

A) evaluated at particle 'a' with respect to neighbouring particle 'b'. The accuracy of the approximation depends on the selection of the differentiable kernel function, especially on its closeness to the Delta function. In the present work, the higher order quantic-spline kernel function was chosen for numerical computations.

4.3.2 Gradient of pressure

Following the procedure described above, the gradient of pressure in the momentum equations can be written in the discretised form as:

$$(\nabla P)_a = \sum_{b=1}^{N} V_b P_b \widetilde{\nabla} \widetilde{W}_b(\boldsymbol{x}_a) \tag{4.18}$$

4.3.3 Viscous term

The viscous term $\frac{1}{\rho}\nabla.\boldsymbol{\tau}$ in the momentum conservation equation can, also, be calculated in a similar style, as follows:

$$\left(\frac{1}{\rho}\nabla.\boldsymbol{\tau}\right)_a = \sum_{b=1}^{N} \frac{m_b}{\rho_b^2} \boldsymbol{\tau}_b \widetilde{\nabla} \widetilde{W}_b(x) \tag{4.19}$$

The above discretised equations will be coupled with suitable numerical procedures to model blood flow.

4.4 Pressure Evaluation in SPH Method

4.4.1 Weakly or quasi-compressibility in the SPH (WCSPH)

Enforcing incompressibility in SPH can be pursued using two different approaches - the weakly or quasi-compressible SPH will be referred to as WCSPH(Monaghan 1994; Lee et al. 2008) and the truly incompressible SPH as ISPH (Kulasegaram et al. 2011). Although both strategies achieve the incompressibility, each has their own advantages and drawbacks. In the present work, due its simplicity, the WCSPH methodology is chosen to enforce incompressibility.

The WCSPH method was developed based on using state equations for computing the pressures of compressible fluids. Monaghan (Monaghan 1994) proposed a methodology to treat a real fluid as a weakly compressible material. This approach leads to the replacement of a real fluid by an artificial quasi-compressible fluid having a small, user-defined, fluctuation in the density. As it is easy to implement, this approach was widely used in many fluid mechanics applications to enforce incompressibility. WCSPH is truly explicit and, consequently, features a simple and efficient algorithm. It can yield sufficient accuracy for a wide range of problems. The WCSPH method can also be easily applied to problem with complex boundaries and various fluids. However, WCSPH does have some drawbacks due to the small-time step associated with a numerical speed of sound which must be at least 10 times larger than the maximum velocity to reduce the density fluctuation down to 1%.

In WCSPH method, the fluid pressure can be obtained using the equation of state described by Bachelor (Batchelor 1970; Monaghan 1994) for sound waves and

modified later by Monaghan (Batchelor 1970; Monaghan 1994) to suit the simulation of bulk fluid flow as,

$$P = B\left(\left(\frac{\rho}{\rho_0}\right)^{\gamma} - 1\right) \tag{4.20}$$

where, ρ_0 is the reference density and γ is a power coefficient that depends on the material properties. Cole and Weller (Cole and Weller 2009) experimentally found that the value of parameter γ for seawater is approximately 7.15 . Meanwhile, in WCSPH the value of γ is largely assumed to be 7 for fluids. To determine the constant B which governs the relative density fluctuation $\frac{\Delta\rho}{\rho}$ with $\Delta\rho = \rho - \rho_0$, Becker and Teschner (Becker and Teschner 2007) demonstrated that the compressibility effects (the density variation in fluid flow) scale with M^2 where M denotes the Mach number of flow, this results in the following relation,

$$\frac{|\Delta\rho|}{\rho_0} \propto \frac{|v_f|^2}{c_s^2} \tag{4.21}$$

where c_s is the speed of sound in the fluid flow and v_f is the speed of fluid flow. The speed of sound can be assumed to be large such that $\frac{|v_f|^2}{c_s^2}$ is typically 0.01 allowing the density variations of the order of 1%. To enforce this condition, B is chosen as:

$$B = \frac{\rho_0 c_s^2}{\gamma} \tag{4.22}$$

A small density fluctuation leads to a large pressure fluctuation because of the power coefficient γ. For free surface water flows, different choices of γ (γ =1 - 7) generally have a very small influence on the results, as shown by (Morris et al. 1997; Molteni

and Colagrossi 2009). For example, when γ = 1, the equation of pressure will be as follows:

$$P = c_s^2(\rho - \rho_0) \tag{4.23}$$

The above equation of state has been widely applied in liquid acoustics (Wylie et al. 1993).

4.5 Time step

The WCSPH method is generally implemented via explicit time stepping scheme. Therefore, the time step Δt is selected based on the relevant stability condition. In the present work time step is estimated following Bonet and Lok (Bonet and Lok 1999) as:

$$\Delta t = C_{FL} \frac{h}{\max(c + \|\mathbf{v}\|)} \tag{4.24}$$

where $0 < C_{FL} \leq 1$ is Courant number, $c = \sqrt{\gamma B/\rho}$ is the speed of sound. To avoid extremely small-time steps or to reduce computational time, an artificial smaller bulk modulus is typically used. This is obtained by choosing a small ratio between the maximum speed of the fluid and the speed of sound and then evaluating B as:

$$B = c_{max}^2 \rho/\gamma \ , \qquad \text{where} \quad c_{max} = m \, \|\mathbf{v}\|_{max} \tag{4.25}$$

values of *m* between 10 and 1000 are used.

4.6 Treatment of Boundary Condition

This sub-section will describe the implementation of boundary conditions. Two types of boundary treatment methods namely Dummy particle boundary and periodic boundary were employed in the present computations. The implementation of these boundary conditions are detailed below.

4.6.1 Dummy boundary

This type of boundary treatment was employed to represent rigid (or wall) boundary with no-slip boundary condition. To enforce no-slip wall boundary, four layers of dummy particles are used (see Figure 4.1), where the velocity of these dummy particles is set to zero. As described in Chapter 3, the dummy particles based boundary treatment can satisfy all the fluid flow equations (momentum and continuity equations), but they retain their positions at the end of the loop in the case of a fixed boundary. The pressure on the particles along the boundary edge and normal to the boundary wall surface are identical to the pressure at the fixed particles.

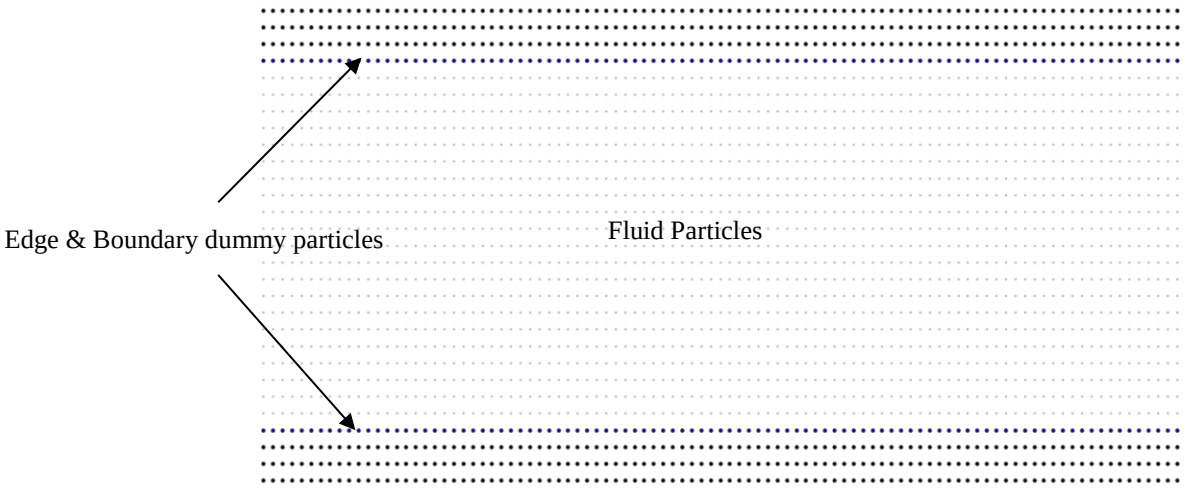

Figure 4.1 SPH discretisation of fluid with boundary dummy particles

4.6.2 Periodic boundary

The periodic boundary condition are used to keep the size of the problem domain small. In the periodic boundary treatment, a fluid particle that moves out of the computational domain through an outlet boundary is immediately inserted back through the opposite or inlet boundary. Figure 4.2 schematically illustrates the implementation of periodic boundary condition.

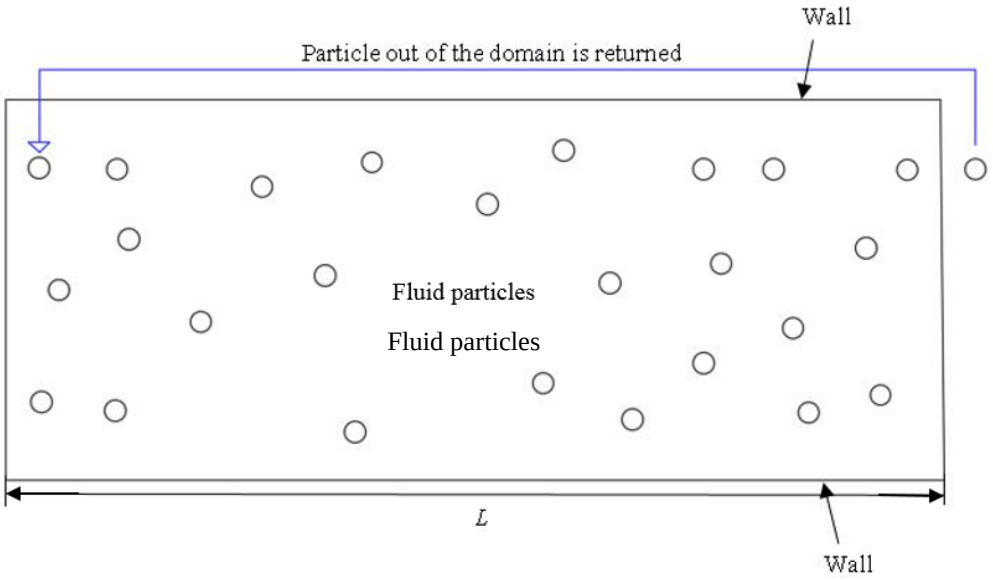

Figure 4.2 Schematic diagram of Periodic boundary conditions

4.7 The Numerical Solution Procedure

The numerical solution procedure undertaken to solve the governing equations in weakly-compressible SPH method is detailed below.

There are many possible forms of the time integration methods which can be used to update the position of SPH particles during the numerical simulation. The simple and the most commonly used time stepping method is leap-frog explicit scheme (Monaghan 1985)

To integrate the momentum equation using leap-frog explicit scheme, the intermediate velocities at point 'a' are first evaluated as,

$$\mathbf{v}_a^{n+\frac{1}{2}} = \mathbf{v}_a^{n-\frac{1}{2}} + \overline{\Delta t}\left[-\frac{1}{\rho}\nabla P + \frac{1}{\rho}\nabla.\boldsymbol{\tau} + \mathbf{F}\right]_a^n \tag{4.26}$$

then the particle positions are updated as,

$$\mathbf{x}_a^{n+1} = \mathbf{x}_a^n + \Delta t^{n+1}\,\mathbf{v}_a^{n+\frac{1}{2}} \tag{4.27}$$

where $\overline{\Delta t} = \frac{1}{2}(\Delta t^n + \Delta t^{n+1})$ and $\left[-\frac{1}{\rho}\nabla P + \frac{1}{\rho}\nabla.\boldsymbol{\tau} + \mathbf{F}\right]_a^n$ indicates that all the quantities inside the bracket are computed at point or particle 'a' at step n.

And from the continuity Equation (4.5) the density is updated as,

$$\rho_a^{n+1} = \rho_a^n - \rho_a^n\,(\nabla \cdot \mathbf{v}_a^{n+1})\,\Delta t^{n+1} \tag{4.28}$$

Finally, the pressure at all the particles at step n+1 can be estimated using the state equation defined by Equation (4.20). A flowchart describing the overall numerical computational procedure is illustrated in Figure 4.3.

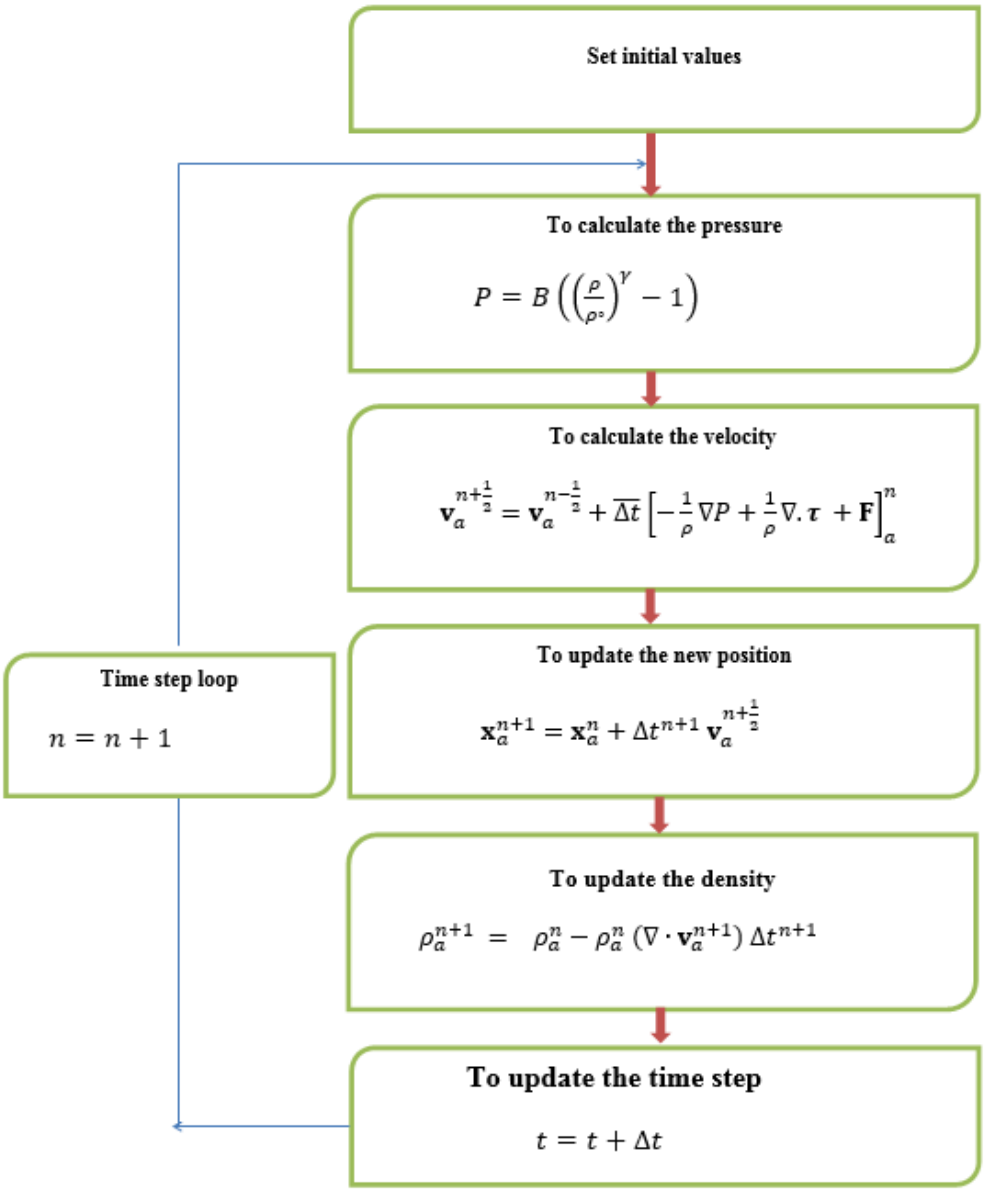

Figure 4.3 Numerical procedure for SPH flow modelling

4.8 Conclusion

This chapter has detailed the governing equations and has outlined the key numerical procedures to be used in Lagrangian SPH modelling of Newtonian flow. The next chapter will focus on evaluating the accuracy of numerical methodology developed in this chapter and, will investigate the application of proposed methodology in blood flow simulation.

Chapter 5

Benchmarking of SPH Numerical Simulations

5.1 Introduction

This chapter aims to validate the accuracy of the SPH numerical methodology that was developed in Chapter 4. It also aims to demonstrate the ability of the computational code that was developed to simulate the steady and oscillatory flows under flow conditions similar to those found in the human body. The effect of particle resolution on the accuracy and order of convergence of the SPH simulations will also be discussed. It is essential to assess and demonstrate that the flow model proposed is able to yield sufficient accuracy before it is used to simulate blood flow. For this purpose, the accuracy and convergence characteristics of the proposed methodology are first verified in the standard numerical tests that are used in computational fluid mechanics. These examples are chosen so that the various characteristics of fluid flow can be assessed under different flow conditions. In addition, these standard numerical tests can also confirm the applicability of the numerical methodology to blood flow in human body systems, such as cardiovascular systems. Finally, the numerical techniques that are developed will be used to study the blood flow in human bifurcation artery. In this test, the results of the numerical simulations are compared with the experimental observations reported in the literature. A convergence study of the numerical results is also performed to assess the computational efficiency of the proposed numerical procedure.

5.2 Test Cases

Most fluid flow phenomena in science and engineering vary with time at different locations along the flow path and they are characterised by a wide range of Reynolds numbers. For instance, cardiovascular flows can be characterised as unsteady flows

with moderate Reynolds numbers due to oscillatory nature of the driving forces. First, the accuracy of the SPH numerical model was assessed by simulating the transient behaviour of Poiseuille flow for different Reynolds numbers up to 1500. The capability of SPH to simulate unsteady flows produced by an oscillating pressure difference for various of Womersley (Wo=1,10 and 16) and amplitudes were then tested.

Lid-driven cavity flow is chosen in the next example. This case is considered to be very useful due to the similarity between flow characteristics observed in this test and blood flow inside the human heart during the filling phase. In particular, the appearance of a recirculation zone in the lid-cavity test is similar to that observed in the human heart. Moreover, the exam of this case is also considered as a benchmark for numerical simulations because reference data are available up to high Reynolds numbers. The simulation of steady flow for different Reynolds numbers has been reported in the SPH literature (Ting et al. 2006; Lee et al. 2008; Basa et al. 2009). In this study, flows with different Reynolds numbers (Re=400 and Re=1000) are considered. These values are selected to show the ability of SPH to simulate this kind of flow in a laminar regime. During this simulation, the effect of particle resolution on the results of the SPH is also demonstrated.

Flow over a cylindrical obstacle is analysed next to assess the accuracy of the developed model in such scenarios. These scenarios are commonly encountered in blood vessels. For example, the flow characteristics observed in this example will be similar to those observed in the human when the blood vessel contains internal surface variations.

Finally, a downstream-Facing Step Flow case is presented to investigate the transient blood flow phenomena with a variation of vessel geometry along the flow field. This type of geometry is close to that of arteries or vessels that are commonly found in the human body circulatory systems, such as curvature and bifurcation artery. These tests are considered to be very interesting because of the most major medical problems in the arterial system, such as atherosclerosis and thrombosis, happen in arteries that have different shapes, such as bends and bifurcations.

The following subsections will detail the various numerical test cases that were performed to investigate the accuracy and characteristics of the SPH based simulations.

5.2.1 Poiseuille Flow

In general, the Poiseuille flow consists of two infinite parallel plates and the movement of fluid between the plates is represented as the flow in channels or pipes. Figure 5.1 describes the boundary conditions and the characteristics of the Poiseuille flow. In this flow, the fluid is driven by an axial pressure difference. There is no applied pressure difference in the vertical or y direction; thus, the flow is mainly directed parallel to the plates. The fluid can be accelerated due to a directional pressure difference and this can be interpreted as the effect of an external body force in the momentum equation. A body force causing acceleration, $\boldsymbol{a}$ of a fluid element can be given as

$$\boldsymbol{a} = \frac{\boldsymbol{f_b}}{\boldsymbol{\rho}} \tag{5.1}$$

where $\boldsymbol{f_b}$ is the body force per unit volume of the fluid element and ρ is the density, which is the so-called force density.

In this case, the plates are located at $y = 0$ and $y = L$ as illustrated in Figure 5.1. The fluid will start moving from rest until it reaches a steady state. The analytical solutions for axial velocity as a function time t and position y is given by (Morris et al. 1997).

$$V_x(y,t) = \frac{\boldsymbol{f_b}}{2\nu} y(y-L) + \sum_{\mathrm{n}=0}^{\infty} \frac{4\,\boldsymbol{f_b} L^2}{\nu\,\pi^3(2\mathrm{n}+1)^3} \sin\left(\frac{\pi y}{L}(2\mathrm{n}+)\right) \exp\left(-\frac{(2\mathrm{n}+1)^2\pi^2\nu}{L^2}t\right) \quad (5.2)$$

where V_x is the flow velocity in the x direction, t is the time, and ν is the kinematic viscosity. The force applied here in x direction is given as:

$$\boldsymbol{f}_b = -\frac{1}{\rho}\frac{dp}{dx} = \frac{8\nu\,V}{L^2} \quad (5.3)$$

where, $\frac{dp}{dx}$ is the pressure gradient in x direction and V is the maximum steady state velocity.

In this test, the parametric values of ρ, L and ν are assumed as $1000\ \mathrm{kg/m^3}$, $0.005\ \mathrm{m}$ and $1\ \mathrm{x}\ 10^{-6}\ \mathrm{m^2 s^{-1}}$ respectively.

The simulations were performed for two different geometrical cases, with the distance L between the plates $0.005\ \mathrm{m}$ and $0.0025\ \mathrm{m}$, to investigate the flow with two different Reynolds numbers. A uniform spacing between particles (i.e. $\Delta \mathrm{x} = \Delta \mathrm{y} = 0.0001\mathrm{m}$ and $0.00005\mathrm{m}$) corresponding to 50 particles across the span

between the plates were used in the case of both Reynolds numbers. The results of the simulation are shown in Figure 5.2.

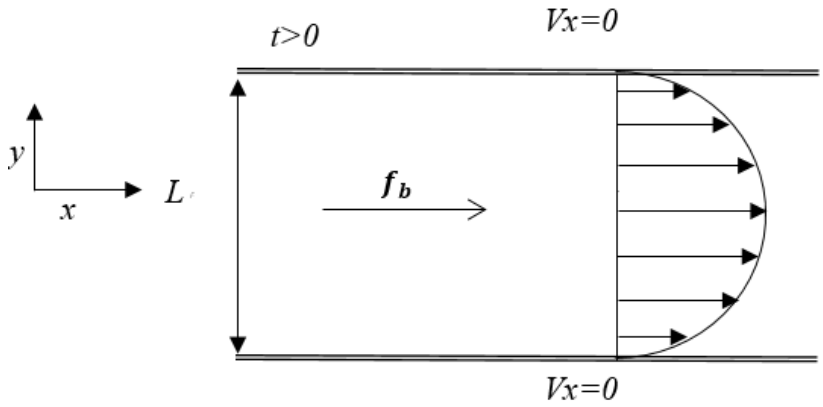

Figure 5. 1 Schematic diagram of Poiseuille flow

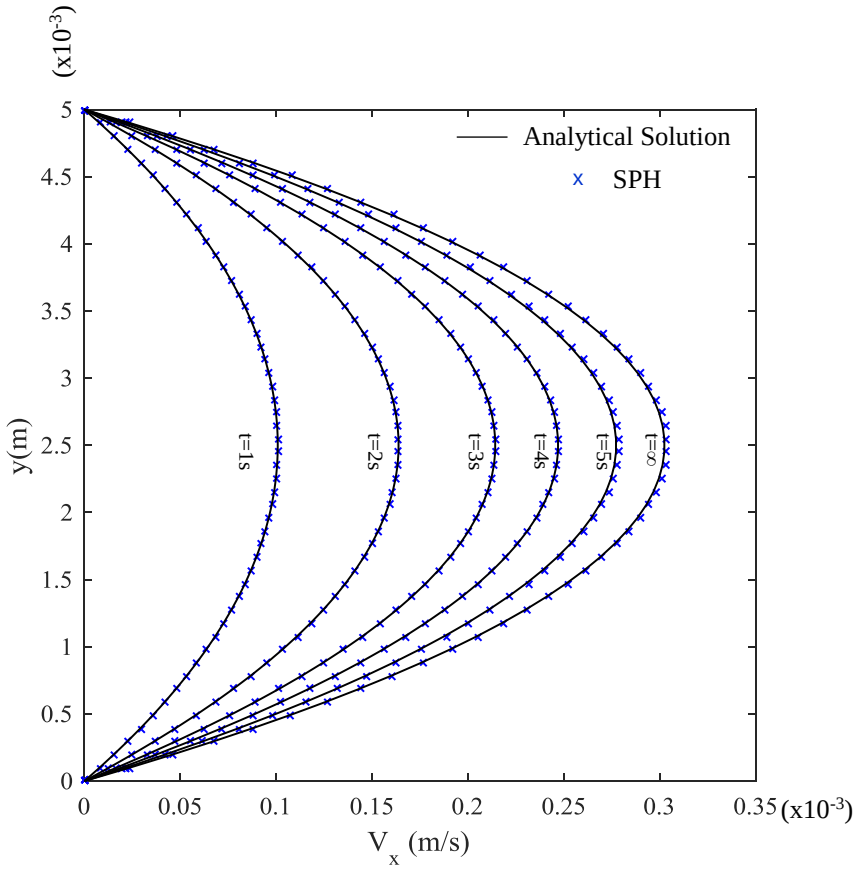

(a)

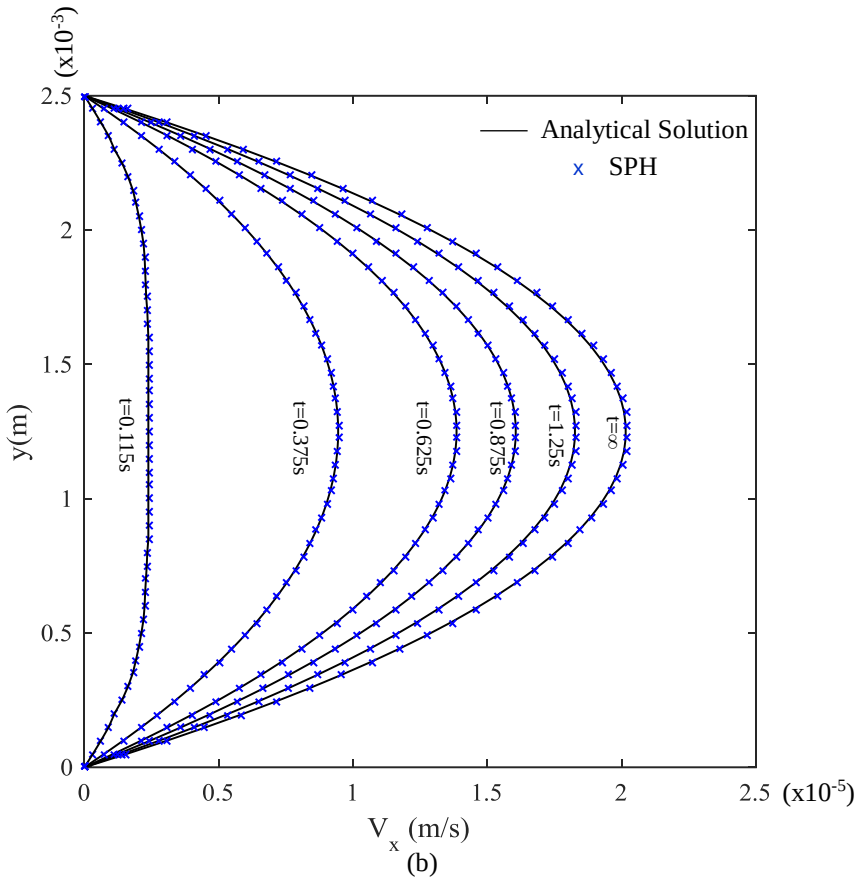

Figure 5. 2 Velocity profiles of Poiseuille flow at various stages for (a) *Re*=1500 and (b) *Re*=0.05

The difference between the numerical simulation results and the analytical solution is determined using the Relative error equation which defines as,

$$\text{Relative error} = \sqrt{\frac{\sum_{i=1}^{i=N}\left(A_{i,SPH} - A_{i,Exact}\right)^2}{\sum_{i=1}^{i=N}\left(A_{i,Exact}\right)^2}} \tag{5.4}$$

where, $A_{i,SPH}$, $A_{i,Exact}$ are the SPH and exact analytical solution for parameter *A* at particle *'i'* and *N* is the total number of particles used to calculate the relative error. The results are compared with the existing analytical solution. The numerical results are in close agreement with the analytical solution. For the case of Re=1500, the maximum relative error is 0.42% for the peak velocity during the simulation and the average relative error over all the particles in the domain at steady state is 0.40%.

5.2.2 Internal Flow Driven by Oscillating Pressure Difference

In this example, the pressure gradient induced in the axial direction of the flow does not remain constant (as in Poiseuille flow) but varies with time. This type of flow is usually found in large arteries and the industrial piping systems due to changes in the direction of pressure waves. The flow direction of the fluid between two parallel plates oscillates due to periodically varying pressure gradient, applied axially. The equation of employed pressure gradient is given by,

$$\frac{dp}{dx} = -A\cos(\omega t) \tag{5.5}$$

where ω is the oscillation frequency ($\omega = \frac{2\pi}{\mathrm{T}}$), T is the period of oscillation, A is the amplitude of the imposed pressure gradient, and t represents time. The analytical solution for axial velocity is given as (Loudon and Tordesillas 1998):

$$V_x(y,t) = \frac{\mathrm{A}}{\omega\rho\gamma}\{[\sinh\emptyset_1(y)\sin\emptyset_2(y) + \sinh\emptyset_2(y)\sin\emptyset_1(y)]\cos(\omega t) + [-\cosh\emptyset_1(y)\cos\emptyset_2(y) - \cosh\emptyset_2(y)\cos\emptyset_1(y)]\sin(\omega t)\} \tag{5.6}$$

where,

$$\emptyset_1(y) = \frac{\mathrm{W_o}}{\sqrt{2}}\left(1 + \frac{2y}{\mathrm{d}}\right), \emptyset_2(y) = \frac{\mathrm{W_o}}{\sqrt{2}}\left(1 - \frac{2y}{\mathrm{d}}\right) \tag{5.7}$$

And,

$$\gamma = \cosh\left(\sqrt{2}\mathrm{W_o}\right) + \cos\left(\sqrt{2}\mathrm{W_o}\right) \tag{5.8}$$

Here, $\mathrm{W_o}$ is the Womersley number, which is a dimensionless quantity representing the ratio of the oscillatory inertial effort (or pulsatile flow frequency) to the viscous effect and is defined as:

$$W_o = \frac{d}{2}\sqrt{\frac{\omega}{\nu}} \tag{5.9}$$

Figure 5.3(a) and (b) present the simulation results obtained for oscillating pressure gradient with two different amplitudes of 0.09 N/m^3 and 0.9 N/m^3. The density (ρ) and viscosity (ν) of the fluid were chosen as $1000\ kg/m^3$ and $1 \times 10^{-6}\ m^2s^{-1}$. The value of W_o for the flows presented in Figure 5.3 is equal to 1. Period T was chosen as 0.61s. In this simulation, the distance d between the plates was assumed to be 0.0025m and, 20 particles were used across the span between the plates. The initial particle spacing in both directions (i.e. Δx and Δy) was 0.000125m. It is evident from Figure 5.3 that the numerical results are in good agreement with the analytically estimated velocity profiles During this simulation, the relative error for velocities along the centreline between the plates has a maximum value of 0.69% and the average value of the relative error considering all the particles in the domain is 0.33%.

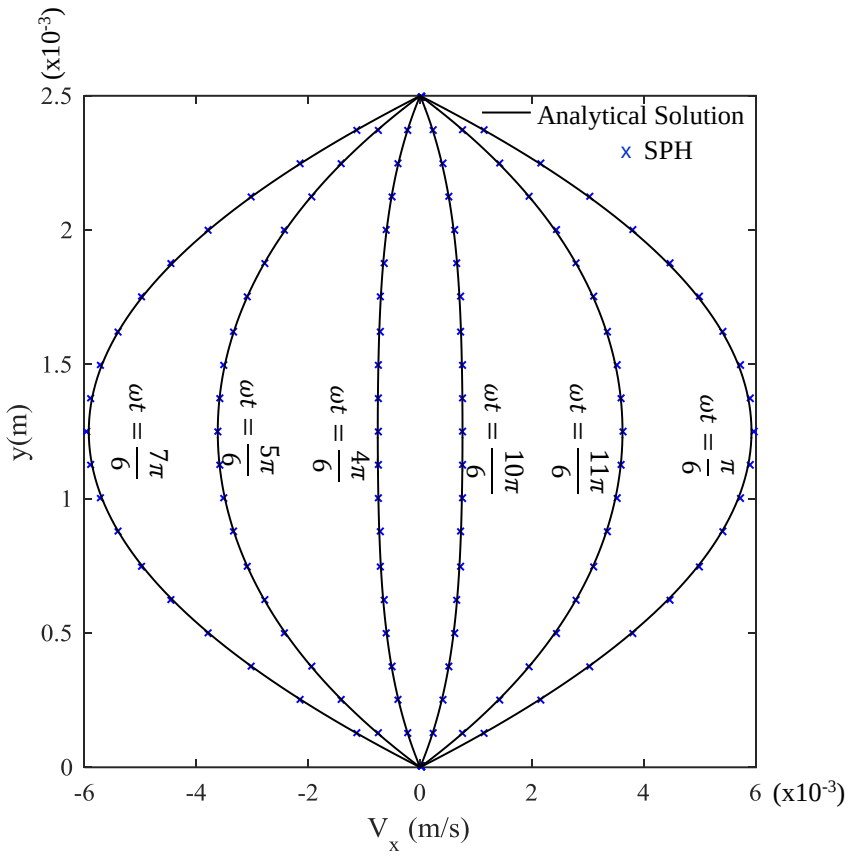

(a)

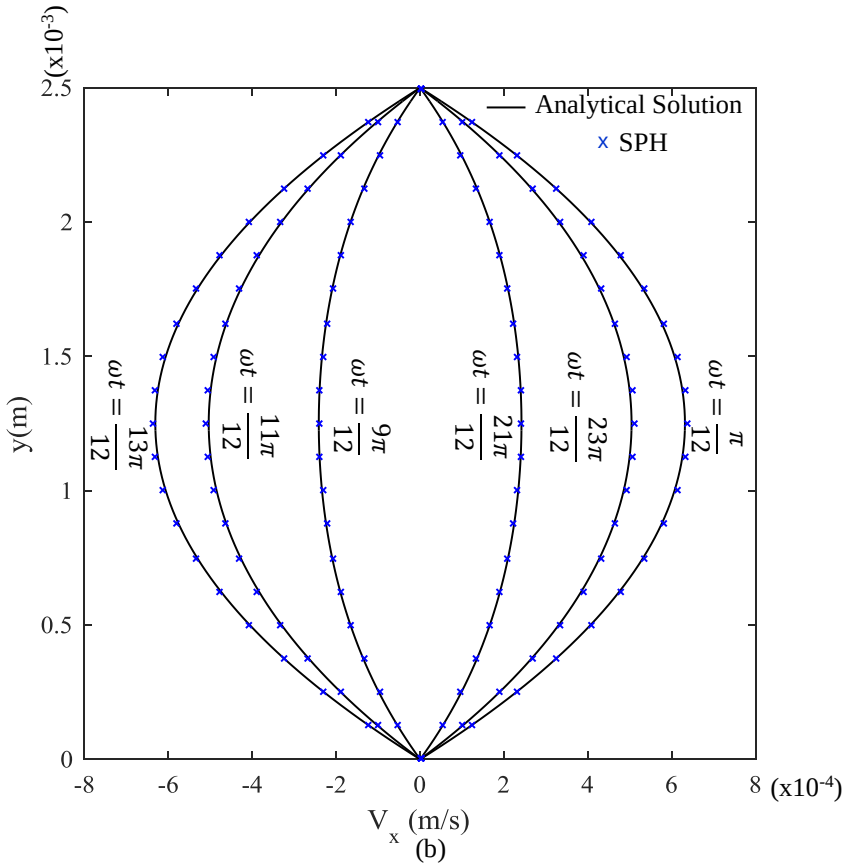

(b)

Figure 5. 3 Velocity profile of oscillating flow (Wo = 1) at various stages for (a) A = 0.09 N/m^3 and (b) A = 0.9 N/m^3

Figure 5.4 (a) and (b) illustrate the simulation results obtained with larger Womersley numbers (i.e. $W_o = 10$ and $W_o = 16$) where the distance between the parallel plates was assumed to be 0.01m. The amplitude of pressure gradient used in this simulation was $0.3 N/m^3$. Here, the fluid domain was discretised by regular grid with initial particle spacing of 0.0002 m in both directions (Δx and Δy). The numerical results are again closer to analytical estimation of the velocity profiles. During the simulation, the relative error for velocities along the centreline between the plates for $W_o = 16$ has a maximum value of 0.66% and the average value of the relative error considering all the particles in the domain is 0.34%.

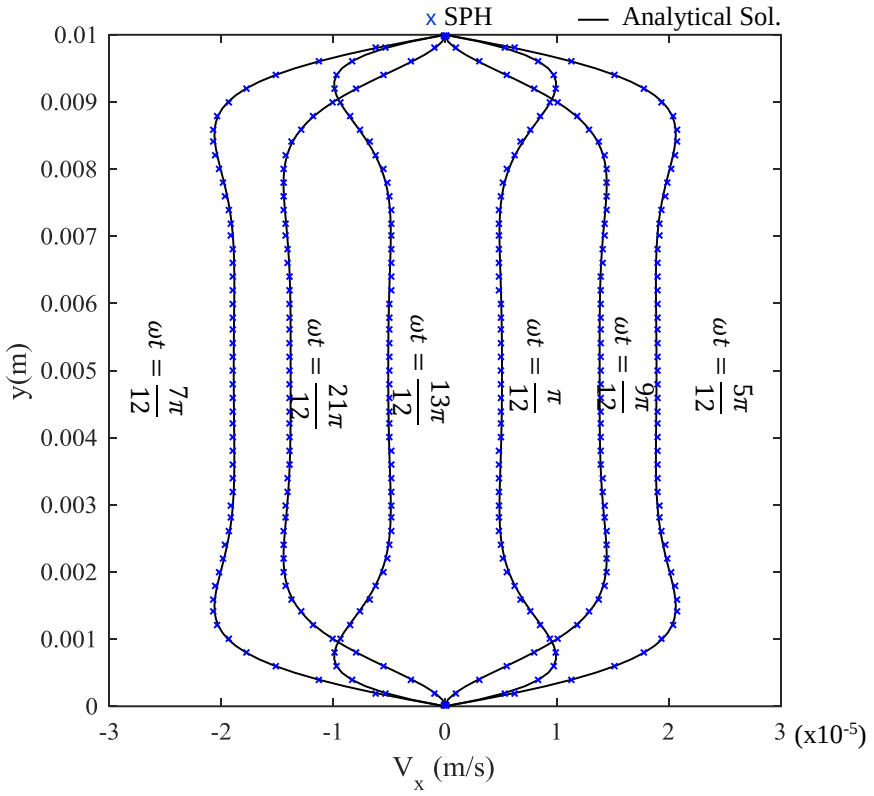

(a)

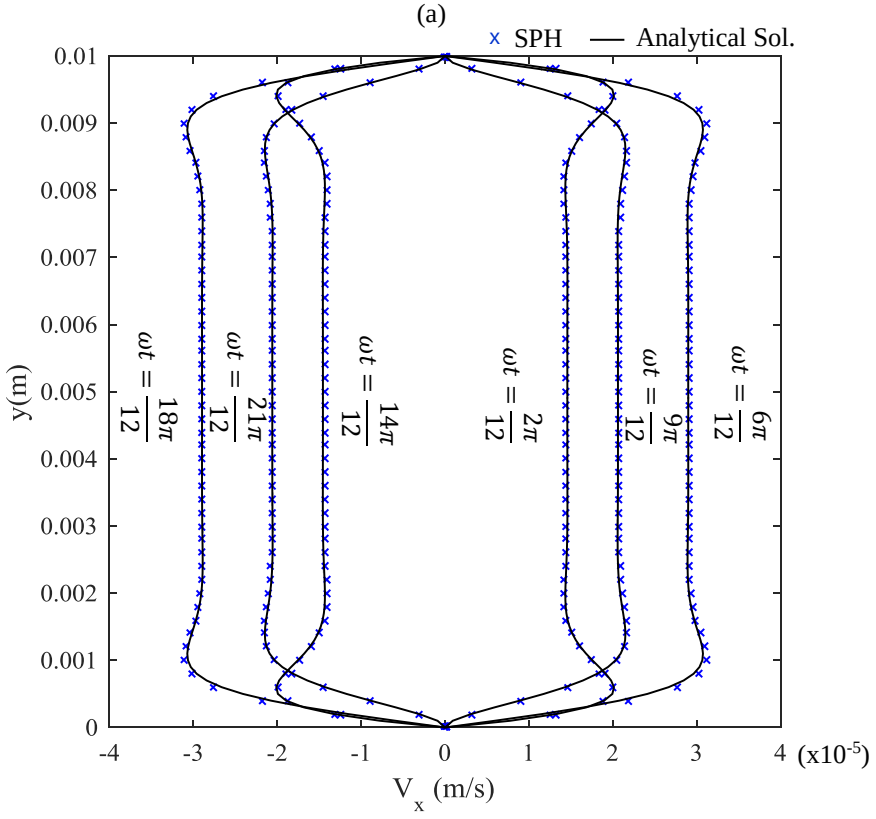

(b)

Figure 5. 4 Velocity profile of oscillating flow at various stages with (a) $W_o = 10$ and (b) $W_o = 16$

Another important parameter to be examined in the above oscillatory flows is the phase shift between the applied pressure gradient and the resulting velocity. Figures 5.5(a) and 5.5(b) show the applied pressure gradient and corresponding velocity profile obtained over a period for two different Womersley numbers (i.e. $W_o = 10$ and $W_o = 16$). As revealed by Figure 5.5, the numerical results produced by SPH method compare well with analytical solutions.

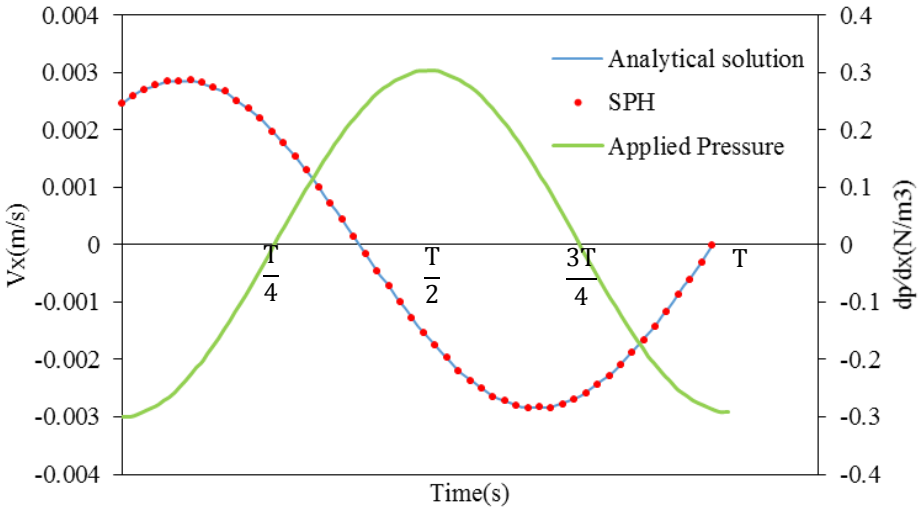

(a)

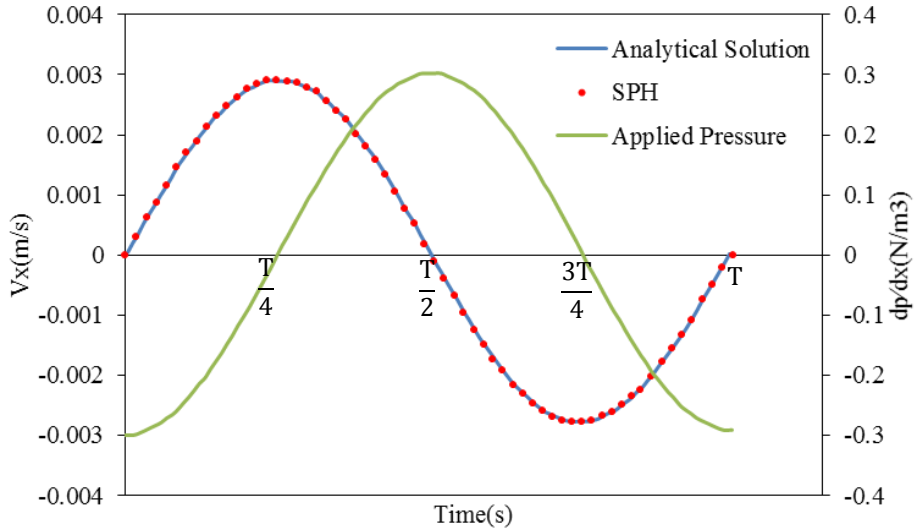

(b)

Figure 5.5 Computed centreline velocity and pressure gradient (A= 0.3 N/m^3) of oscillating flow for (a) $W_o = 10$ and (b) $W_o = 16$

Figure 5.6 illustrates the results of numerical convergence study performed in this example. In this study, three different particle mesh with 20, 39 and 77 SPH particles across the span (d = 0.01 m) between the plates were used. The results in Figure 5.6, corroborate that the numerically computed velocities converge to the analytically determined values.

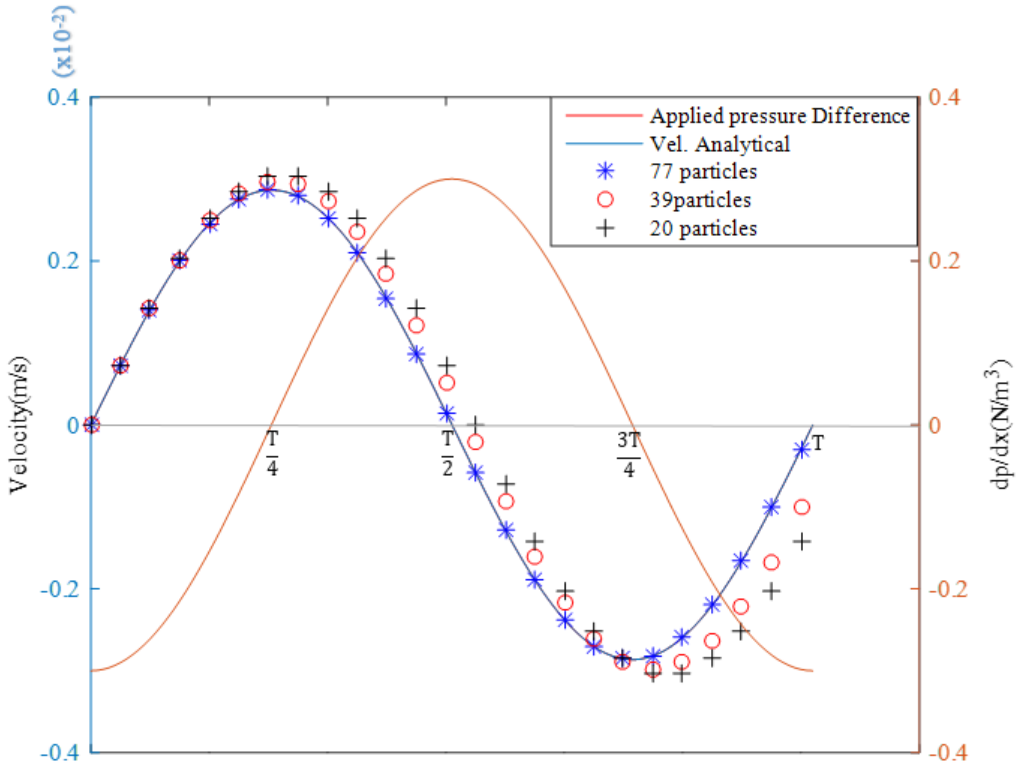

Figure 5.6 Computed centreline velocity and applied pressure gradient for Oscillating flow over a period (Wo=16 and A= 0.3 N/m^3)

5.2.3 Lid-Cavity Flow

Flow inside closed boundaries is encountered in cardiovascular systems. Therefore, this lid-cavity flow test is chosen here to assess the accuracy and efficiency of the proposed method. In this example, the flow inside a square cavity is examined using SPH method. The motion of the fluid is induced here by a moving

lid, which is on the top side of the cavity. Figure 5.7 illustrates the configuration of the lid-cavity test with relevant boundary conditions. The Reynolds number is defined here as, $Re = \frac{V_o L}{\nu}$, where V_o is the velocity of the lid, which is in the *x*-axis direction as indicated by Figure 5.7. The length (L), viscosity (ν) and density (ρ) were chosen as $1\,\mathrm{m}$, $0.0025\,\mathrm{m^2 s^{-1}}$ and $1\,\mathrm{kg/m^3}$ respectively. Initially the Reynolds number (Re) of the flow was assumed as 400. Four different meshes with total number of particles 40 x 40, 70 x 70 ,100 x 100 and 200 x 200 were used to discretise the square region of the lid-cavity. In this simulation, the speed of sound (c) was assumed to be equal to $100V_0$. Figure 5.8 shows the velocity profiles obtained by the numerical simulations, at the mid-vertical and mid- horizontal cross sections of the cavity with different particle spacing (or resolution). The results are compared with the results of Ghia et al. (Ghia et al. 1982). The effect of different particle resolution is clearly visible in the figure 5.8.

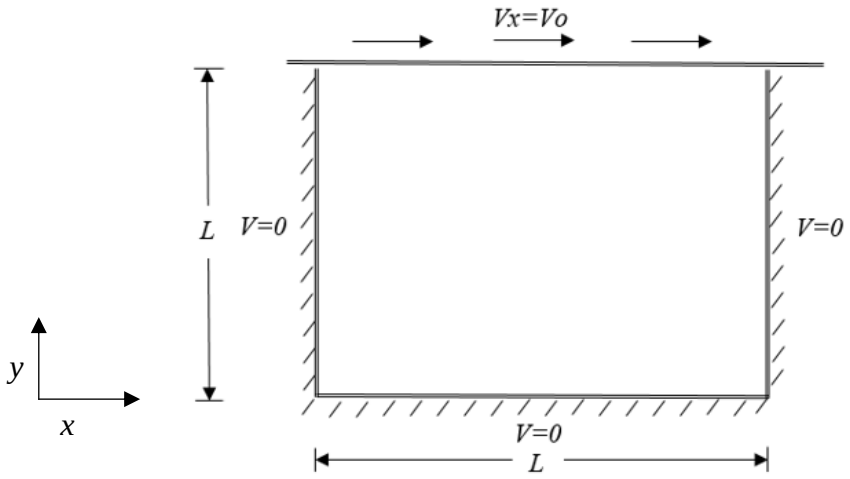

Figure 5. 7 Configuration of the Lid-Cavity Test

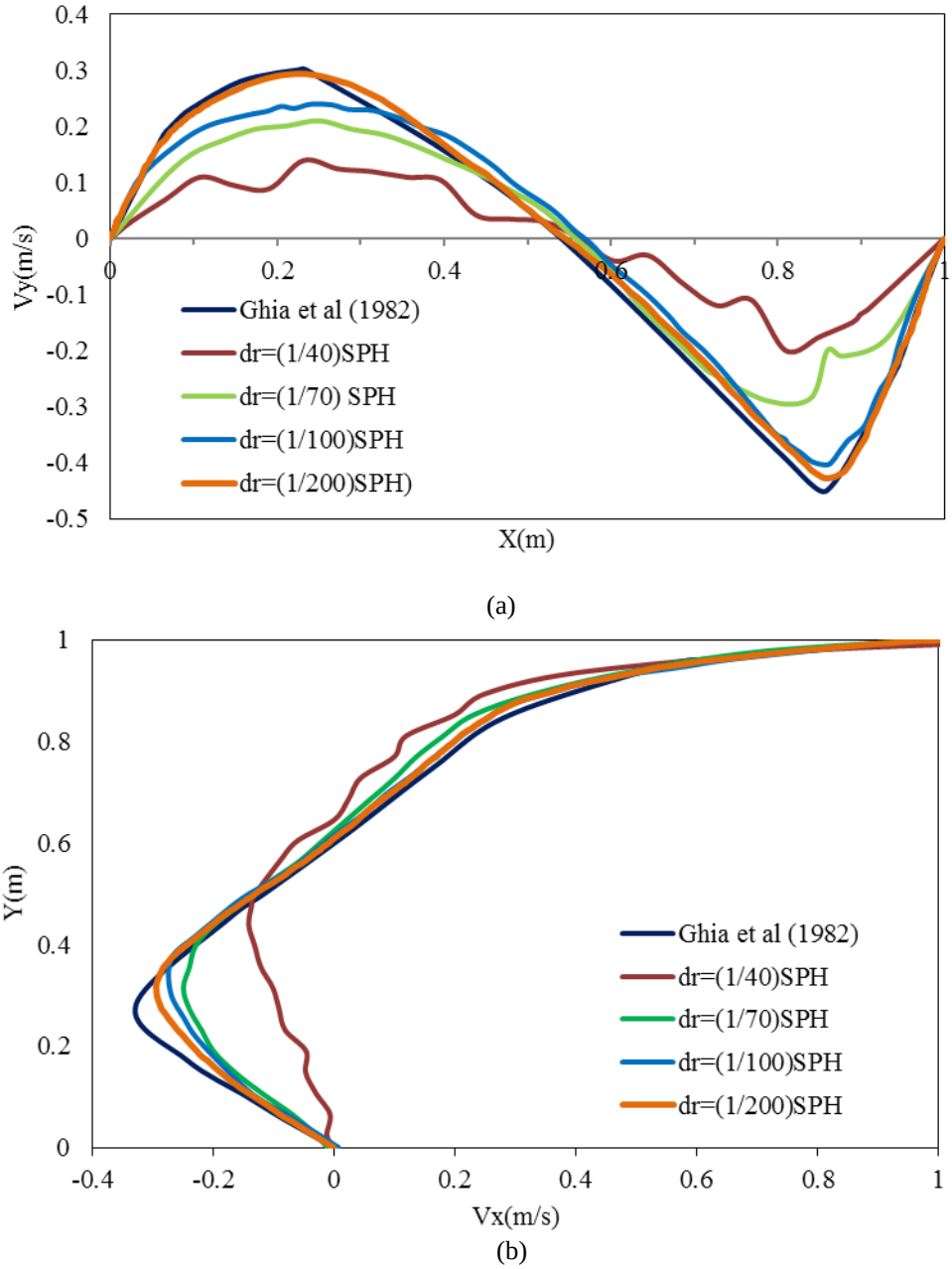

Figure 5. 8 Velocity profiles (Re = 400) at (a) mid-horizontal (b) mid-vertical cross-sections

To explore the effect of Reynolds number on the numerical results, the lid-cavity with Reynolds number 1000 was tested. For this purpose, the length (L), viscosity (ν) and density (ρ) were chosen as 1 m, 0.001 $\mathrm{m^2 s^{-1}}$ and 1 $\mathrm{kg/m^3}$ respectively. Figure 5.9 shows the velocity profiles at mid-vertical and mid- horizontal cross–sections of the cavity at different particle resolutions. The results are again compared with the

results from Ghia et al. (Ghia et al. 1982). Similar to the previous case, the effect of different particle resolutions can be clearly noticed from the figure 5.9.

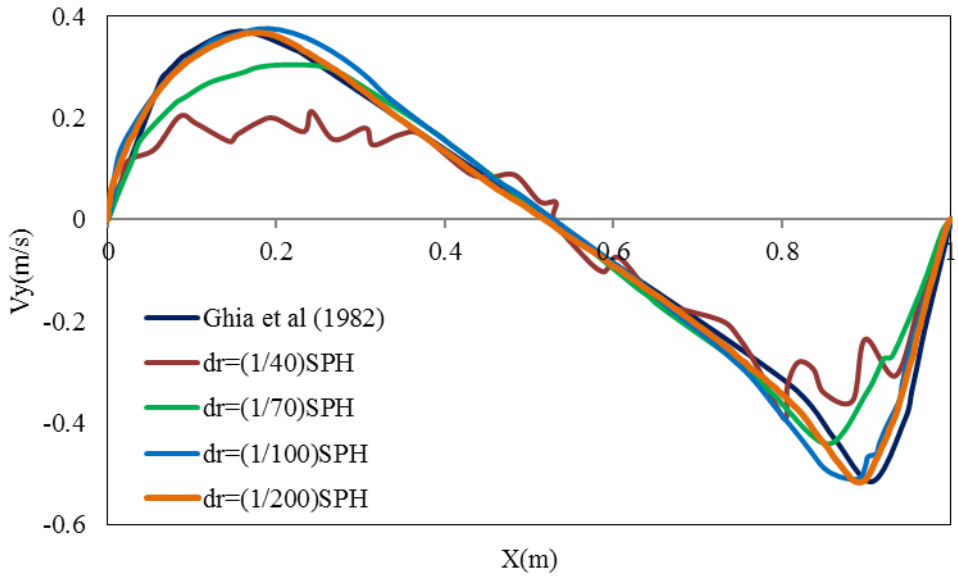

(a)

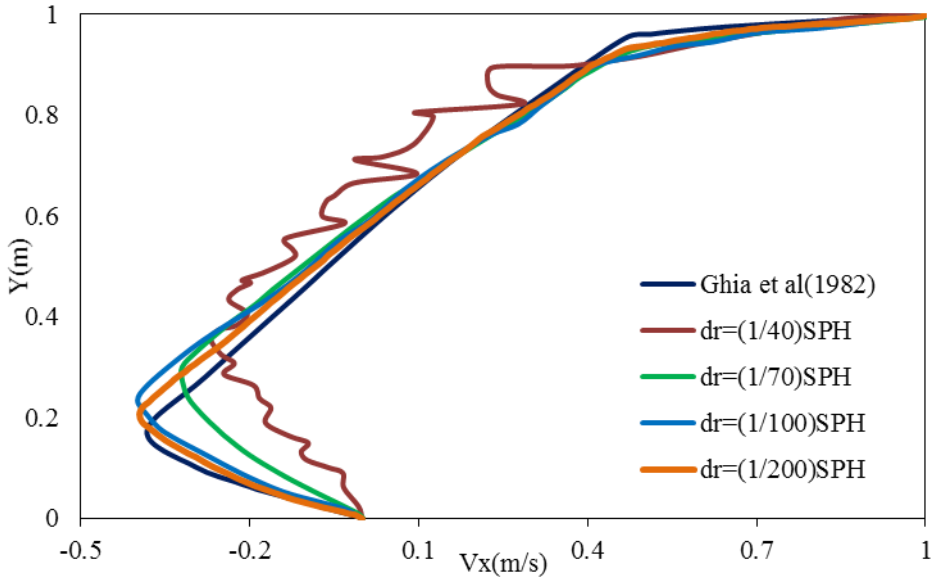

(b)

Figure 5. 9 Velocity profiles (Re=1000) at (a) mid-horizontal and (b) mid-vertical cross-sections

From the numerical results of the lid-cavity tests, it is evident that the velocity profiles obtained with SPH simulations are converging towards the results from Ghia et al. (Ghia et al. 1982). However, the results of flow with higher Reynolds number demonstrate better convergence rate. It can be noted from figures 5.8 and 5.9 that the

numerical results of the simulation converge towards the reference data with increasing particle resolution.

5.2.4 Flow over a Cylindrical Obstacle

This example is chosen to investigate the accuracy of the numerical simulations during the flow over obstacles. Especially, the effect of interaction between the flow and obstacle, on the accuracy of the numerical simulation to be explored in this test. In this numerical simulation, two-dimensional flow over a cylindrical obstacle was investigated. The geometry, as illustrated in Figure 5.10 (Morris et al. 1997) was chosen, where the radius of the cylinder is 0.02m, and the length (L) of the domain is 0.1m. Flow with two different Reynolds numbers 0.03 and 1 were simulated in this study. The particle spacing in both directions (Δx and Δy) was 0.002 m. The Table 5-1 lists the various parameters used in each test case.

Table 5. 1 Reynolds number (Re), velocity scale (V_o), viscosity (ν) and Speed of sound (c)

Case	Re	V_o m/s	ν m^2s^{-1}	c m/s
1	1	$5\ \text{X}\ 10^{-5}$	$1\ \text{X}\ 10^{-6}$	$5.77\ \text{X}\ 10^{-4}$
2	0.03	$1.5\ \text{X}\ 10^{-4}$	$1\ \text{X}\ 10^{-4}$	$1\ \text{X}\ 10^{-2}$

In Figure 5.10, $\boldsymbol{f_b}$ is the body force which drives the fluid flow over the cylindrical obstacle. The body force values used in case 1 and case 2 are $1.5\ \text{x}\ 10^{-7}\ \text{m/s}^2$ and $5\ \text{x}\ 10^{-5}\ \text{m/s}^2$ respectively. Periodic boundary conditions (see Chapter 4) were applied at the two opposite sides (inlet and outlet regions) of the domain. Aim of this

numerical test is to obtain horizontal velocity (V_x) distribution along the discontinuous lines 1-1 and 2-2 (depicted in the Figure 5.10).

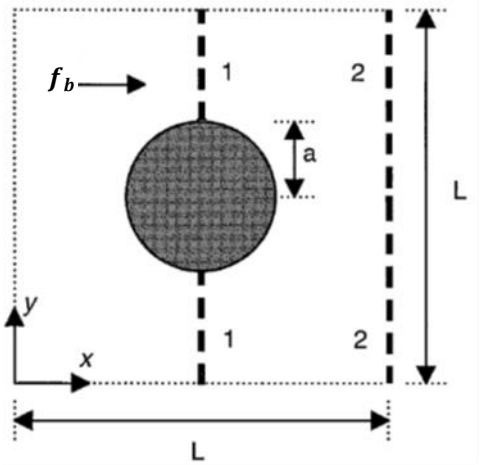

Figure 5.10 Flow past a single cylinder within a periodic lattice from (Morris et al. 1997)

The Figures 5.11 and 5.12 show the numerical results obtained for Reynolds numbers 1 and 0.03 respectively. In these figures, SPH results are compared with standard FEM results. As it can be noted from Figures 5.11 and 5.12, the SPH results compare well with that of FEM. The average value of the relative error considering all the particles in the domain with *Re*=1 is 0.42%. While the average value of the relative error for *Re*=0.03 is 0.54%. Therefore, the results obtained with higher Reynolds number demonstrates better comparison with FEM results.

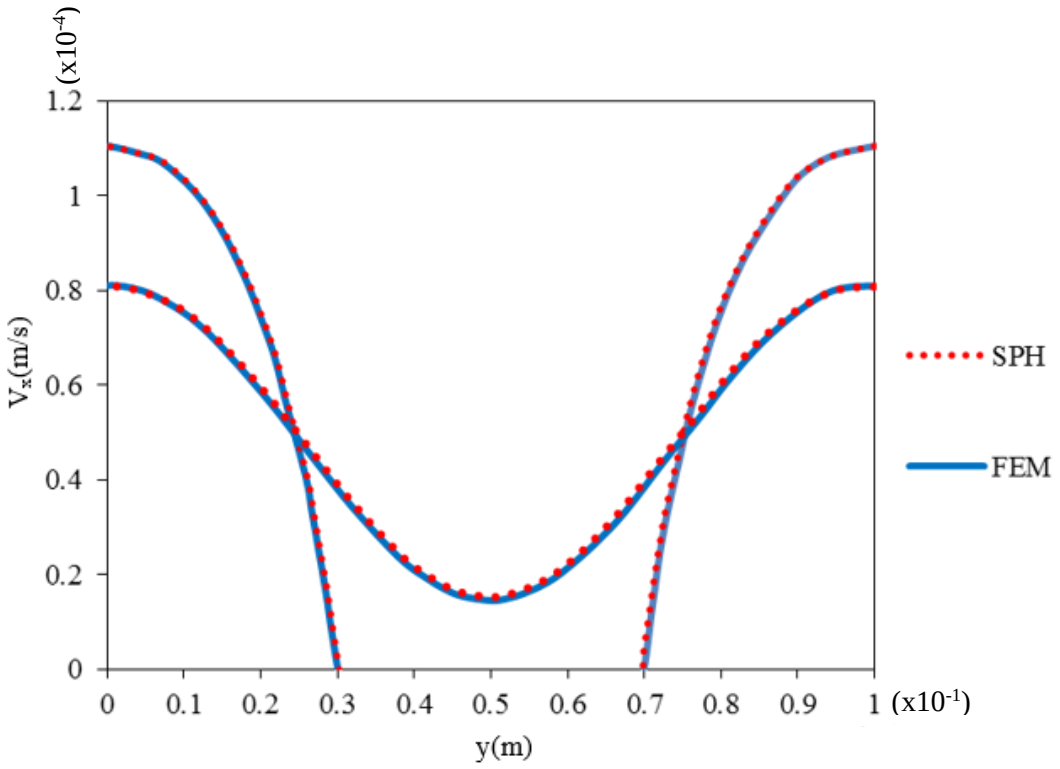

Figure 5. 11 Comparison of velocity distributions (Re = 1) along sections 1-1 and 2-2

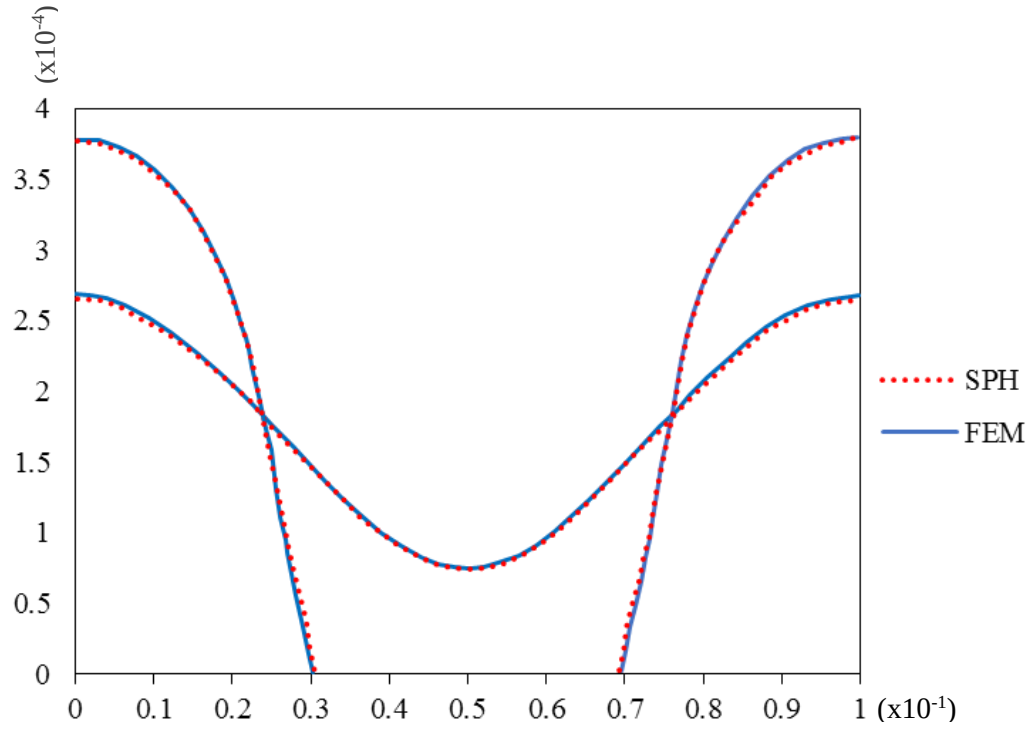

Figure 5. 12 Comparison of velocity distributions (Re = 0.03) along sections 1-1 and 2-2

5.2.5 Downstream-Facing Step Flow Channel

This test is an important benchmark example as it contains sudden change of cross-sectional area at the step, in combination with channel flow characteristics away from the step. Therefore, successful simulation of this benchmark can further establish the accuracy and applicability of the developed methodology for simulating blood flow in arteries. The geometrical domain adopted (Denham 1974) for downstream-facing step flow is illustrated in Figure 5.13. In this numerical simulation, a constant body force is applied to drive the flow at the entrance of the channel, where the body force is set to obtain a mean bulk velocity in the channel above the step at two different Reynolds numbers (i.e. Re = 73 and Re = 229) were simulated. Here, the Reynolds number is given by $Re = \frac{V_o h}{\nu}$, where h is the height of the channel entrance, V_o is the velocity at entrance of the channel (V_o = $2.4\ \text{X}\ 10^{-3}\text{ms}^{-1}$ and V_o = $7.6\ \text{X}\ 10^{-3}\text{ms}^{-1}$). The density and dynamic viscosity of the numerical simulations were chosen as $1000\,\text{kg/m}^3$ and $1\,\text{x}\,10^{-6}\ \text{m}^2\text{s}^{-1}$ respectively. At the start of the simulation, fluid domain was discretised with uniform spacing between particles ($\Delta x = \Delta y = 1$ mm). The velocity distribution at two different locations (x = -20mm and x = 90mm) along the downstream are depicted in Figures 5.14 and 5.15. It can be noted from these figures that the numerical results compare well with the experimental results presented in (Denham 1974). In addition, Tables 5.2, 5.3, 5.4, and 5.5 give the numerical values of corresponding convergence velocities at chosen positions along each location (x = -20mm and x = 90mm).

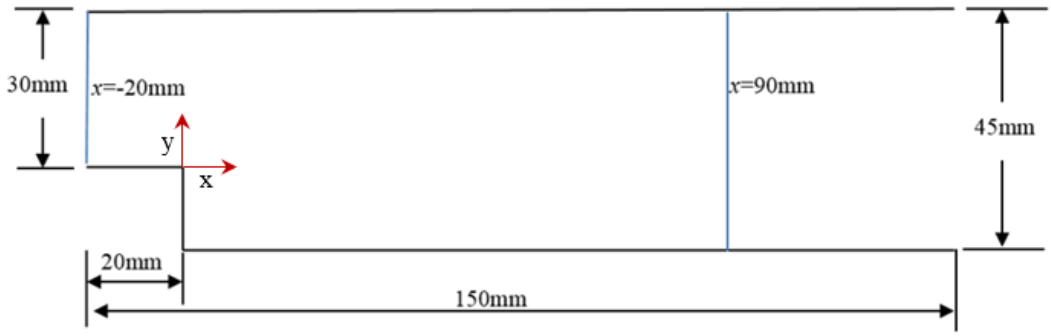

Figure 5.13 Geometrical configuration of problem domain

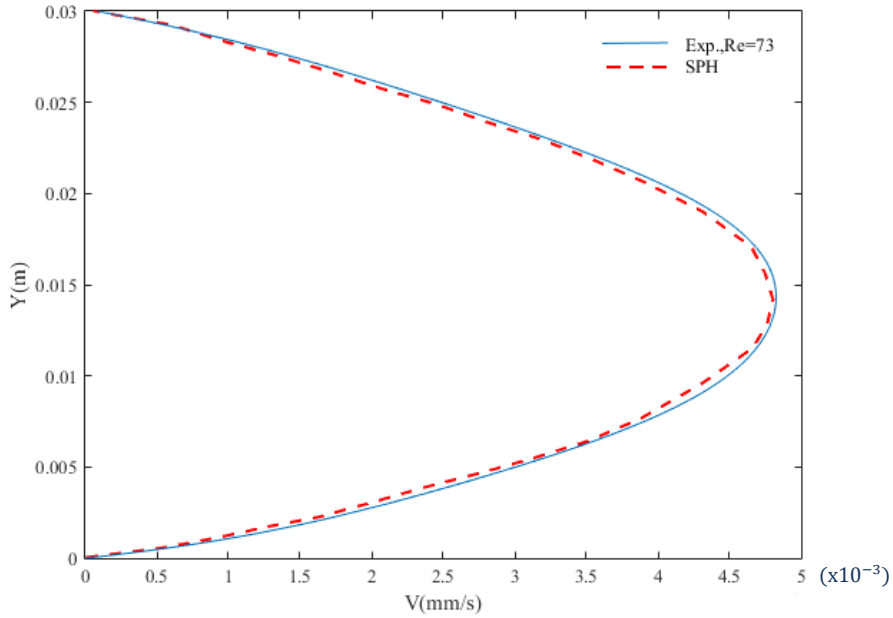

(a)

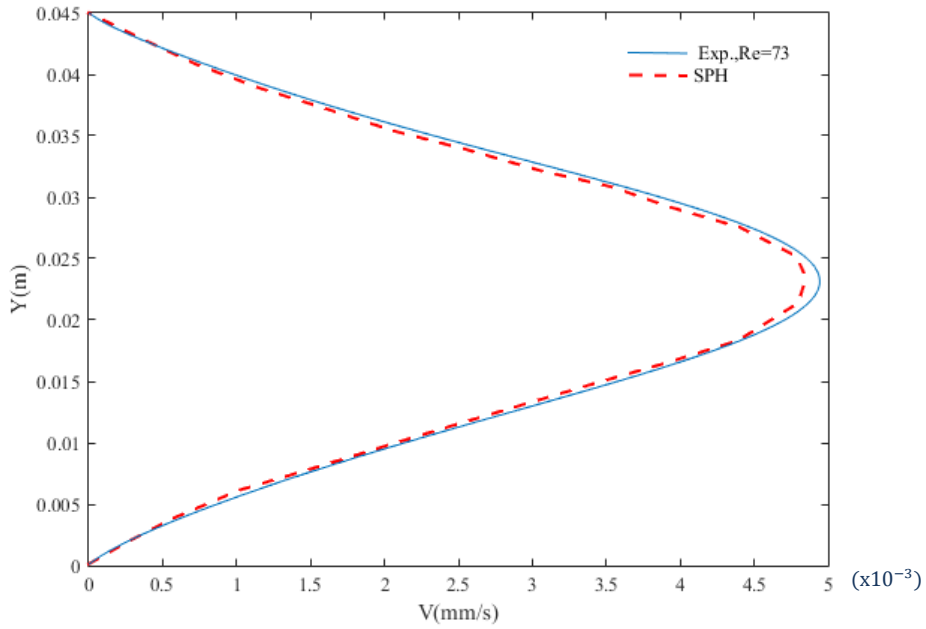

(b)

Figure 5.14 Comparison of the velocity profiles (Re=73) at (a) *x*=-20mm and (b) *x* = 90mm

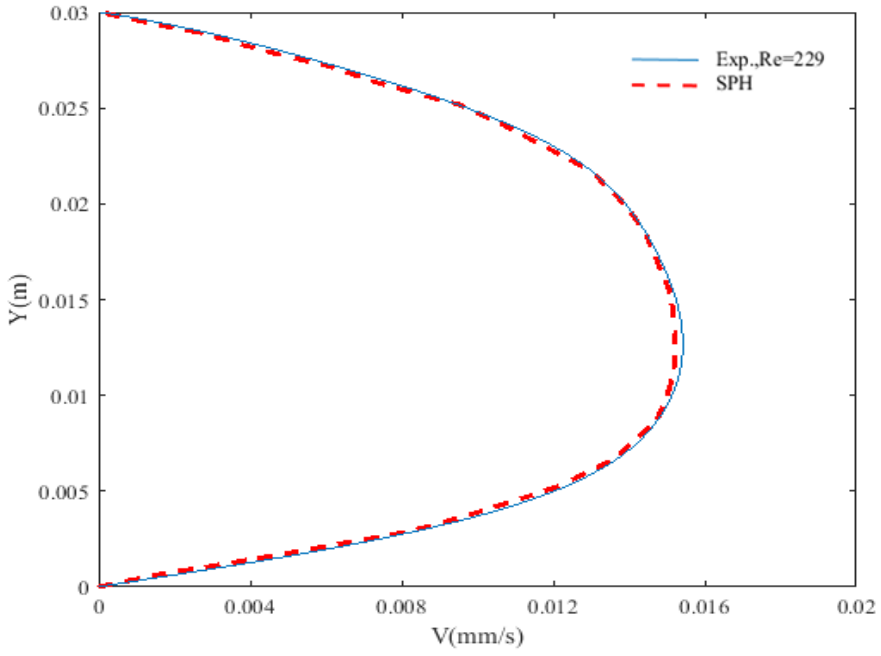

(a)

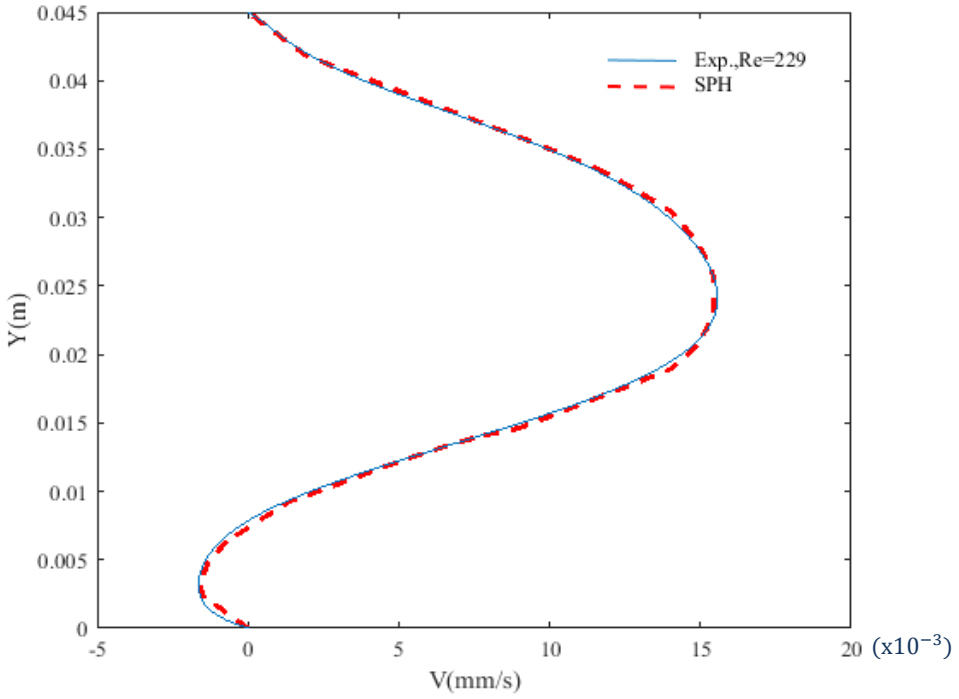

(b)

Figure 5.15 Comparison of the velocity profiles (Re = 229) at (a) *x*=-20mm and (b) *x* = 90mm

Table 5. 2 Converge velocities (*Re*=73) at x=-20

Position (y)	**% different in velocities with respect to Experiment**
0.015	0.80
0.02	0.016
0.025	0.026
0.03	0

Table 5. 3 Converge velocities (*Re*=73) at x=90

Position (y)	**% different in velocities with respect to Experiment**
0.025	1.62
0.03	2.15
0.035	3.66
0.04	3.43

Table 5. 4 Converge velocities(*Re*=229) at x=-20

Position (y)	**% different in velocities with respect to Experiment**
0.015	0.92
0.02	0
0.025	0.0093
0.03	0

Table 5. 5 Converge velocities (*Re*=229) at x=90

Position (y)	% different in velocities with respect to Experiment
0.025	1.160
0.03	0.65
0.035	0.018
0.04	0.054

The numerical simulations of benchmark test cases that have been presented in this chapter so far have demonstrated the capability of the computational model developed. In addition, the effect of particle resolutions on the accuracy of the computed results was promising. The next sub-section focuses on the application of SPH methodology for blood flow simulation. For this purpose, the blood flow through a bifurcation artery is considered. This simulation is performed here to explore the accuracy of the proposed SPH method in modelling blood flow through arteries.

5.3 Flow Inside a Bifurcation Artery

It is known from the clinical diagnosis that some regions in the artery are considered to be very susceptible to the formation of an atherosclerotic lesion. The predilection to form the atherosclerotic plaques in regions of a vessel bifurcation, ostia and curvature is an important recognised fact. Clinical studies can confirm that atherosclerosis chooses different locations in the vascular system, such as primarily sited in the carotid arteries, coronary arteries, and in vessels supplying the lower

extremities in the arterial system(Yazdani 2003). Atherosclerosis is one of the vascular pathologies that is considered to be a prominent disease. Atherosclerosis can affect medium-sized or large arteries (Waite and Fine 2007). Therefore, the hemodynamic phenomenon can be considered to be an important factor among the list of possible initiating factors in the formation of atherogenesis. The local hemodynamic can be viewed as having a vital effect on the expansion of the atherosclerotic lesion in the sinus of the carotid bifurcation (Caro et al. 1971; Friedman et al. 1981; Zarins et al. 1983; Nerem 1992). Although the exact mechanism of this disease is indistinct, a number of hypotheses have been suggested to relate hemodynamical forces to the location of atherosclerotic lesions. For instance, the high and low shear stress theories respectively of Caro et al. and Fry (Caro et al. 1971; Fry 1973; Caro 1982) provide various descriptions. It has been suggested that local variations in the samples of the blood flow behaviour, specifically boundary layer separation, takes an important role in atherogenesis (Fox and Hugh 1966). Then, Caro et al. (Caro et al. 1971) modified Fox and Hugh's theory (Fox and Hugh 1966) and showed that the early lesions are more likely to develop in regions with low shear stress because of the shear-dependent mass transport mechanism for atherogenesis. Meanwhile, Fry (Fry 1973) showed that the early atherosclerotic lesions appear in the regions with high shear stresses, which were found to induce endothelial injury. In addition, Friedman et al. (Friedman et al. 1993) explained that the disease begins with a thickening of the intimal layer in locations that connect with the shear stress distribution on the endothelial surface. Atherosclerosis is a disease that classifies one of the diseases of the arterial wall which refers to be influenced by hemodynamics (Bronzino 1999). The rheological properties of the blood flow are not simply controlled by pressure pulse, the

properties of the arterial wall, and the geometry of the bifurcation, but they are also controlled by the local hemodynamic (Gijsen 1998). Bronzino (Bronzino 1999) showed the outer walls of bifurcations and the inner walls of curvatures have localised regions that are characterised by relatively low blood phase transport rates in which leads to accumulation of lipid in the arterials thus causing atherosclerosis. Clinical and postmortem anatomical studies have also discovered that atherosclerotic lesions in humans increase along the inner wall of the curved artery and the outer walls of bifurcations of relatively large arteries (Kerber et al. 1996; Malek et al. 1999). This happens because the blood flow is changed by the appearance of flow separation and creation of complex recirculation flows (Motomiya and Karino 1984; Wada and Karino 2002). Where observed, the disturbed flow in the regions of the separation and reattachment points has a major effect on atherosclerosis (Yazdani 2003). A large number of publications in the scientific community indicate that there is a strong interest in understanding the flow behaviour in arteries. In particular, the flow behaviour in a bifurcation artery is considered to be of great interest when studying the atherosclerosis diseases with respect to both the genesis and the diagnostics of atherosclerotic diseases. Thus, a deeper understanding and explanation of the flow behaviour in that area would be an important chance to support the early discovery of many diseases. In addition, low shear stress areas are related to the development of atherosclerotic diseases. Despite the importance of other factors, such as chemical and physiological factors, the localised atherosclerotic lesions must be connected to the local flow conditions, as is the case for another factor can be considered in a well-mixed condition; that is, uniformly distributed along the vessels. Furthermore, the flow of blood through healthy vessels can influence the formation of deposits, where the appearance of plaques will lead to a change of the

hemodynamics in the vicinity of the lesion. Many studies have dealt with the flow inside the artery using either experimental or numerical simulations (Bharadvaj et al. 1982; Perktold and Hilbert 1986; Rindt et al. 1990; Rindt and Steenhoven 1996; Palmen et al. 1997). Meanwhile,(Kleinstreuer 1989; Jou and Berger 1998) presented a study to investigate the effects of pulsatility and bifurcation angle. The numerical simulations dealing with the flow inside the bifurcation artery were mostly based on conventional mesh-based methods: such as finite elements (Perktold and Rappitsch 1995; Gijsen et al. 1999; Chen and Lu 2004), while an experimental and numerical review of bio-fluid dynamic studies of the arterial bifurcation was presented by (Lou and Yang 1991). Most of the numerical studies were performed by treating the walls of the bifurcation artery as rigid walls. Meanwhile, a few numerical studies (Perktold et al. 1991; Reuderink 1991; Perktold et al. 1992; Perktold and Rappitsch 1993) have considered the distensibility of the wall in their simulations. Coupling and integration of models with different dimensionality were applied (Formaggia et al. 1999; Quarteroni 2001). These researchers worked to link the lumped models with 3D models of the arterial tree. Another study has investigated the pulsatile flow of non-Newtonian fluid in a bifurcation model with a non-planar daughter branch (Chen and Lu 2006). These authors used the Carreau–Yasuda model to examine the shear thinning behaviour of the analogue blood fluid. Moreover, a numerical study examined the effects of Newtonian and Non- Newtonian blood flow on local hemodynamics in a multi-layer carotid artery bifurcation (Nikparto and Firoozabadi 2011). These previous studies have demonstrated that the flow behaviour is sensitive to the geometry of the bifurcation artery, such as the complex geometry of the branch, flow division between the branches, pulsatile nature of the flow,

distensibility of the arterial wall, and Newtonian or non-Newtonian characteristics of blood.

As a mesh-free method, the SPH can be used in simulating a flow inside complex geometrical domains. This example was chosen to explore the fluid dynamics phenomena in a bifurcation artery and to explore the accuracy of the proposed SPH method, in simulating blood flow through complex arterial geometry.

A 2-D model was used in this numerical test and the simulations were executed under pulsatile flow conditions similar to that of physiological conditions. The geometrical configuration of a bifurcation artery described by (Gijsen et al. 1999) is illustrated in Figure 5.16. The geometry of bifurcation artery consists of three main regions namely, common carotid, internal carotid, and external carotid. It can be noted from Figure 5.16 that the cross-sections of common and external carotid artery do not change during the flow. However, the cross-section of the internal carotid artery changes considerably during the flow. Therefore, the flow characteristics of the fluid moving within the internal carotid can vary over the time. It is important to study the effect of these variations on the flow characteristics to understand the physiological conditions associated with local hemodynamic. For this purpose, the axial flow through cross-sections located at A, B, C and D are investigated in this numerical simulation. The cross-section A is located in the middle of the common carotid artery. Meanwhile, the cross-sections B, C and D are located at different positions along (x'-axis) the internal carotid as shown in Figure 5.16.

To study the accuracy and convergence of the computed parameters, the numerical simulations were performed by discretising the fluid domain using three different particle resolutions (1000, 2000 and 5000 particles). The fluid was accelerated by a

pulsatile pressure variation to mimic realistic blood flow. The applied pulsatile pressure gradient can be interpreted as the effect of an external body force in the momentum equation. The equation of a pulsatile pressure gradient can be presented as (Aroesty and Gross 1972);

$$\frac{dp}{dx} = A_o(1 + Asin\omega t) \tag{5.10}$$

Where, ω is the imposed pulse frequency, A_o is component the pressure gradient, A is the amplitude of the imposed pulsatile pressure gradient, and t represents time. In the present simulations, A and ω were chosen as 0.3 and $2\pi/\mathrm{T}$, $\mathrm{T} = 0.72s$ is the period. And the viscosity and density of the fluid were assumed to be 2×10^{-6} $\mathrm{m^2 s^{-1}}$ and $1410\, kg/m^3$ respectively (Gijsen et al. 1999). And, the diameter of the common carotid was chosen as 8 mm. In the numerical simulations, no-slip boundary condition was imposed at the rigid walls and the periodic boundary treatment was used between inlet and outlet boundaries.

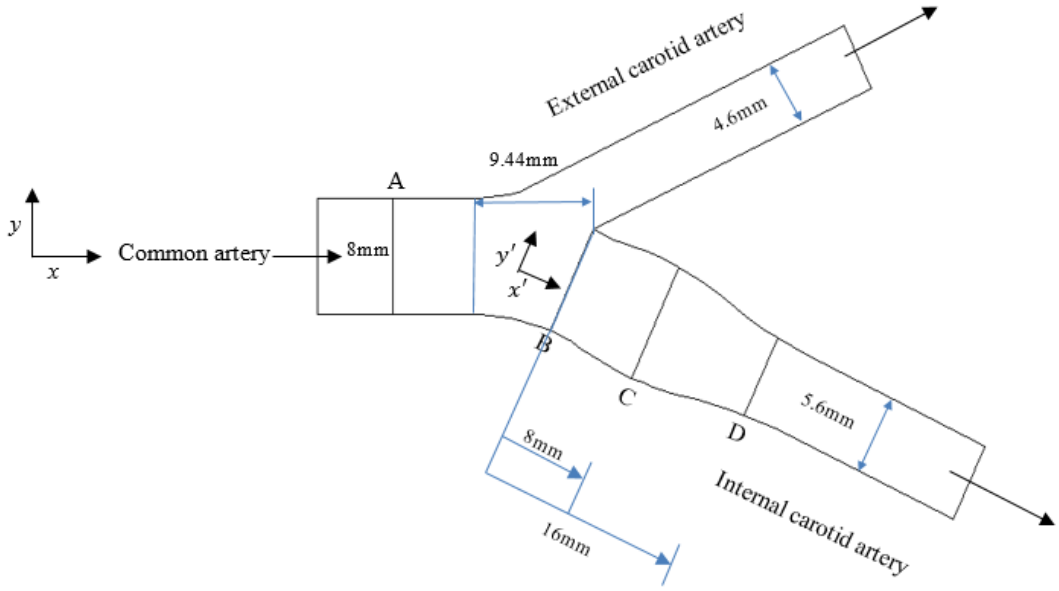

Figure 5.16 Geometry of the bifurcation artery (Gijsen et al. 1999)

During the numerical simulations, the velocity distributions across locations A, B, C and D were plotted at $t = 0.2s$ (i.e. $t = \mathrm{T}/4$). Figure 5.17 shows the velocity profile across the common carotid at location A. The axial velocity computed across the common carotid at location A exhibited a parabolic distribution. In Figure 5.17, the results obtained from SPH simulations are compared with the experimental observations reported in (Gijsen et al. 1999).

The flow in the internal carotid sinus artery is considered to be very complex due to its geometry. Figures 5.18, 5.19 and 5.20 illustrate the comparison between velocity profiles obtained numerically and experimentally at locations B, C and D across internal carotid sinus artery. All the figures confirm that the numerical results agree well with the velocity distribution obtained from previous experiments (Gijsen et al. 1999). In addition, these figures also illustrate the effect of SPH particle resolution (i.e. number of points used) on the convergence of the numerical results.

As predicted, the flow inside the internal carotid sinus artery was observed to be very complex due to its geometry. It can also be noted from Figure 5.16 that the cross-sectional area of the internal carotid artery gradually increases from location B till location C and then gradually decreases from location C till location D. The effect of this variation in the cross-sectional area of the velocity distribution can be seen from Figures 5.18, 5.19 and 5.20. As revealed by the figures, till location C, the velocity of the flow inside the internal carotid artery was decreased because of the increase in cross-sectional area and the maximum value of the velocity was reached at location D. Further, the Figure 5.18 exhibits high gradients of velocity distribution due to the change of cross-sectional area at location C. It is clearly evident from the figures that the numerical results compare well with the experimental observations

reported in (Gijsen et al. 1999). In addition, Tables 5.6, 5.7, 5.8, and 5.9 provide numerical values of corresponding convergence velocities at chosen positions along each cross-section A, B, C and D.

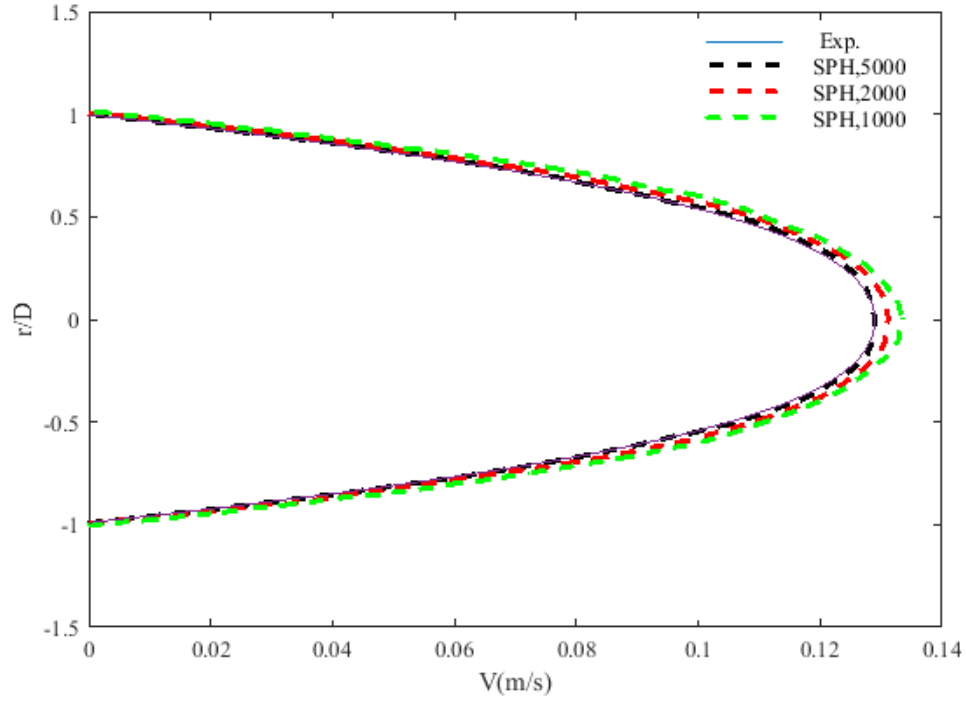

Figure 5. 17 Comparison of the velocity profile at location 'A' across common artery

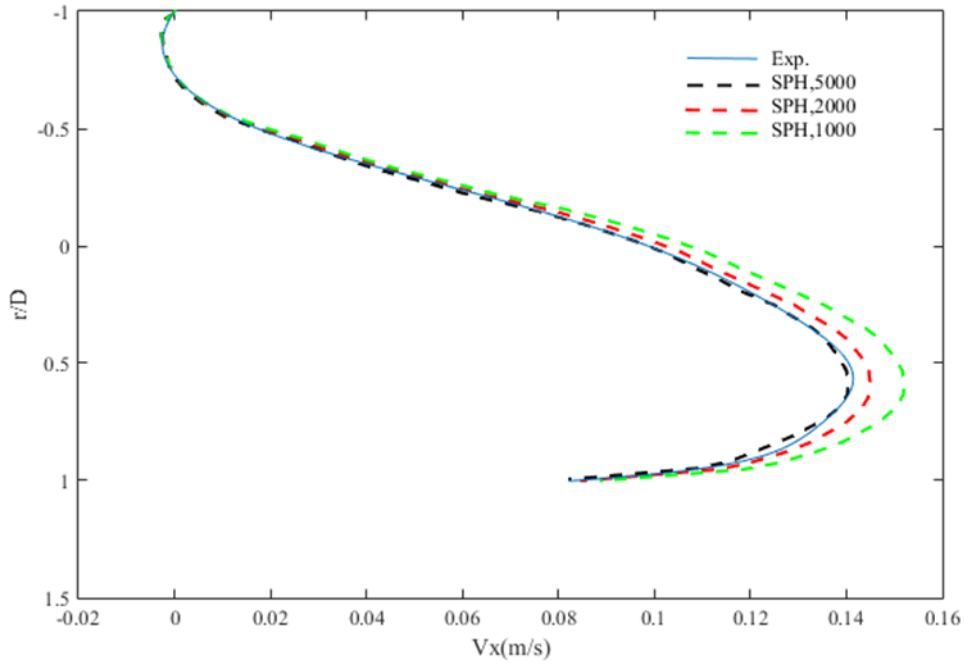

Figure 5. 18 Comparison of the velocity profile at location 'B' across internal artery

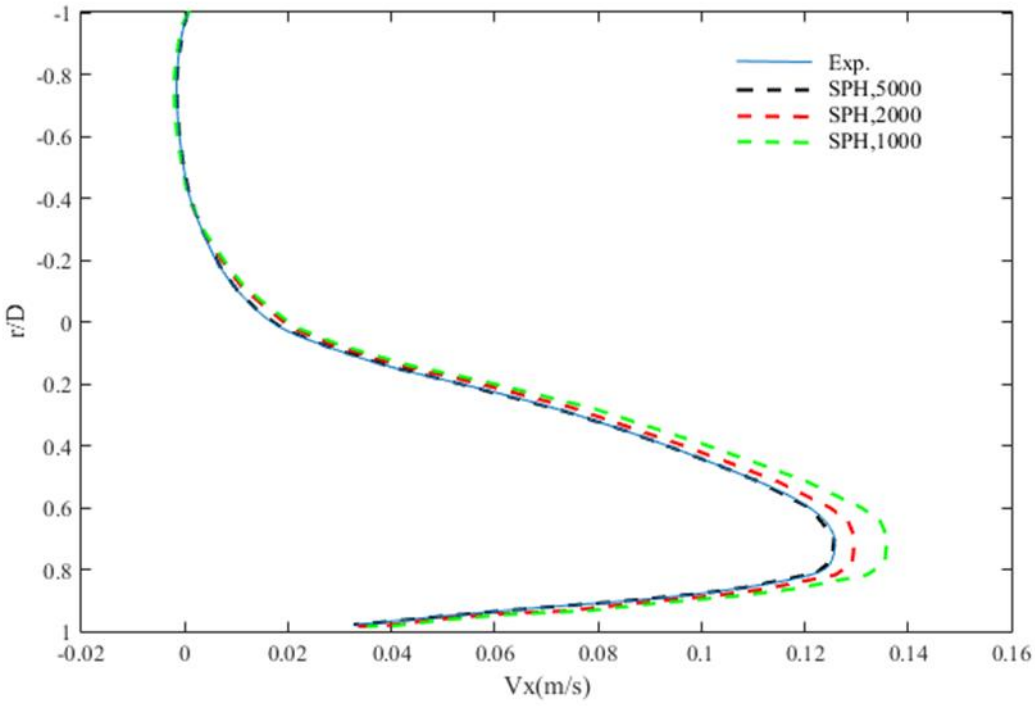

Figure 5. 19 Comparison of the velocity profile at location 'C' across internal artery

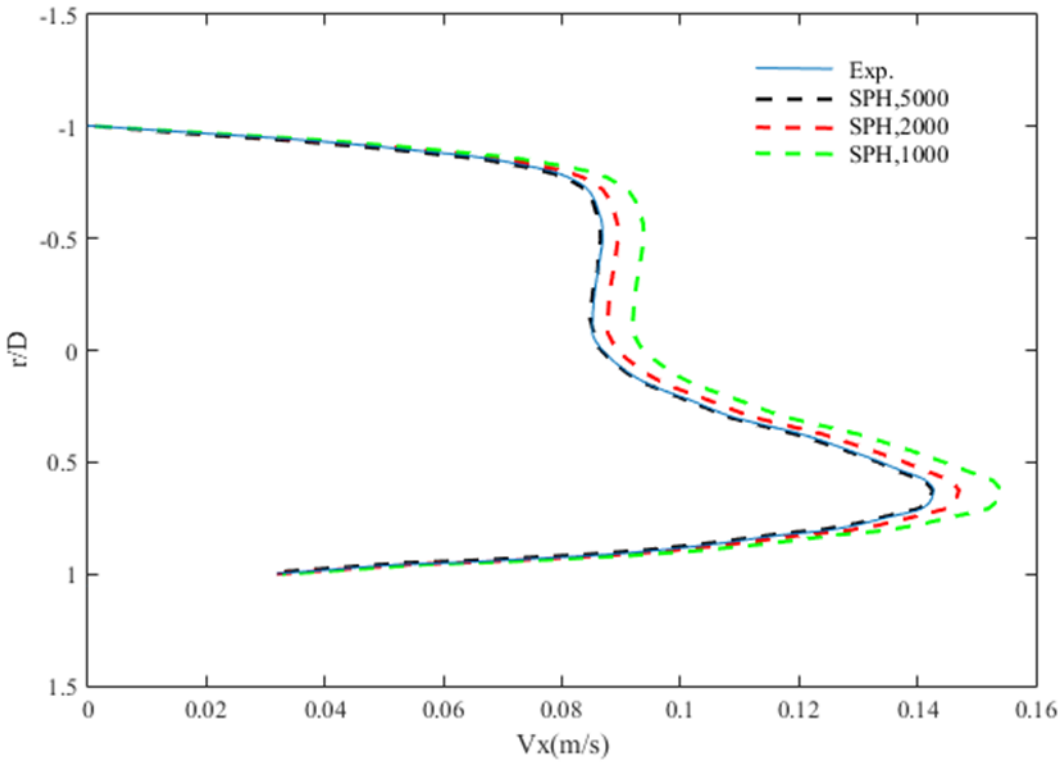

Figure 5. 20 Comparison of the velocity profile at location 'D' across internal artery

Table 5. 6 Converge velocities at section A

Position (r/D)	**% different in velocities with respect to Experiment**		
	SPH (1000)	SPH (2000)	SPH (5000)
0.4	0.29	0.29	0.19
0.2	2.73	1.67	0.35
0	3.84	2.09	0.34
-0.2	2.73	1.67	0.35
-0.4	0.29	0.29	0.19

Table 5. 7 Converge velocities at section B

Position (r/D)	**% different in velocities with respect to Experiment**		
	SPH (1000)	SPH (2000)	SPH (5000)
0.4	0.14	0.13	0.13
0.2	0.13	0.12	0.12
0	0.10	0.10	0.09
-0.2	0.06	0.06	0.06
-0.4	0.03	0.03	0.02

Table 5. 8 Converge velocities at section C

Position (r/D)	**% different in velocities with respect to Experiment**		
	SPH (1000)	SPH (2000)	SPH (5000)
0.4	0.09	1.63	0.0005
0.2	0.05	6.99	0.002
0	0.01	0.01	0.01
-0.2	0.006	0.05	0.27
-0.4	0.0005	0.09	0.13

Table 5. 9 Converge velocities at section D

Position (r/D)	**% different in velocities with respect to Experiment**		
	SPH (1000)	SPH (2000)	SPH (5000)
0.4	0.13	0.12	0.12
0.2	0.10	0.10	0.09
0	0.09	0.08	0.08
-0.2	0.09	0.08	0.08
-0.4	0.09	0.08	0.08

5.4 Conclusion

This chapter focused on the application of numerical procedures proposed in Chapter 4 in simulating fluid flow under various physical and boundary conditions. The numerical test cases were chosen such that the accuracy of the proposed methodology could be assessed under various flow conditions. In addition, the selected cases have similarities with geometries and flow characteristics commonly found in the human circulatory systems.

At first, the developed SPH based methodology was used in a number of standard computational fluid dynamics test cases to assess accuracy and convergence characteristics. The results of the numerical simulations confirmed that the proposed methodology was successful in yielding sufficient accuracy. In addition, the convergence of the numerically computed results towards either analytical or experimental result was successfully demonstrated. Finally, blood flow through an

artery was simulated using the proposed numerical methodology. To investigate the flow through a realistic blood vessel, a bifurcation artery geometry was chosen as the flow domain. During the simulation of flow through the bifurcation artery, the results of the numerical simulation were compared with experimentally observed data. The numerical results compared well with the experimental results and demonstrated that the SPH method could be applied to flow simulation with complex boundaries. Although the blood flow simulations in this chapter were performed under 2-D geometrical setting, the proposed methodology can be extended to the 3-D framework. This chapter has demonstrated that the developed SPH methodology is able to accurately capture the salient features of blood flow dynamics within various vessel geometries. Given that fluid dynamics play an important role in thrombus formation, the numerical implementation can now focus on developing a suitable computational procedure to simulate thrombus formation. The next chapter delves into the simulation of thrombus formation using the developed SPH method to investigate the influence of flow parameters on thrombus formation.

Chapter 6

Numerical Simulation of Thrombus Formation

6.1 Introduction

The formation of thrombus in blood vessels is a process that influences various pathological conditions, including cardiovascular ischemia, cerebrovascular accidents and prevention of bleeding (due to the damaged vessel). This chapter explores the feasibility of modelling thrombus formation using smoothed particles hydrodynamic (SPH) method and investigates the influence of blood flow on thrombus growth. First, a brief introduction of thrombus and elements involved in its formation are presented in this chapter. Next, a computational model which is adopted in the present work to simulate the formation of a thrombus is described. Finally, the results of the numerical simulations performed to investigate the formation of thrombus within vessels of different wall geometries and for various blood flow velocities are presented.

As described in Chapter 2, a thrombosis is the formation of a blood clot inside a blood vessel, which can cause an obstruction to the circulatory system. Over the years, many studies have tried to analyse or explain thrombogenesis, beginning in the 1840s with the investigations of Rudolf Virchow. A thrombosis can appear at many different locations in the circulation and it is strongly influenced by the local fluid mechanics (Caro 2012). Thrombosis is considered to be one of the important causes of cardiovascular diseases. Arterial thrombosis is one of the thrombus diseases that have been found to overlay ruptured atherosclerotic plaques. According to a study conducted by the World Health Organization (WHO), approximately 17.7 million people worldwide die due to cardiovascular diseases every year, in which heart attacks and strokes have the most occurrences. Around 50% of sudden deaths are due to cardiac causes (Kochanek et al. 2004). Studies have shown that there is a link to

acute myocardial infarction caused by coronary thrombosis or to an arrhythmia arising within a scarred left ventricle (Davies et al. 1989). Acute ventricle tachyarrhythmia accounts for 80% of sudden deaths, which is caused by acute coronary events (Huikuri et al. 2001). Most of these deaths occur in persons without prior cardiac symptoms or signs (Myerburg et al. 1998). These studies reveal that sudden death can be caused by a mural thrombosis, which plugs the lumen and restricts blood flow distally. Consequently, the blood flow is decreased and the heart muscles reach a low oxygen state. Due to ischemia, there is no return flow of blood. This can then lead to an irreversible infarct in the myocardium. During this time, the tissue that is ischemic does not introduce electrical signals to enable contractions in the heart ventricles and leads to an arrhythmia, which causes heart arrest and consequently results in death (Flannery 2005). A total of 70% of cardiac deaths around the globe are due to thrombosis (Panteleev et al. 2014). Thrombosis in the deep veins is considered to be one of the main global health problems (Tapson 2008). Thrombosis is considered as the most distinguished of the haemostatic disorders, which is exhibited by the formation of a blood clot that blocks the blood flow in the vessels. Thrombus formation causes many types of diseases and conditions, such as atherosclerosis, trauma, stroke, infarction, cancer, sepsis and others. The formation of a thrombus depends on platelet activity, such as the transport to denuded subendothelium, a formation of membrane tethers, adhesion to the subendothelium, and aggregation. (Ruggeri 2002; Ruggeri 2003). In blood circulation, the platelets do not normally adhere to the wall of the blood artery or vessels, to other cells, or to each other. However, if the wall of the vessel is damaged, then platelets will rapidly adhere and accumulate on the damaged wall.

In physiological conditions, platelets are considered to be one of the most important elements for causing haemostasis (Broos et al. 2011; Nuyttens et al. 2011).When an imperfection or damage is recognised, the platelets react with adhesion. The procedure of initial platelet-plug generation is called primary haemostasis. Low platelet numbers may impede the primary haemostasis and this can lead to an extreme increment of cessation times (Reininger 2008). Platelets play an important role in primary haemostasis, which has three functions: adhesion, activation, and aggregation. Adhesion of platelets occurs on the subendothelium. Many receptors can interact with subendothelial components, such as collagen, to facilitate adhesion to the damaged vessel wall. Then, the platelets change to activated phase thanks to different chemical agonists, such as thrombin, collagen and ADP. The last stage is the aggregation phase, which indicates the accumulation of platelets. This is considered to be an essential requisite for the formation of a platelet-plug (Flannery 2005; Broos et al. 2011; Nuyttens et al. 2011). During secondary haemostasis, the accumulation of aggregation platelets results in a plug. This is then further settled by, for example, fibrinogen fibres compared to the primary thrombosis (Müller 2015).

Thrombosis is principally connected to hemodynamics because blood transports cells and proteins to the thrombus, which upholds stresses that may disturb the thrombus (Wootton and Ku 1999). Many parameters are affected by the formation of thrombogenesis, which are either fluid mechanical factors or one of many physiological reactions. For example, platelet membrane glycoprotein (GP) is activated by the shear rate of blood flow (Andrews et al. 1997), which will affect the quantity of the adhesion of platelets to the subendothelium (Begent and Born 1970; Ruggeri et al. 1999). Thrombosis is extremely influenced by blood flow (Bronzino 1999). The blood flow is considered an active contributor to creating a thrombus

through platelets and their interaction with other materials in the blood. Therefore, thrombus formation is affected by the blood flow velocity (Tosenberger et al. 2012).

Following this brief account of the factors involved in thrombus formation, the following sections of this chapter will focus on using meshless particle-based Lagrangian numerical technique named SPH method to explore the blood flow behaviour and flow conditions that determine thrombus formation and its characteristics. Due to its simplicity and effectiveness, the SPH method is employed here to simulate the process of thrombogenesis under the influence of various blood flow parameters. In the present SPH simulation, blood is modelled by particles that have the characteristics of plasma and platelets. Flow simulations were conducted with different Reynolds numbers. The results obtained from the numerical simulations are compared with experimental results to validate the accuracy of the proposed methodology.

6.2 Modelling Thrombus Formation

This section aims to detail the modelling techniques adopted for platelet motion and aggregation during the various phases of thrombus formation. To model platelet motion and aggregation, a suitable numerical procedure has to be coupled with flow equations developed in Chapters 3 and 4.

The platelets tend to adhere and aggregate when a blood vessel is damaged. This can lead to the formation of primary thrombus. Inside thrombus, the neighbour platelets link together, which are then bound by vWF fibrinogen in plasma and collagen in the subendothelial tissue (Savage et al. 1996; Schmugge et al. 2003). To numerically model such platelet motion, an algorithm based on a penalty or spring

force mechanism is adopted (Kamada et al. 2010). This model dictates the interactions between platelets and plasma inside the blood vessel. When the platelets are within a distance d_{ad} from the damaged area, the platelets move towards damaged area and adhere to the wall by an adhesive force defined by Eq. (6.1). The platelets that adhered to the wall are activated and attract other platelets which are within a distance of d_{ag} from them, as illustrated in Figure 6.1. This attractive force is called an aggregation force and is defined by Eq. (6.2). This aggregation force is algebraically similar to that of the adhesive force on the platelets but has a different spring constant compare to adhesive force.

$$\boldsymbol{F}_{ad} = \begin{cases} K_{ad}(|\boldsymbol{r}_{ij}| - r_o)\boldsymbol{n}_{ij} & (|\boldsymbol{r}_{ij}| \le d_{ad}) \\ 0 & (|\boldsymbol{r}_{ij}| > d_{ad}) \end{cases} \tag{6.1}$$

$$\boldsymbol{F}_{ag} = \begin{cases} K_{ag}(|\boldsymbol{r}_{ij}| - r_o)\boldsymbol{n}_{ij} & (|\boldsymbol{r}_{ij}| \le d_{ag}) \\ 0 & (|\boldsymbol{r}_{ij}| > d_{ag}) \end{cases} \tag{6.2}$$

where $\boldsymbol{F}_{ad}, \boldsymbol{F}_{ag}$ are the adhesive and aggregate forces, respectively, and K_{ad}, K_{ag} are the corresponding spring constants. In addition, $\boldsymbol{r}_{ij}$ here is the distance between activated platelet and vessel wall (or other non-activated platelets), r_o is the original or natural length of the spring and $\boldsymbol{n}_{ij}$ is a unit vector linking platelet and damaged wall (or linking activated platelet and other surrounding platelets). During the numerical simulations, the forces defined above are introduced in equation (4.2) as the external forces acting on platelet particles which are within the regions of influence of adhesion and aggregation forces.

Unless specified otherwise, the numerical procedure used for solving basic flow equations (4.1) and (4.2) are as described in Chapter 4. For example, the estimation of pressure and treatment of boundary conditions are performed in the

same manner as detailed in Chapter 4. The main addition to the solution procedure is the introduction of penalty forces which act on platelets those are subjected to adhesion and aggregation forces.

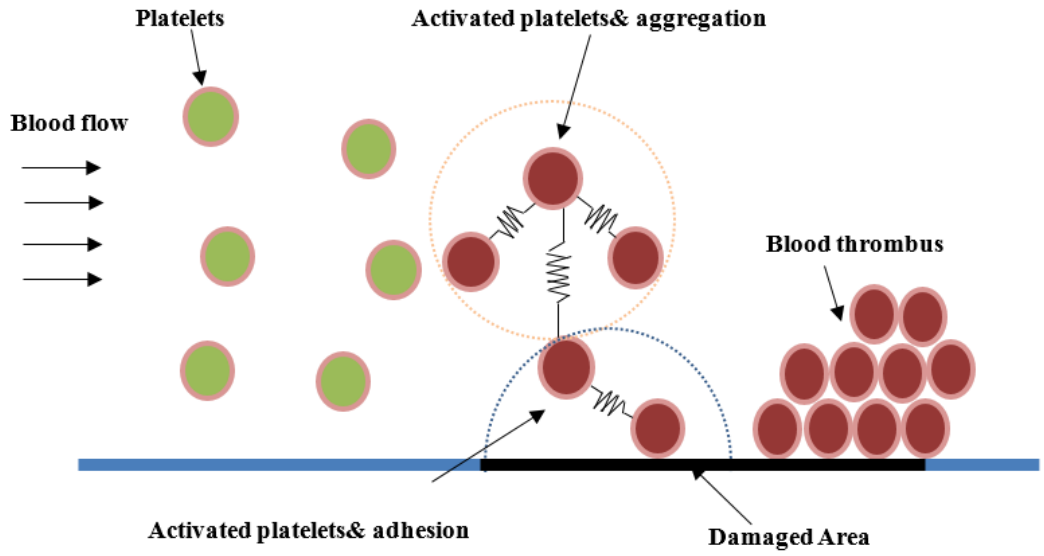

Figure 6.1 Method of platelet adhesion and aggregation at a damaged area of a vessel Blood Flow Model of Straight Vessel

In the following sections, a number of simulation test cases are investigated to determine the characteristics of thrombus formation based on the numerical algorithm proposed above. For this purpose, simulations of thrombus inside vessels of different geometries were also considered. The simulation results are compared with the experimental and analytical results. First, the simulations were performed inside a straight blood vessel. The influence of modelling parameters such as spring stiffness on thrombus shape and its formation was explored. Following this, thrombus formation inside the curved vessel, stenosis vessel and rectangular/tubular three-dimensional vessels were also investigated.

6.2.1 Straight Vessel Test

In this numerical test, the blood flow simulations were performed inside a straight blood vessel with different flow velocities between 100, 500 and 700 $\mu m/s$, which were defined at the inlet of the vessel. The total length of the vessel (L) and the width between two walls (D) are, respectively, $130\mu m$ and $40\mu m$. The length of the damaged wall (L_i) is $30\mu m$, and the distance from the inlet to the damaged wall (L_o) is $40\mu m$ (see Fig.6.2). The total number of particles used in the simulation was 5371. The initial distance between particles in both directions is 1.0 μm. The density ρ and kinematic viscosity v of the plasma and platelets were set as $\rho = 1x10^3 kg/m^3$ and $v = 1x10^{-6} m^2 s^{-1}$. The boundary conditions were a uniform velocity at the inlet, zero pressure at the outlet and non-slip condition at the walls enforced by dummy boundary particles. The amount of platelet particles used is approximately 9 % of the plasma which is higher than normal physiological condition to reduce simulation time for thrombus formation. The time step of the simulation was set $5x10^{-7}s$ to ensure the stability of numerical integration scheme. After performing systematic repetitive simulations to achieve numerical results that were consistent with reported experimental observations (Begent and Born 1970), appropriate spring constant values were determined for adhesion and aggregation. The determined spring constant values for K_{ad} and the K_{ag} were $9.0x10^9$ N/m and $4.5x10^9$ N/m, respectively, while d_{ad}= 2.0 μm = d_{ag}, and r_o = 2.0 μm. Figures 6.2(a) and (b) show the initial configuration of the two- dimensional vessel model and the arrangement of the platelets and plasma in the fluid domain.

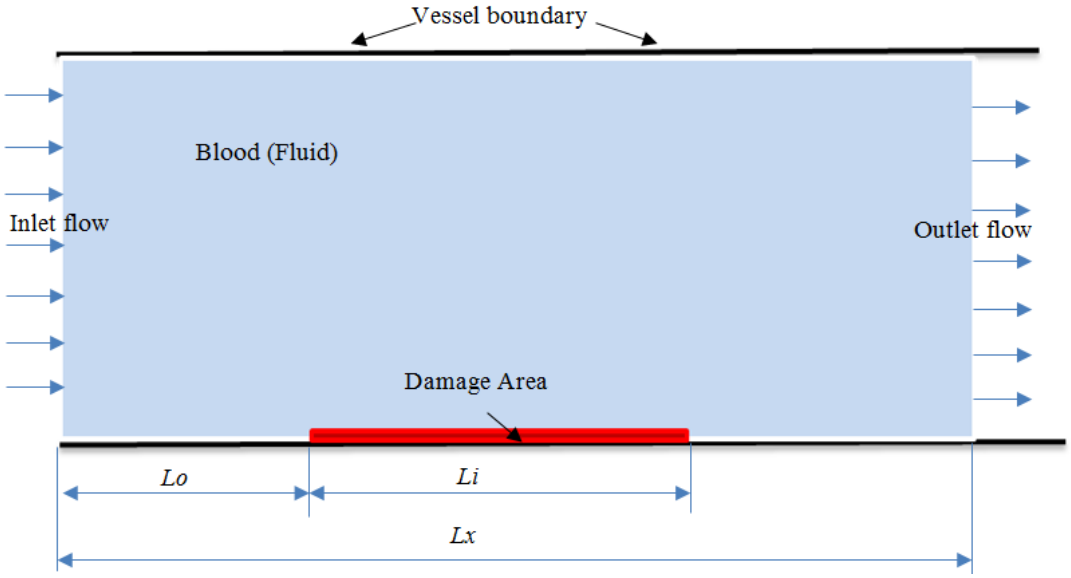

(a)

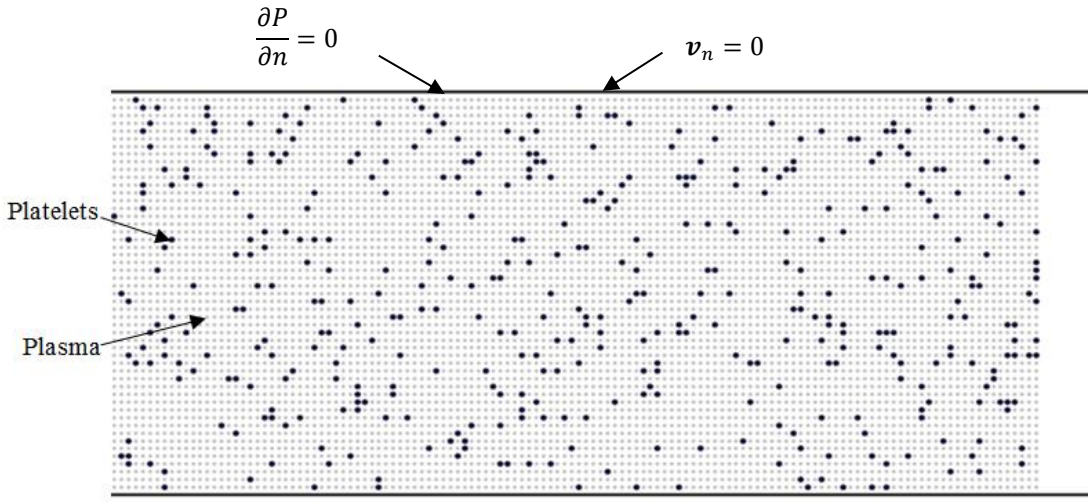

(b)

Figure 6.2 Schematic diagram of (a) a straight vessel (b) arrangement of particles

(*P*- pressure, v_n - normal velocity)

Normally, a thrombus is formed by adhesion and aggregation of platelets which are transported by the blood flow through different geometries of arteries or vessels, where the growth rate of thrombus formation varies with the stenosis and the flow rate of blood. Figure 6.3 illustrates the formation of thrombus at four different stages of the flow in a straight vessel. In these figures, for clarity, plasma and platelet particles are denoted by light and the dark grey, respectively. The platelets are

activated when they are within d_{ad} distance from the damaged region and form a primary thrombus. Meanwhile, the aggregation force acts between an adhered platelet and a neighbouring platelet particle that are separated by a distance less than the value of d_{ag} (as shown in Figure 6.1). During the course of time, a thrombus is developed to cover the whole damage area by forming several layers of platelets. When thrombus grows to a certain volume, a part of the thrombus is separated and transported downstream by the blood flow. Figures 6.3, 6.4 and 6.5 depict the growth of thrombus at different times for velocities 100, 500 and 700 $\mu m/s$ of the blood flow. From the figures below, various stages of thrombus growth on the damaged area of the wall are clearly evident. Figures 6.3(d), 6.4(d) and 6.5(d) illustrate that, a part of the thrombus is separated from the primary thrombus once the primary thrombus grows to a substantial volume. It is interesting to observe that the volume of the primary thrombus and the time at which separation of the thrombus takes place are influenced by the flow rate. From these figures, it can also be noted that when the flow rate was 700 $\mu m/s$ the thrombus growth was thinner compared to the cases where the blood flow rate was 100 and 500$\mu m/s$. Further, it was observed that with higher flow rates the separation of thrombus takes place quicker.

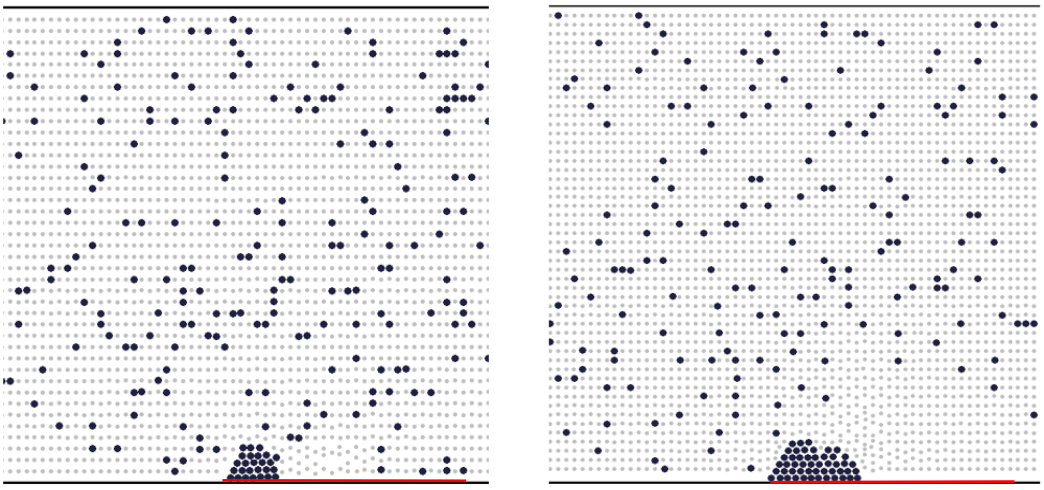

(a) (b)

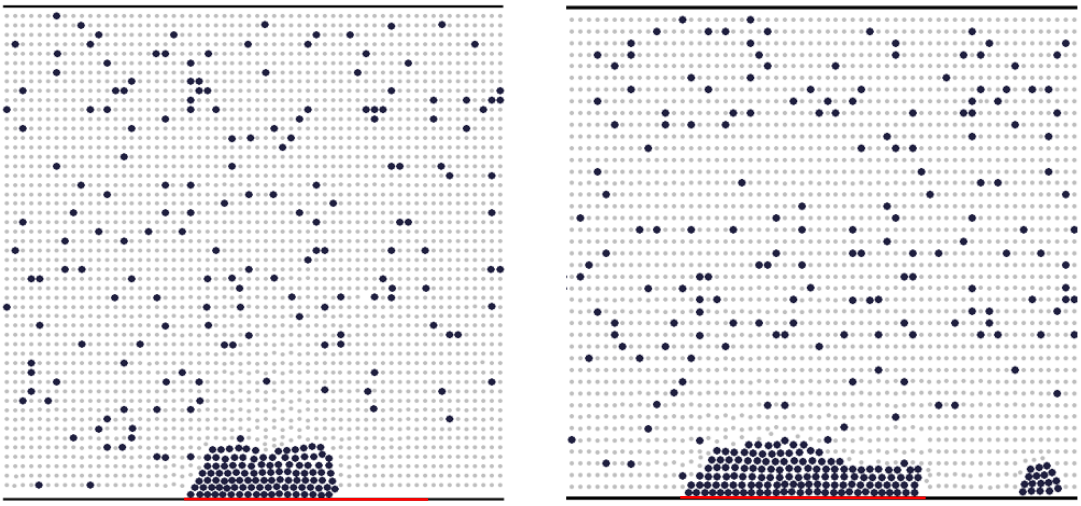

(c) (d)

Figure 6.3 The platelet aggregation for flow velocity =100 μm/s at (a) *t*=0.2s (b) *t*=0.3s (c) *t*=0.4s (d) *t*=0.6s

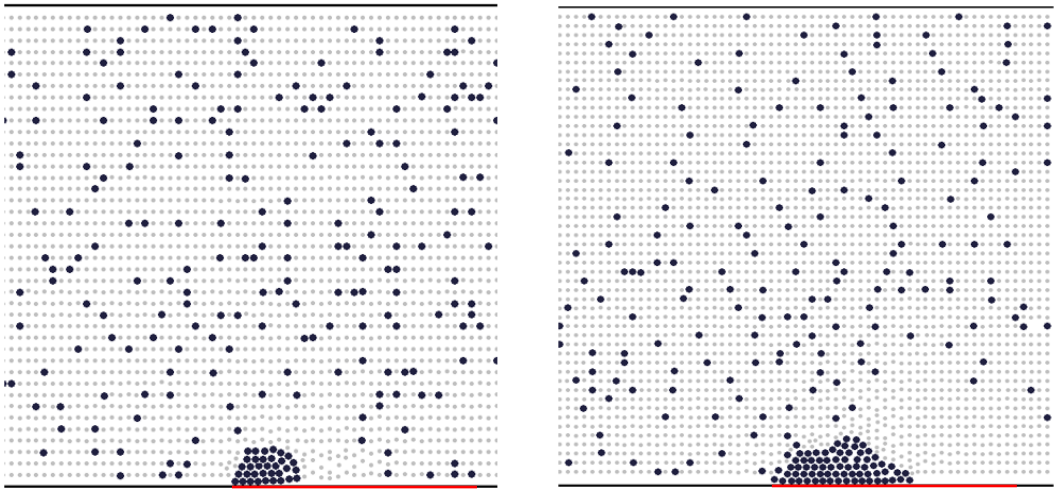

(a) (b)

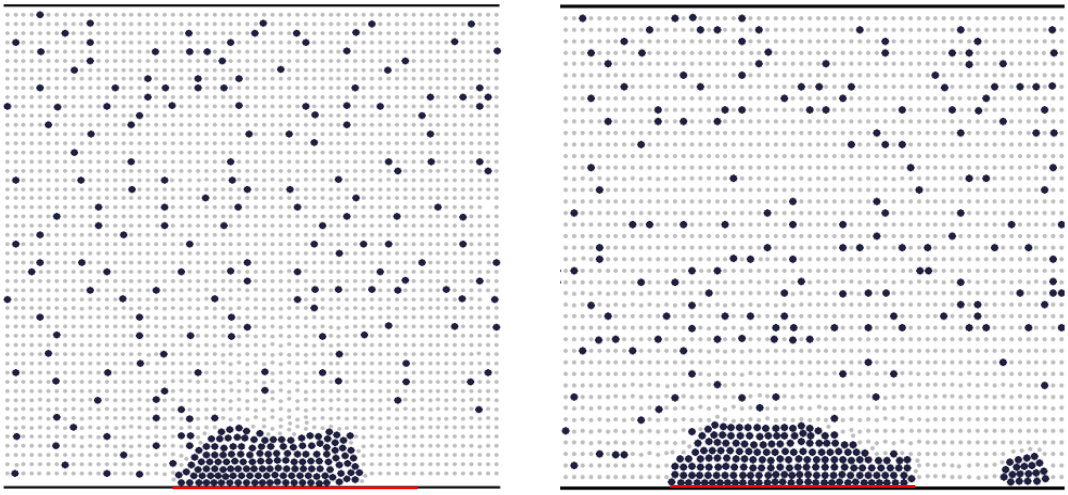

(c) (d)

Figure 6.4 The platelet aggregation for flow velocity =500 µm/s at (a) *t*=0.2s (b) *t*=0.3s (c) *t*=0.4s (d) *t*=0.6s

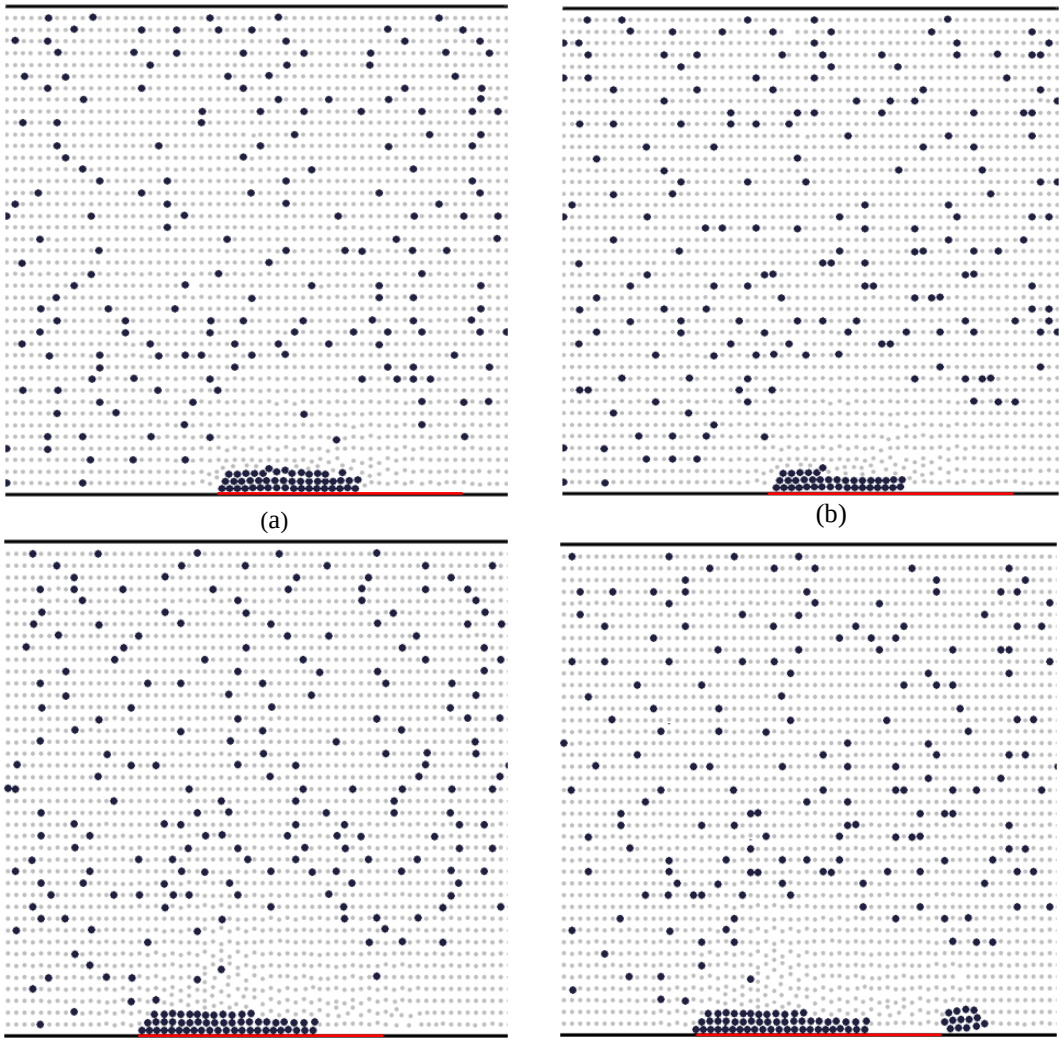

(a) (b)

(c) (d)

Figure 6.5 The platelet aggregation for flow velocity =700 µm/s at (a) *t*=0.2s (b) *t*=0.3s (c) *t*=0.4s (d) *t*=0.6s

Now, to validate the accuracy of the proposed model, thrombus growth rate and blood flow rate were further investigated and compared with data available in the literature. Figure 6.6 plots the growth rate of thrombus against various blood flow velocities. The growth rate of the thrombus in Figure 6.6 has been calculated by evaluating the ratio between the area covered by thrombus formed and the total blood flow area. To determine the area covered by the thrombus, or in other words the enveloped area surrounding the platelets that form thrombus, a built-in image processing tool that is available in MATLAB was used. The image processing tool converts the region which contains platelets that form thrombus into binary format and then evaluates the corresponding area which is defined by the enveloped region. The MATLAB tool was validated prior to use by estimating ratio between known (or user define thrombus) and the total area of an artificial image.

It can be seen from Figure 6.6 that the growth rate of the thrombus gradually increases with blood velocity until approximately 500 μm/s. Beyond 500 μm/s, the thrombus growth rate drops to a lower level. The results illustrated in Figure 6.6 qualitatively agree with the experimental observation made in (Begent and Born 1970). Given that the results reported here are from 2-dimensional simulations, direct comparisons could not be made at this point. It is evident, however, from the results that the blood flow rate plays a crucial role in the build-up and separation of a thrombus. The results also indicate that the growth rate of the thrombus, its thickness, and formation/separation vary according to the blood flow rate and these results are consistent with experimental observations reported in (Begent and Born 1970).

To further establish the accuracy of the model developed in this research, a comparative study was conducted with a 2-dimensional simulation model reported in the literature (Xu et al. 2008). In this study, the numbers of platelets (size of the clots) adhered/aggregated at different blood flow rates were compared. Figure 6.7 illustrates the comparative results obtained with SPH model developed in this article and computational model reported by (Xu et al. 2008). It is evident from Figure 6.7 that both simulation results compare well. Using equation (5.4) (Chapter 5), the average relative error in the numbers of platelets (size of the clots) through the different velocities in Figure 6.7 is 1.65%.

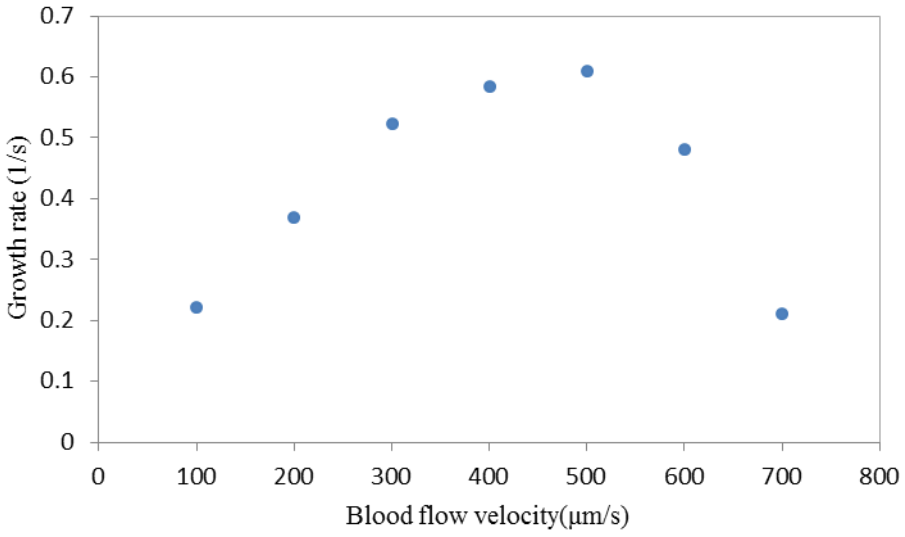

Figure 6.6 Effect of blood flow velocity with thrombus growth rate

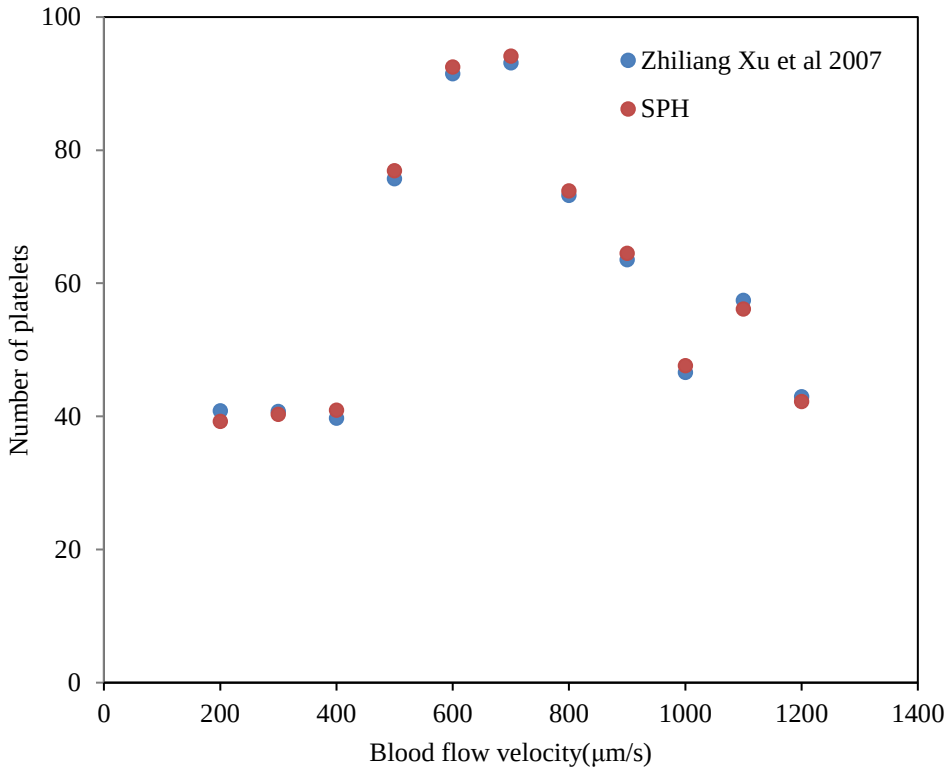

Figure 6.7 Effect of blood flow velocity on the number of platelets aggregated

6.2.2 Blood Flow Throw Vessels with Bend

Recent studies have suggested that fluid mechanical forces play an important role in the pathogenesis and pathophysiology of atherosclerosis(Berger and Jou 2000). The quantitative understanding of their contribution is considered to be poor, especially in the microvasculature with laminar flows. It was observed that atherosclerotic lesions might occur anywhere in the arteries but they preferentially form in arteries and arterioles in regions of high curvature, bifurcations, and junctions which experience major changes in flow structure and, thus, are subjected to large variations in fluid loading on the vessel wall. In addition, the phenomenon of atherosclerosis is known to particularly occur at different arterial sites of curvature, bifurcation, and branching (Texon 1960; Caro et al. 1971). The reason behind this

situation is the effect of pulling or suction on the arterial intima of the low-pressure region near the inner bend of highly curved arteries due to blood flow (Texon 1960). Many previous studies have shown that the wall shear stress (high or low) has played an important role to find the atherosclerotic (Fry 1968, 1969; Caro et al. 1971). Many researchers have tried to determine between these two factors. For example, (Friedman et al. 1981; Ku et al. 1985) compared measurements *in vitro* of the human circulatory system with physiological and anatomical data and proved that intimal plaque thickening was very high in regions of low, and not high, wall shear stress. Meanwhile, (Lutz et al. 1977) studied the velocity profiles and wall shear stresses for steady flow in asymmetric bifurcations. Normally, the locations of curvature in the human circulatory system that refer to a frequent incidence of atherosclerosis formation of thrombosis are the aortic arch and the cerebral and coronary arteries (Chandran et al. 1979). Some researchers have extended these studies to investigate different curvature of arteries in the human body, such as carotid siphon, distal femoral artery, branching of the femoral artery (Back et al. 1985; Perktold et al. 1988; Wensing et al. 1995; Giordana et al. 2005). In addition, (Nandalur et al. 2006) evaluated the calcified atherosclerotic burden in the cervical carotid, which is one of the curved arteries, using an MDCT (multidetector CT scanner) to specify the relationship of scores with luminal stenosis and ischemic symptoms. (Zheng et al. 2015) studied the human umbilical vein to show the influence of vessel curvature in thrombus formation. Furthermore, (Sanyal and Han 2015) investigated the effect of tortuous arteries with hypertension and atherosclerosis that is represented in part of the coronary artery. The motivation behind this simulation is to model thrombus formation and to investigate the effect of vessel geometry on thrombus formation and its growth. For this purpose, vessels with 90^o and 180^o bends were chosen for use

in the numerical simulations. Figure 6.8 illustrates the initial geometry of the two cases and Figure 6.9 shows the two-dimensional vessel configurations with platelets and plasma in the fluid model. The boundary conditions and flow parameters used in the simulations were same as that of straight vessel. Approximately 5000 SPH particles were used to model the material in the numerical simulation of bent vessel (see Figure 6.9). The initial distance between the particles in both directions is 1.0 μm. The geometrical specifications of the bent vessels illustrated in Figure 6.8 are adopted from (Liu et al. 2008).

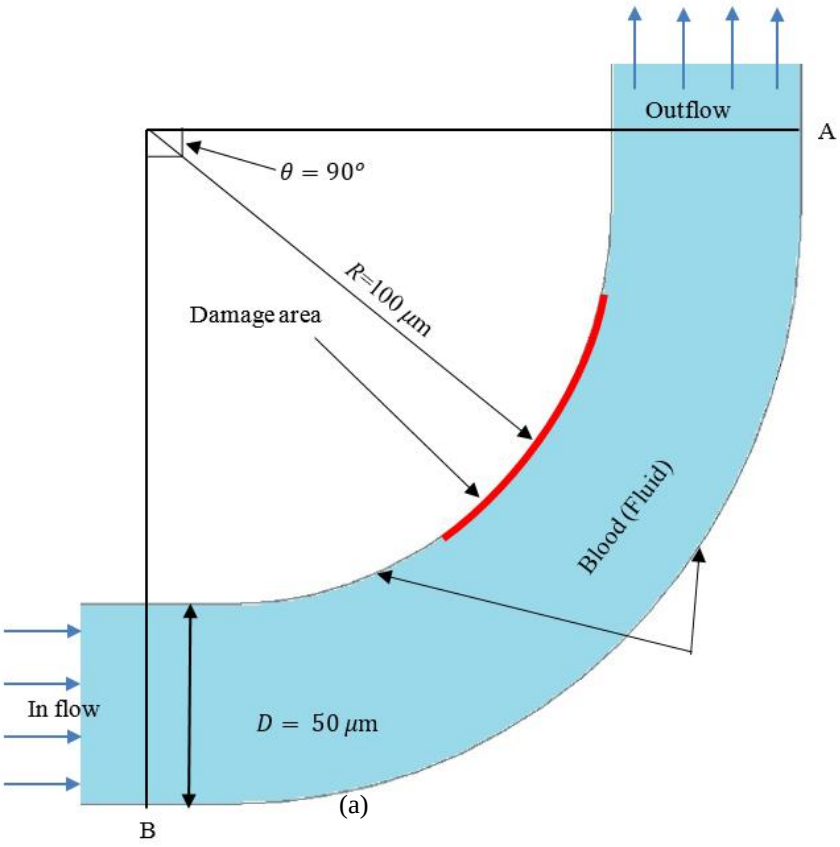

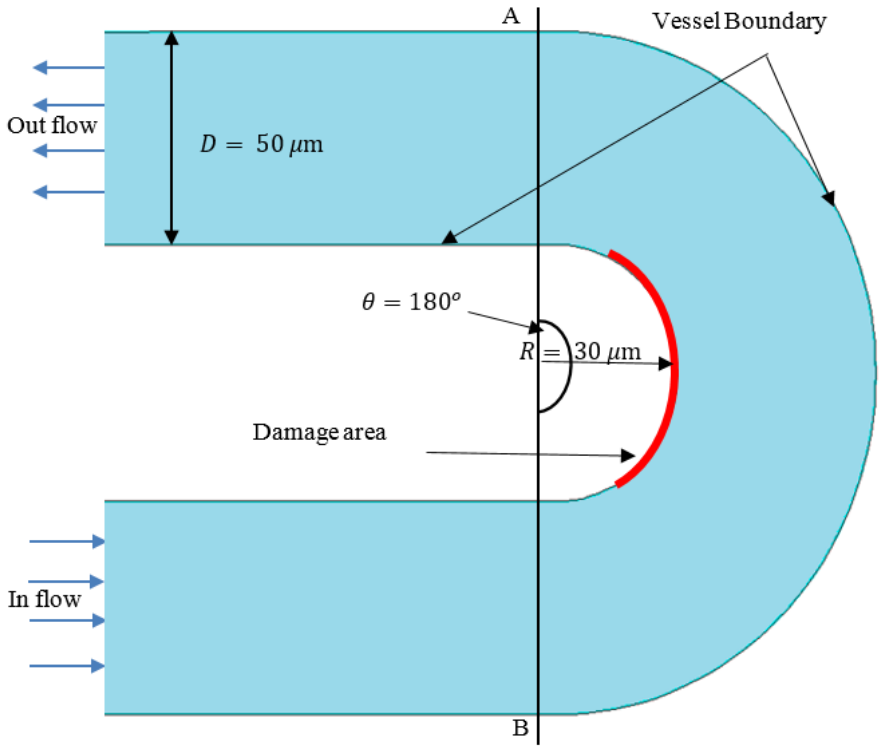

(b)

Figure 6.8 The geometry of the vessels with (a) 90 ° and (b) 180 ° bends

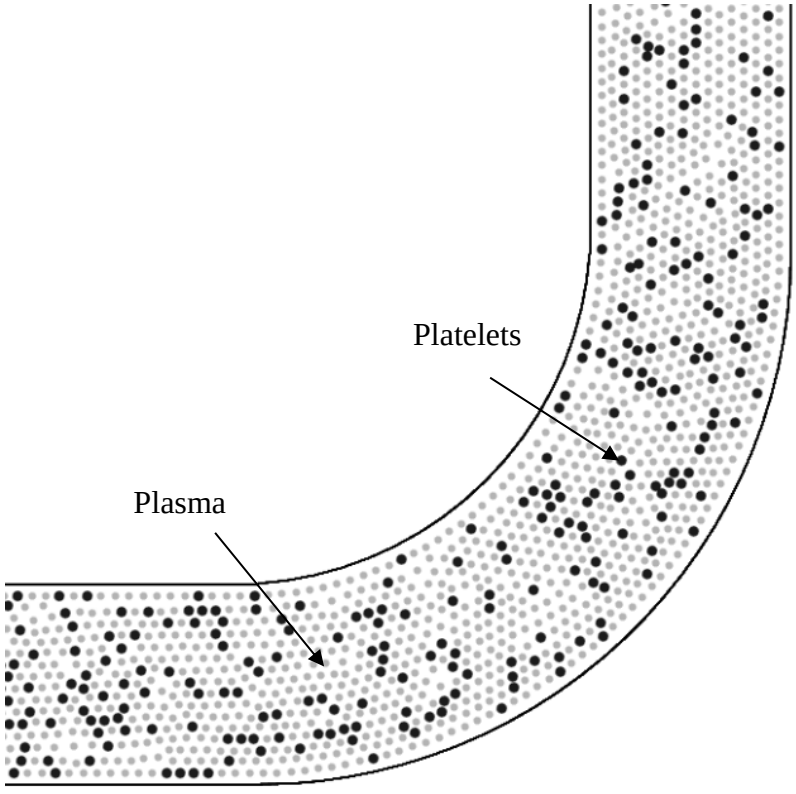

(a)

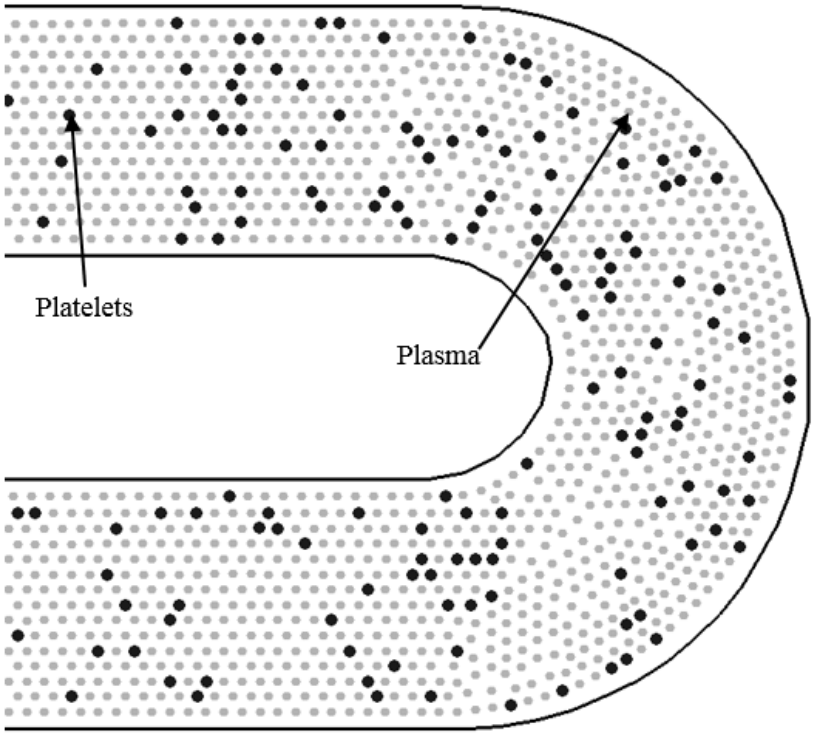

(b)

Figure 6.9 The distribution of platelets and plasma inside the bent vessel (a) 90^o and (b) 180^o

Figure 6.10 depicts the growth of a thrombus in a vessel that has a 90^o bend. The fluid velocity increases marginally towards the inner side of the bend where maximum velocity of the flow is reached. The larger velocity in the inner vessel wall would carry more blood cells and more reactants to the curve wall (Tangelder et al. 1985; Turitto and Hall 1998). Consequently, less platelets adhere and aggregate in the case of vessel with 90^o bend (at the same instants) when compared to a straight vessel with the same damage area and fluid entry velocity. Figure 6.10 also indicates that after the thrombus developed into a substantial volume, it was destroyed by the blood flow and transported to the downstream of the vessel. The numerical results clearly indicate that the difference in velocity along the bend sections can be attributed to the variations in the shape of thrombus formed and its collapse or separation time. The separation of thrombus is triggered when the blood flow velocity is sufficiently high to exert fluid forces on thrombus to overcome the

aggregation force. The results obtained are consistent with the results produced by (Liu et al. 2008).

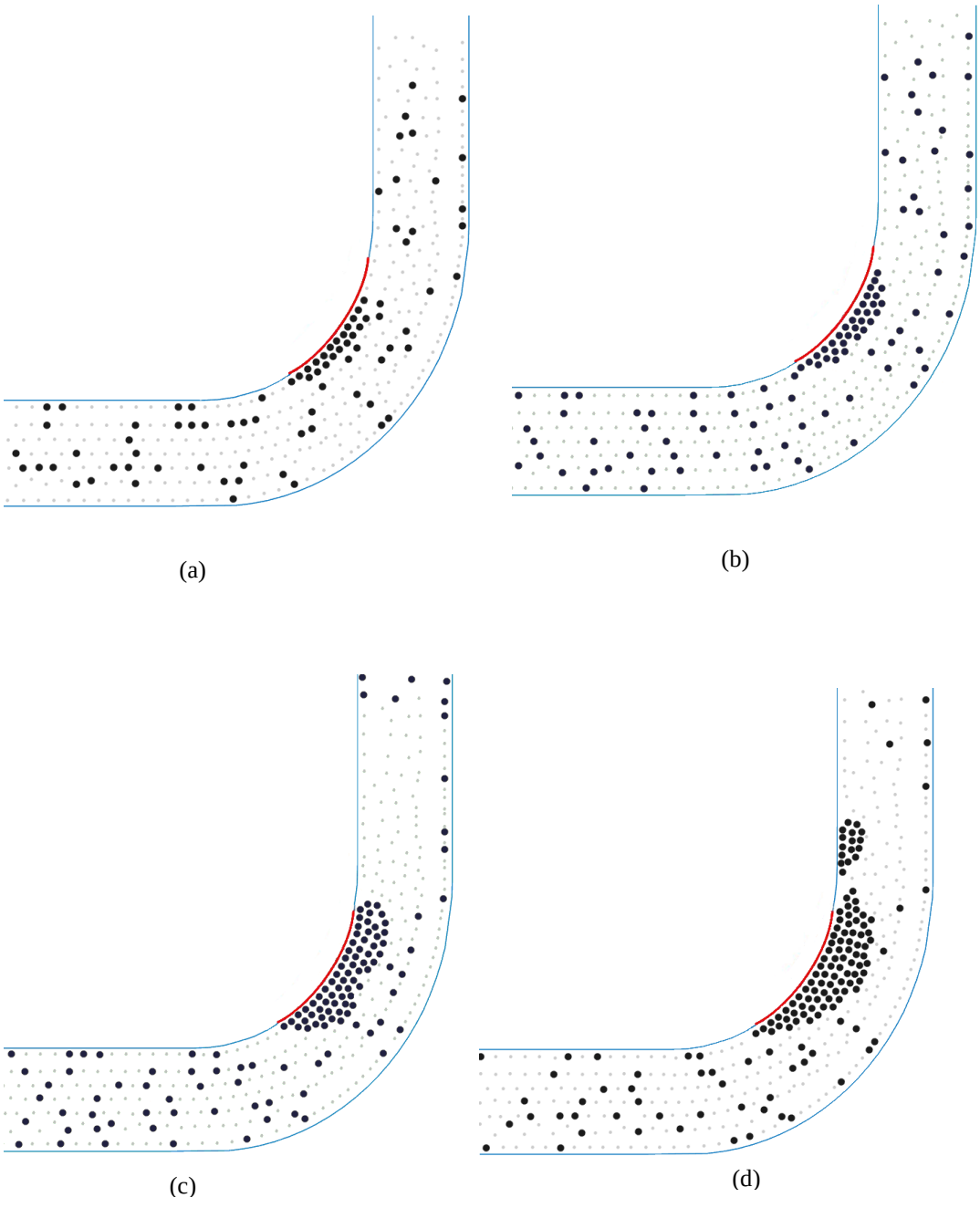

Figure 6.10 The platelet aggregation for entry velocity =100 µm/s at (a) *t*=0.2s (b) *t*=0.3s; (c) *t*=0.4s (d) *t*=0.6s.

Figure 6.11 describes the growth of a thrombus in a vessel that has 180^o bend. It can be noted that, the numbers of platelets that adhere and aggregate on the damaged area of the vessel for 180^o bend are different from those in the vessel with 90^o bend. Given that the maximum velocity is towards the inner side of the bend, the velocity for the 180^o bend will be larger than that in a vessel with a 90^o bend, the number of platelets that adhere and aggregate in the case of vessel with 180^o bend is less. As a result, in Figure 6.11(b), with fluid entry velocity 100 $\mu m/s$, the damaged area is covered with only a monolayer of platelets. As can be noted from Figure 6.12, with a higher fluid entry velocity 700 $\mu m/s$, the number of platelets adhere and aggregate are much fewer compared to that in the case of entry velocity 100 $\mu m/s$ and the characteristics of thrombus growth/transportation were entirely different to that of a straight vessel and a vessel with 90^o bend. From these computational results, it is apparent that the growth and separation of thrombus are significantly influenced by the curvature of the vessel and blood flow rate.

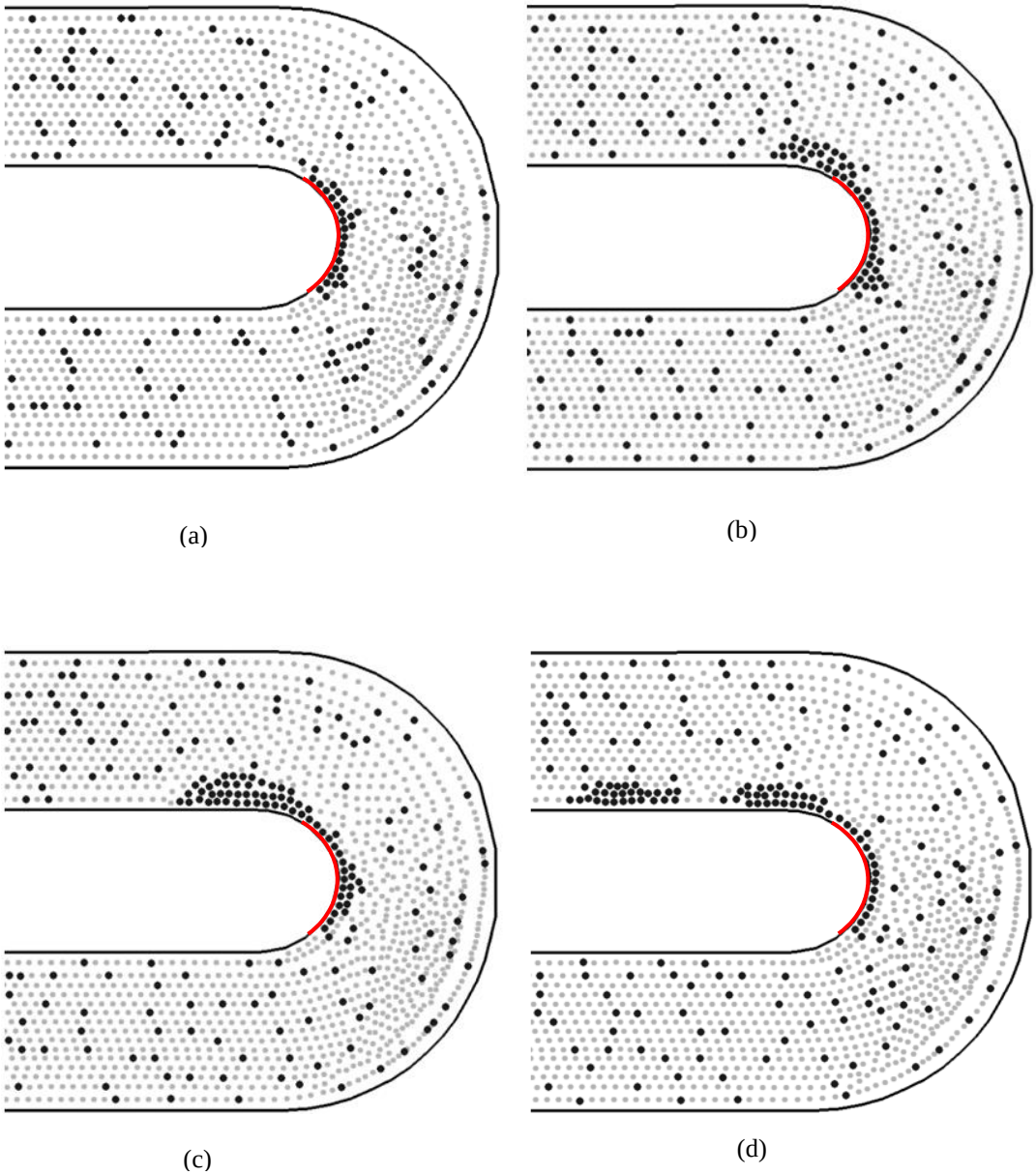

Figure 6.11 The platelet aggregation for entry velocity =100 μm/s at (a) *t*=0.2s (b) *t*=0.3s (c) *t*=0.4s (d) *t*=0.6s.

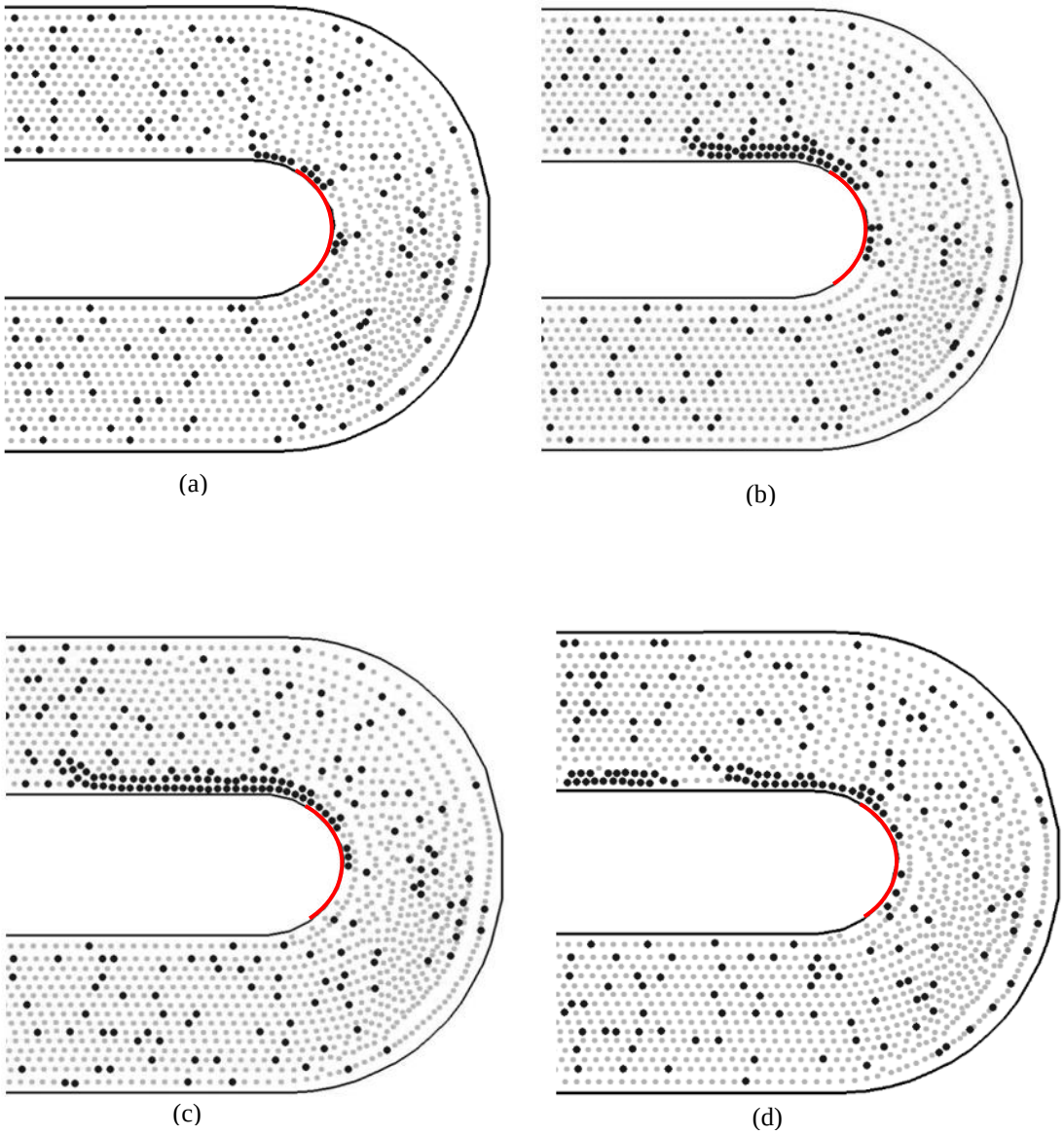

Figure 6.12 The platelet aggregation for entry velocity =700 μm/s at (a) *t*=0.2s (b) *t*=0.3s (c) *t*=0.4s (d) *t*=0.6s

6.2.3 Blood Flow Through Stenosis Vessel

The cardiovascular disease usually leads to natural death in most of the world; it is estimated that 50% of sudden deaths are due to cardiac causes. The high percentage of these sudden deaths are due to the acute ventrical tachyarrhythmias that are often caused by acute coronary events (Huikuri et al. 2001). According to the clinical diagnosis, these diseases can happen in people without previous symptoms. In many

cases, sudden death happens in patients with high coronary risk rather than patients with previous myocardial infarction (Myerburg et al. 1998). In coronary artery disease, the blood vessel is progressively narrowed by the enlargement of a plaque, called an atheroma, in the intimal layer. The atheroma consists of smooth muscle cells, lipids, collagen, elastin, and sometimes calcium deposits. The constriction caused by the atheroma is clinically referred to as a stenosis (Ku 1997). In most situations, sudden death is caused by a mural thrombus which occludes the lumen and restricts blood flow in vessels. Clinically, a thrombosis is considered to be a thrombus formation on the ruptured atherosclerotic plaque, which is also called atherothrombosis (Viles-Gonzalez et al. 2004). This expression refers to the combination of both the acute and chronic events in arterial disease (Ruggeri 2002). The acute thrombosis can lead to unstable angina or myocardial infarction due to the embolization of thrombus or the thrombus formation (Flannery 2005). Thrombus formation in different arteries or stenotic arteries is mostly referred to participate of the platelet. To analyse thrombus formation in a straight vessel with an internal and local geometric variation, the blood flow through a stenosis vessel is examined in this section. The aim in this simulation is to determine the modelling parameters that will reproduce qualitatively comparable results with respect to experimental observations reported in the literature.

Figure 6.13(a) illustrates the initial geometry of the stenosis vessel, which is based on the geometrical description provided in (Kamada et al. 2011). The total length of the vessel is 300μm, and the stenosis area is in the middle of the vessel with the length of the damaged area is 30μm. The diameter of the vessel is 20μm. As per the geometry, the vessel contains 75% stenosis by cross-sectional area. The initial distance between particles is 1.0μm ($= \Delta x = \Delta y$). The density ρ and kinematic viscosity v of the

plasma and platelets were set as $\rho = 1\text{x}10^{3}\text{kg/m}^{3}$ and $v = 1\text{x}10^{-6}\text{m}^{2}s^{-1}$. The amount of the platelet particles used in this simulation is approximately 7 % of the plasma. The entry velocity of the blood flow is 500µm/s. The numerical simulations with various parametric values for the spring constants (K_{ad} , K_{ag}), the adhesion area (d_{ad}) and the aggregation area (d_{ag}) were repeated until a qualitative match is obtained between the numerical simulations and experimental results reported in literature. From the numerical experiments, the parametric values obtained for spring constants K_{ad} and K_{ag} were $9.0\text{x}10^{9}$ N/m and $5.0\text{x}10^{9}$ N/m, respectively. Furthermore, the suitable parametric values for adhesion area (d_{ad}) and aggregation area (d_{ag}) were found to be 2.0 µm and 4.0 µm, respectively. It can be noted from these resulted parametric values that the aggregation area d_{ag} is doubled in this simulation compared to previous numerical examples to reproduce thrombus location and growth similar to that of experimental results (Flannery 2005). In addition, the spring constant for aggregation K_{ag} is also slightly modified to adjust the shape of the thrombus to match the observation reported in the experiment. The total number of particles used in the simulation to model the platelets and plasma was 8400.

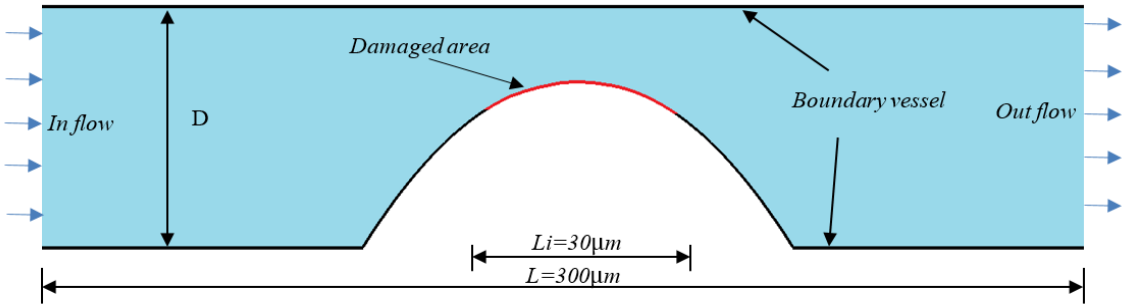

(a)

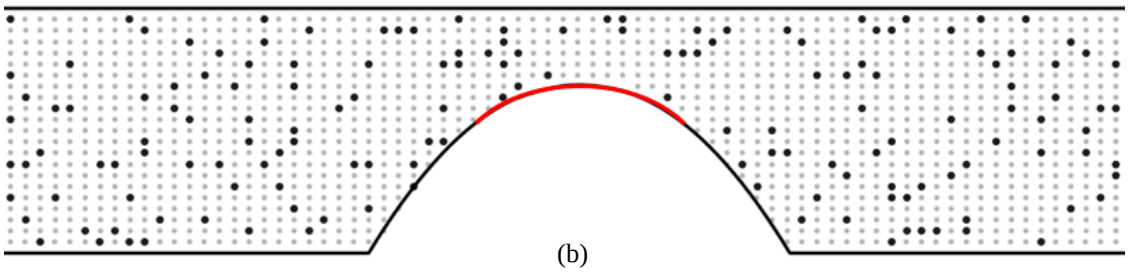

(b)

Figure 6.13 (a) Geometry of the two-dimensional simulation of a stenosis vessel (b) The distribution of the platelets and plasma particles

Figure 6.14 illustrates the growth of a thrombus at various stages (i.e. at 240s, 320s, 400s and 480s) during the numerical simulation of the blood flow through the stenosis vessel. To clearly demonstrate the effect of aggregation spring constant K_{ag}, simulations with K_{ag}= 4.5x10^9 N/m (previously used value) and K_{ag}= 5.0x10^9 N/m are presented in Figure 6.14. From the following figures, various stages of thrombus growth on the damaged area of the wall are clearly apparent. It can be seen from these figures that the growth of thrombus starts slowly from the upstream side of the damaged area and continues to grow along the downstream of the damaged area where the thrombus grows rapidly and develop into a large volume. It can be noted from Figure 6.14 that larger amount of thrombus formation occurs at the vicinity of the throat of stenosis. The results of the numerical simulations also indicate that the thrombus formation nearly result in complete occlusion of the vessel. As thrombus grows, the flow characteristics changes due to the protruding surface of thrombus. As a result, adhesion and aggregation of platelets will be influenced accordingly. Figure 6.14(d) demonstrates that for the modelling parameters chosen in the simulation, the occlusion of the vessel is most likely to occur at the vicinity of downstream of stenosis apex. It is also worth noting that there was no separation of the thrombus during the various stages depicted in Figure 6.14.

This is due to fact that the aggregation area was increased in this simulation to obtain thrombus formation characteristics similar to that of experimental findings. The aggregation area is the only parameter subjected to a significant change in this test compare to simulations reported in the previous sections. The increase in aggregation area can be attributed to the fact that the presence of stenosis can affect hemodynamic of blood flow over the stenosis apex, which in turn can increase platelet activation as suggested in (Karino and Goldsmith 1979; Lelah et al. 1984). During the numerical simulation of a stenosis vessel, it was also observed that the thrombus tends to develop faster than in the case of straight the vessel without stenosis. This is due to both increase in aggregation area and reduction in flow cross-sectional area. As the flow area is reduced due to the stenosis, more platelets will travel in the vicinity of the damaged area. Consequently, there is a rapid growth of thrombus in the case of stenosis vessel. The profile of thrombus obtained at various stages of the growth compare well with experimental results in literature (Flannery 2005). In addition, the number of platelets deposited over the time as demonstrated by Figure 6.15 has a similar trend to that of experimental observation noted in (Flannery 2005). The numerical results obtained in the above simulation are promising and can be used when predicting valuable information, such as location/growth of thrombus and occlusion time.

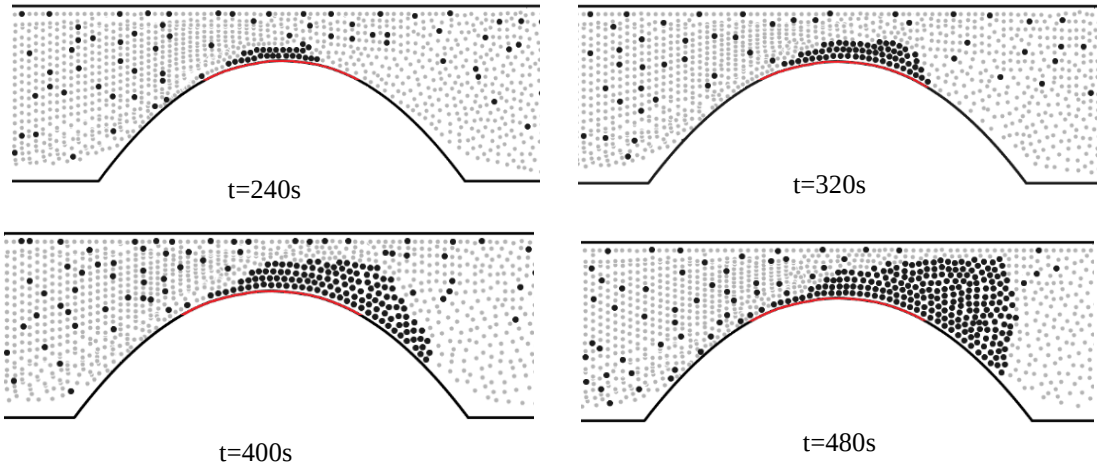

(a)

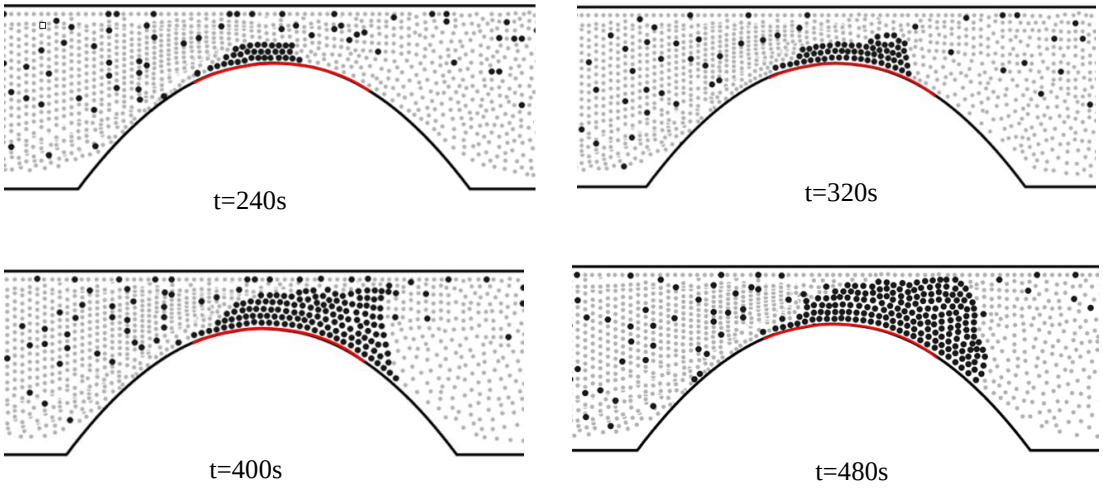

(b)

Figure 6.14 The platelet aggregation for stiffness (a) $K_{ag} = 4.5\text{x}10^{9}\ \text{N/m}$

(b) $K_{ag} = 5.0\text{x}10^{9}\ \text{N/m}$

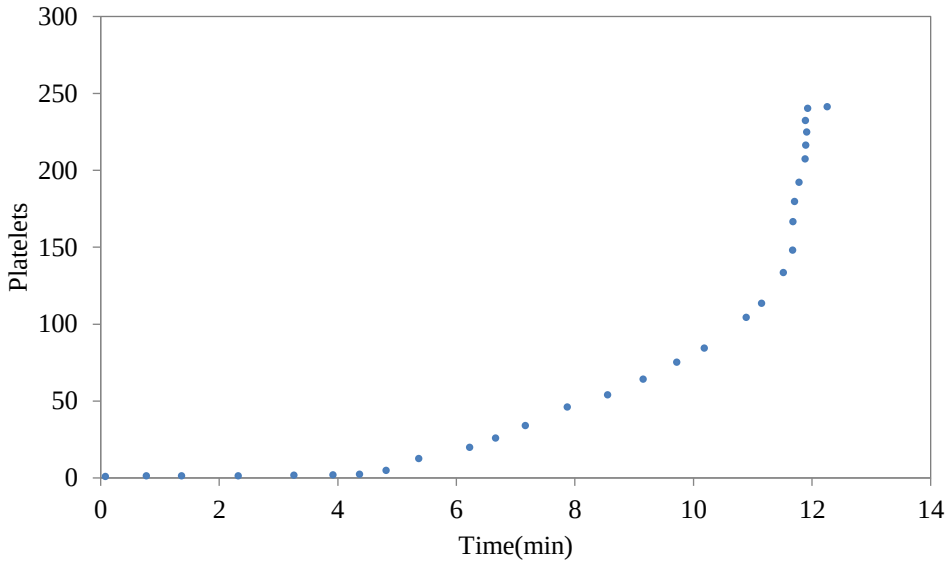

Figure 6. 15 Number of platelets attached and/or aggregated with time

6.3 Three-Dimensional Simulation of a Thrombus

Predicting thrombus behaviour is very difficult, especially in the presence of various physiological and pathological conditions, and also with complex vessel shapes. However, an understanding of the plasma and platelet behaviour and the blood flow characteristics is crucial to describe the formation of a thrombus with a high degree of accuracy. Numerical simulation is considered to be the most cost-effective way to gain a full understanding of the behaviour of blood flow, as well as to characterise thrombus formation inside various vessel shapes and to reveal the distribution of larger aggregate particles. This section will extend the application of methodologies proposed in the previous chapter to the three-dimensional simulation of thrombus in vessels with a straight rectangular and a tubular vessel. To observe the three-dimensional effect clearly. The three-dimensional effect is considered to be a key that can give an actual impression of thrombus formation during blood flow and, therefore, has the ability to predict the orientation of the thrombus. To investigate the

effect of different geometry of a blood vessel in thrombogenesis, the main aim of this section is to demonstrate that the numerical techniques can be extended to three-dimensional vessels and to assess the accuracy of the SPH method under such conditions (i.e. velocity of blood flow, geometry, platelets interaction and the spring constant). It is important to emphasise that the governing equations formulated and the numerical procedure developed in the previous chapters are equally valid for simulating thrombus formation inside three-dimensional vessels. The main difference here is that the developed methodology is applied to three-dimensional vessel geometries to perform more realistic simulations.

6.3.1 Three-Dimensional Modelling of a Straight Rectangular Vessel

In this example, the blood flow simulations are introduced inside a rectangular straight blood vessel with a constant velocity of blood flow of 100 $\mu m/s$, which is defined at the entrance of the straight vessel. The total length of the vessel L and the width between two opposite walls and height are $130\mu m$, W=$50\mu m$ and H=$50\mu m$, respectively (see Figure 6.16). In Figure 6.16 (a), the dimensions of the damaged area Lx x Wy are 8.0x8.0 μm^2 and the distance from the inlet to the damaged wall L_o is $40\mu m$. The total number of particles used in the simulation is 32500. The resolution of particles in x, y and z directions is set as 130x50x50 μm^3. The initial distance between particles in all three directions is 1.0 μm. The density ρ and kinematic viscosity v of the plasma and platelets are set as $\rho = 1x10^3 kg/m^3$ and $v = 1x10^{-6} m^2 s^{-1}$, respectively. The amount of the platelet particles used is approximately 8.8% of the plasma. The percentage of platelets is chosen larger than the normal physiological conditions to accelerate the formation of thrombus during the numerical simulation. In addition, the platelets are randomly distributed within

the fluid domain. In the numerical simulations, the parameters of spring constants K_{ad} and the K_{ag} are $9.0\text{x}10^9$ N/m and $4.5\text{x}10^9$ N/m, respectively, while d_{ad}= 3μm = d_{ag}, and r_o = 2 μm. Figures 6.16(a) and (b) show the configuration of the three-dimensional vessel model and the randomly distributed platelets. The boundary conditions used here are; a uniform velocity at the inlet and non-slip at the vessel wall.

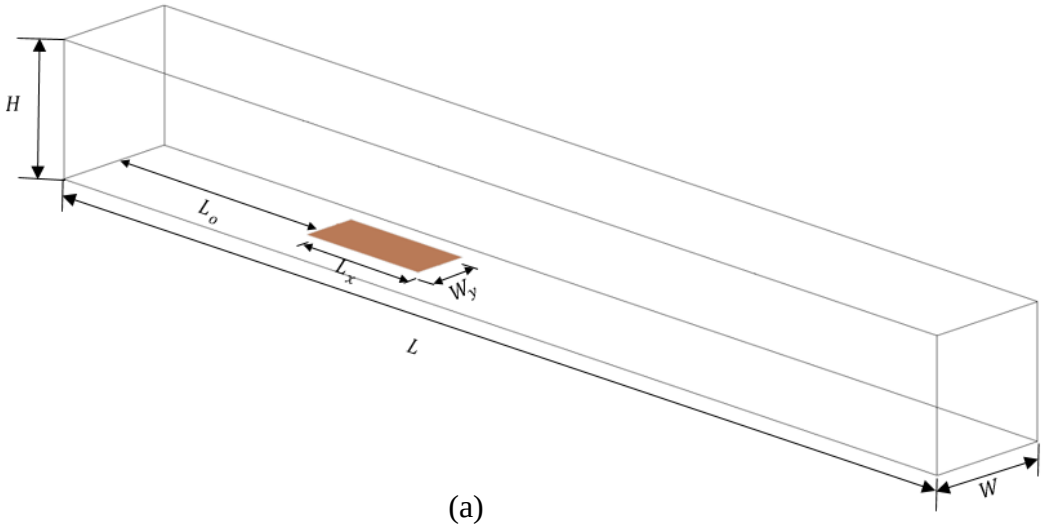

(a)

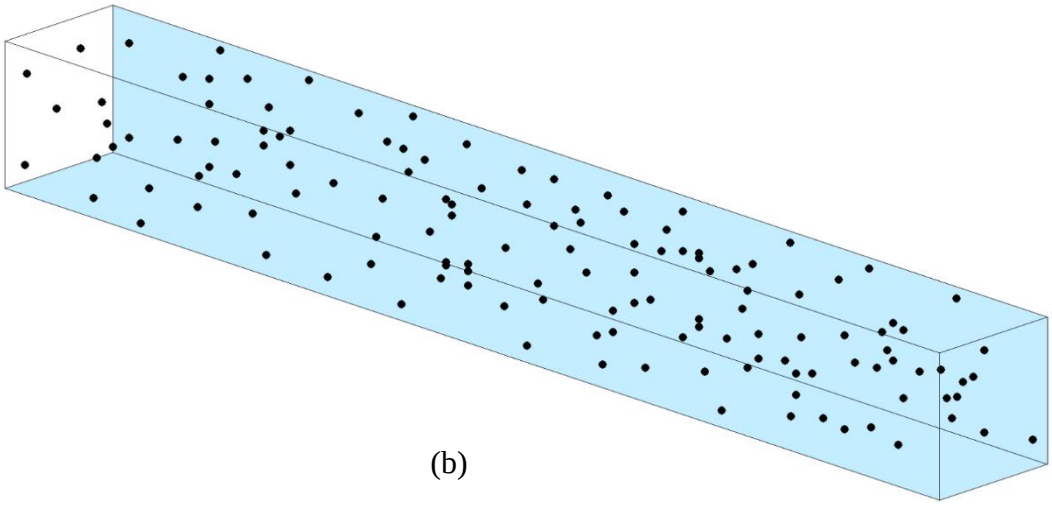

(b)

Figure 6. 16 (a) configuration of three-dimensional rectangular vessel (b) arrangement of platelet particles

Figures 6.17 illustrates the formation of thrombus at four different stages of the flow. In this figure, for clarity, only platelet particles are shown. The activated and adhered platelet particles in the figure are denoted by dark spheres, and the rest of the platelets are denoted by light spheres. The Figure 6.17 clearly illustrate the gradual formation of thrombus and the separation of a part of thrombus (see Figure 6.17 (d)) over the course of time. It is evident from Figure 6.17 that three-dimensional simulation provides more details of the geometrical nature of formed thrombus. The results displayed in Figure 6.17 (a, b, c and d) further proves that the nature of flow significantly influences the shape, formation and separation of thrombus. Further, it can be noted that the instances at which formation and separation of thrombus takes place is also affected by flow dynamics.

The Figure 6.17 depicts the number of platelets forming the volume of thrombus at various stages of the simulation. From Figure 6.17, it can be noted that the number of platelet particles forming thrombus increases slowly at the initial stages (<0.1s) and then rapidly increases at later stages. Figure 6.18 also compares the results obtained using SPH method to the results reported by (Kamada et al. 2010). The results are in good agreement with those presented by (Kamada et al. 2010). The results presented in Figure 6.18 also confirm that the average relative difference in particle number with respect to time is 0.69% (based on equation (5.4) in Chapter 5).

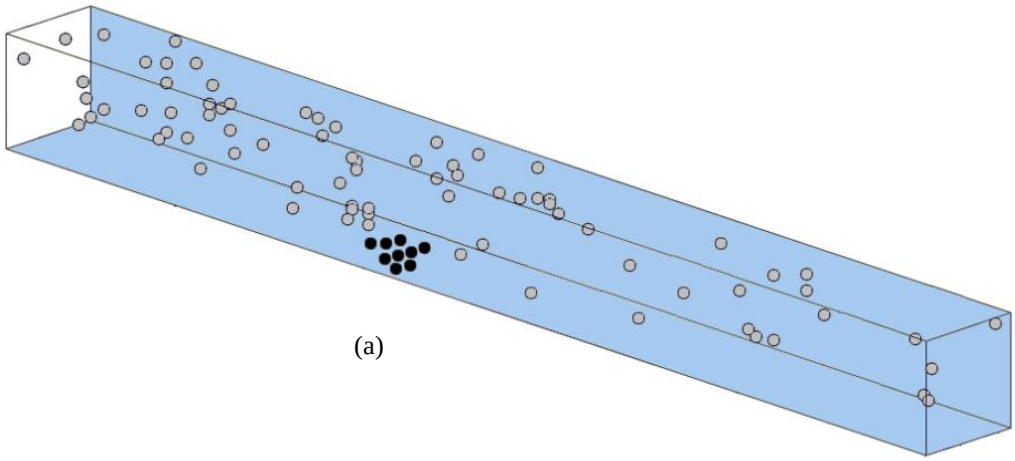

(a)

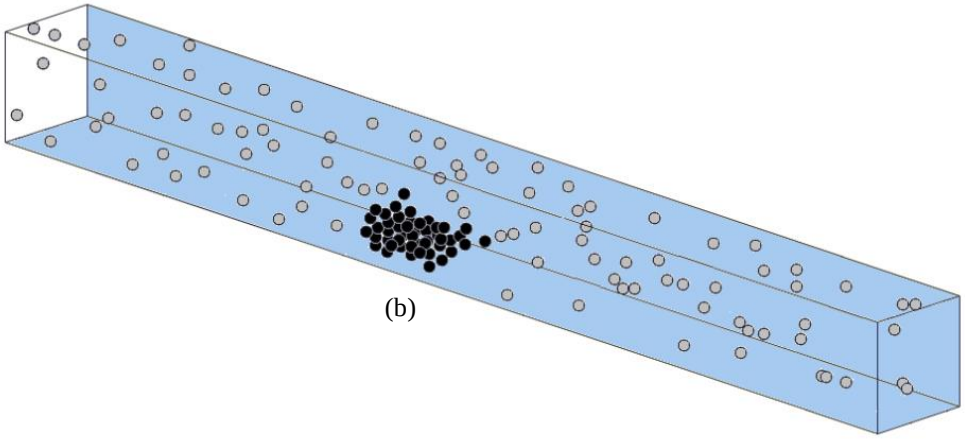

(b)

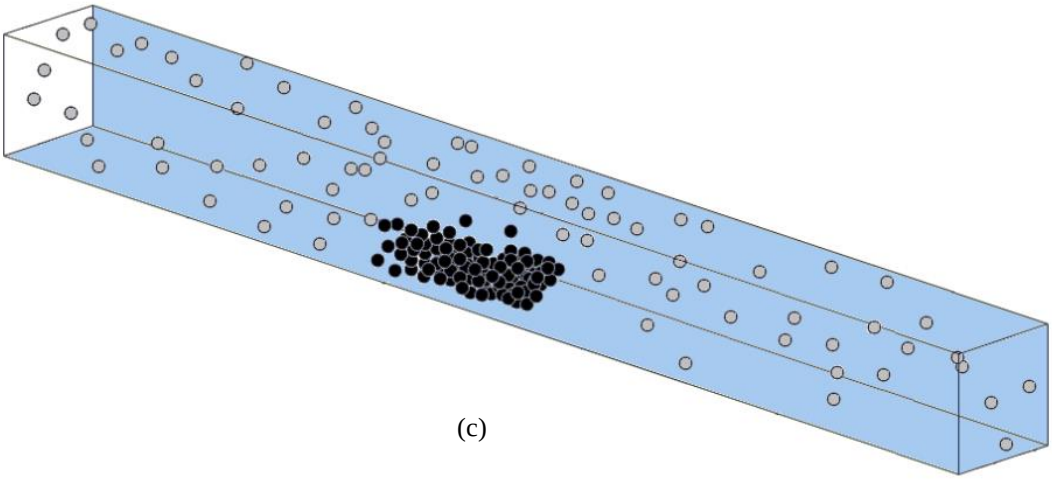

(c)

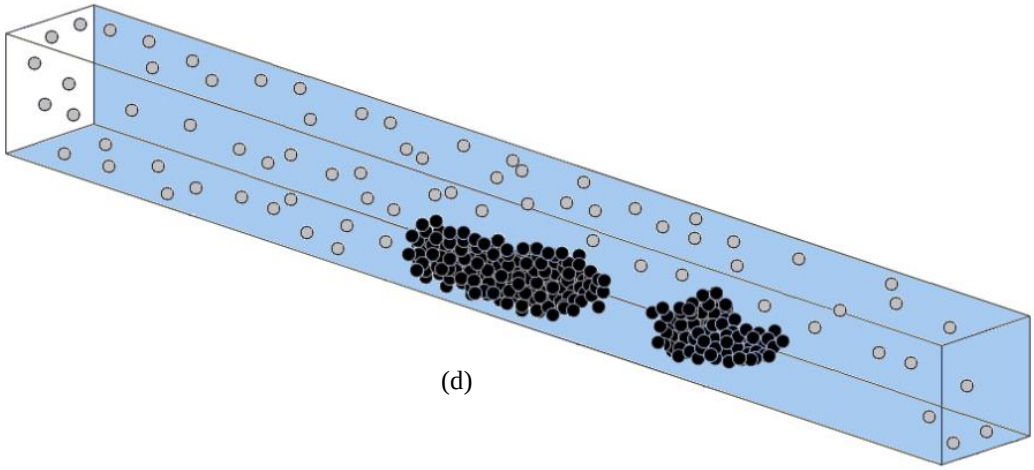

(d)

Figure 6.17 The platelet aggregation for entry velocity =100 µm/s and at (a) *t*=0.2s (b) *t*=0.3s (c) *t*=0.4s (d) *t*=0.6s

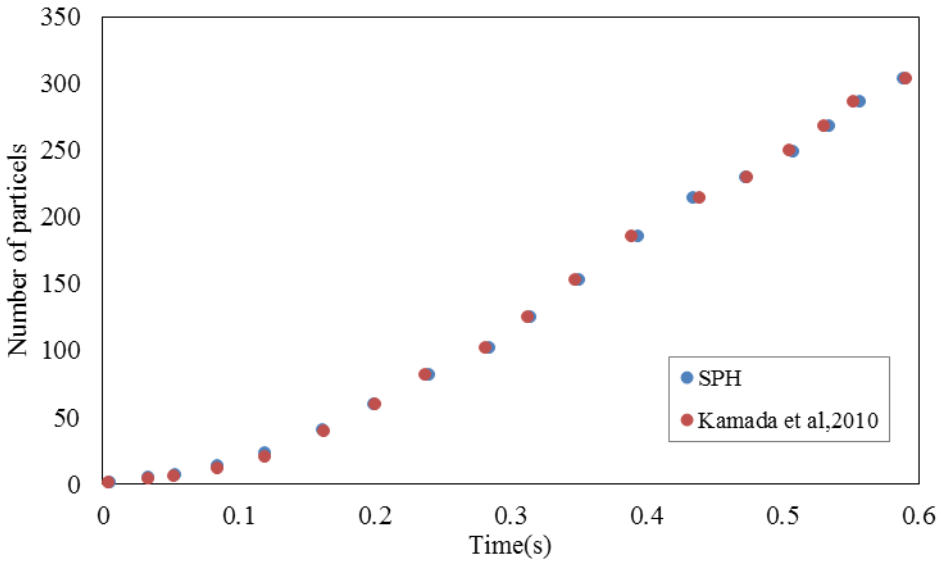

Figure 6.18 Effect of time on the number of platelets

6.3.2 Three-Dimensional Modelling of a Straight Tubular Vessel

In this section, three-dimensional blood flow is performed inside a 50µm diameter straight tube, with 500 µm length. Three different cases with steady blood flow rates of 100, 500 and 700 $\mu m/s$ were investigated. As shown in Figure 6.19(a) the dimensions of the damaged area (Lx x Wy) and the distance from the inlet to the damaged wall (L_o) are chosen as $(8.0 \times 8.0)\mu m^2$ and 40µm, respectively. The total

number of particles used in the simulation is about 50,000. The particles are uniformly distributed with initial distance between particles in all three directions is 1.0 μm. The density ρ and kinematic viscosity v of the plasma and platelets are set as $\rho = 1\text{x}10^{3}\text{kg/m}^{3}$ and $v = 1\text{x}10^{-6}\text{m}^{2}s^{-1}$. The amount of the platelet particles used were approximately 0.336% of the plasma (which is in line with normal physiological conditions). The platelet particles are randomly distributed as in Figure 6.19(b). The boundary conditions used here are similar to the conditions used in the rectangular vessel. In the numerical simulations, the parameters of the spring constants K_{ad} and K_{ag} were $9.\text{x}10^{9}\,\text{N/m}$ and $5.0\text{x}10^{9}\,\text{N/m}$, respectively, while d_{ad}= 3μm, d_{ag} = 4.0 μm and r_o = 2 μm. In this numerical test, a larger (twice as in the case of rectangular vessel) radius of influence is used for aggregation. This value of d_{ag} is chosen in order to compare the simulation results against the experimental results (Begent and Born 1970) in which no collapse of thrombus was observed.

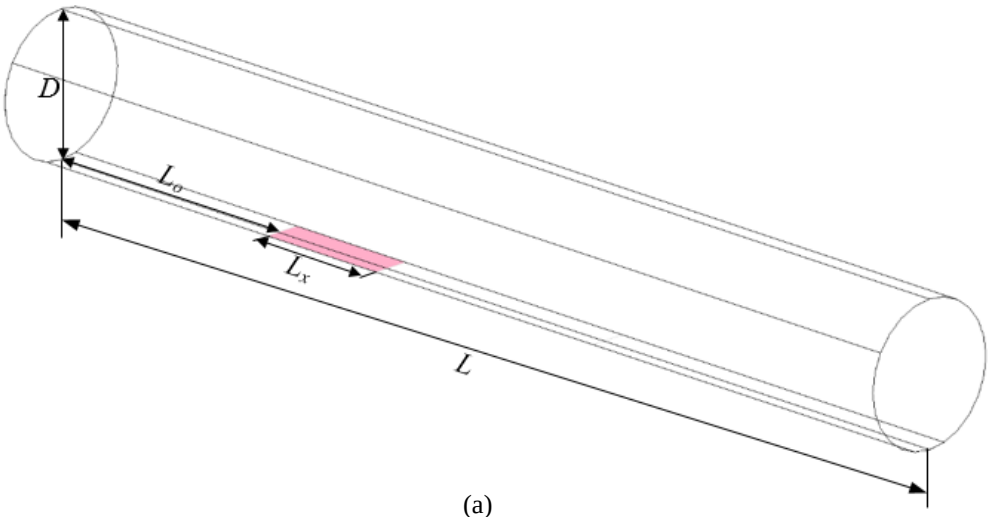

(a)

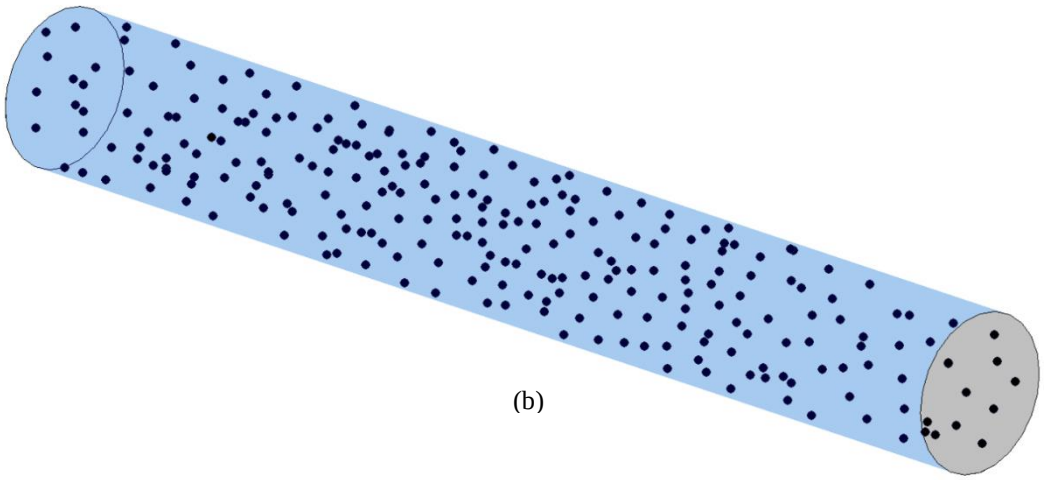

(b)

Figure 6.19 (a) Configuration of three-dimensional tubular vessel (b) initial arrangement of platelet particles

Figures 6.20, 6.21 and 6.22 illustrate the growth of thrombus at different times for flow velocities 100, 500 and 700 $\mu m/s$, respectively. As in the case of a rectangular tube, only platelets particles are shown in the figures. Figures 6.20, 6.21 and 6.22 illustrate the growth of thrombus over time, and they show how the shapes and dimensions of the thrombi are influenced by various flow velocities. Due to the use of larger aggregation zone, the thrombus formed in this example does not collapse and separate, as observed in the case of rectangular vessels.

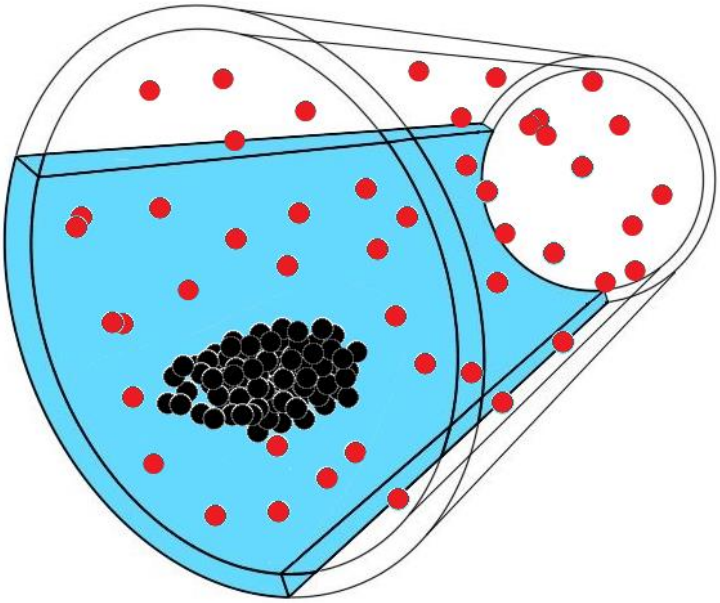

(a)

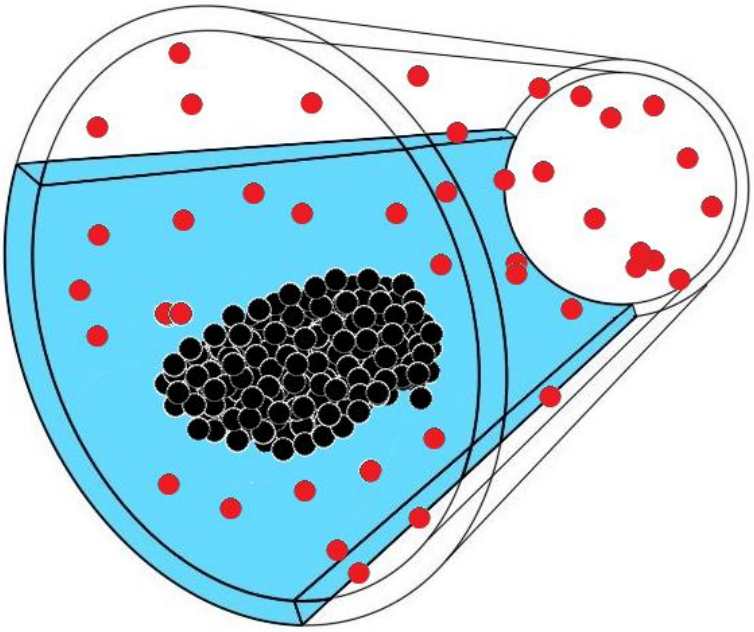

(b)

Figure 6. 20 The platelet aggregation for entry velocity =100 µm/s and at (a) *t*=2s (b) *t*=10s

A comparison between these three cases shows that the growth size of the thrombus decreases with higher flow velocities. The profile of the thrombus obtained at various stages of growth compares very well with the experimental results in the literature (Begent and Born 1970). In addition, the number of platelets deposited

(adhered/aggregated) at different blood flow rates over time, as illustrated in Figure 6.23, is qualitatively similar to that of the experimental observation noted by (Begent and Born 1970). These results show that dynamic changes in velocity of blood flow affect the volume and characteristics of the primary thrombogenesis. Further, the results presented in Figure 6.23 also confirms (using equation (5.4) in Chapter 5) that the average relative difference in the growth rate constant with respect to velocity is 5.49%.

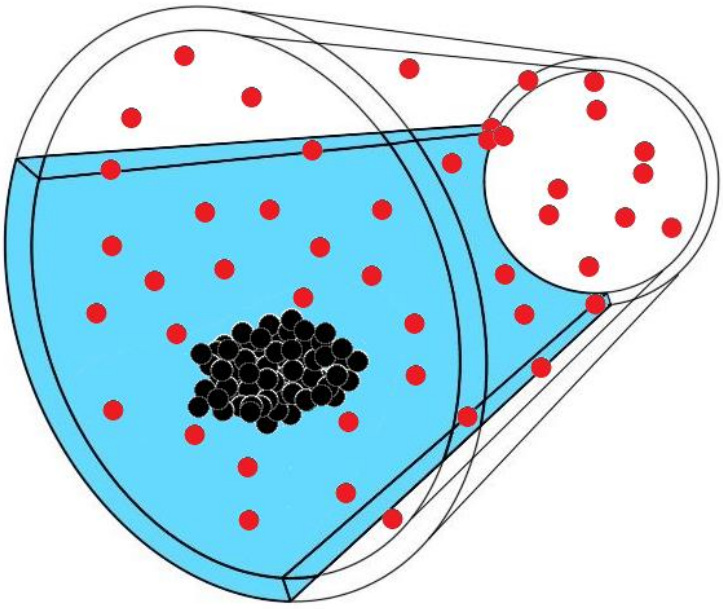

(a)

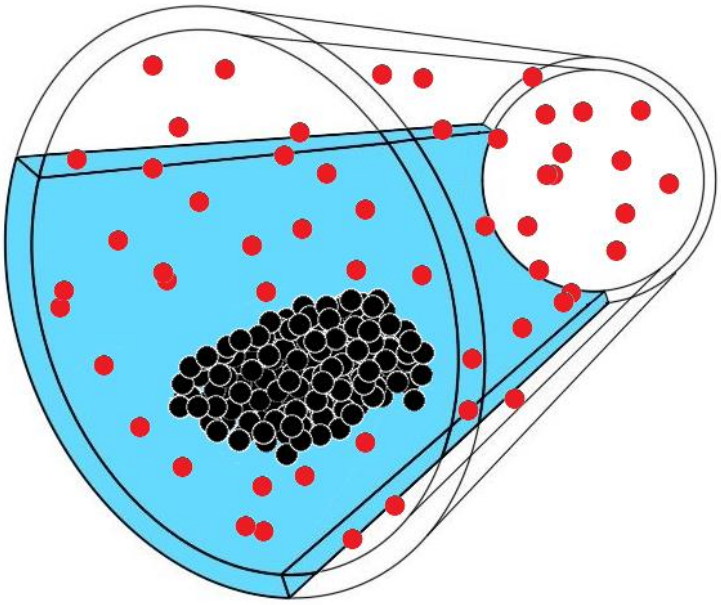

(b)

Figure 6.21 The platelet aggregation for entry velocity =500 µm/s and at (a) *t*=2s (b) *t*=10s

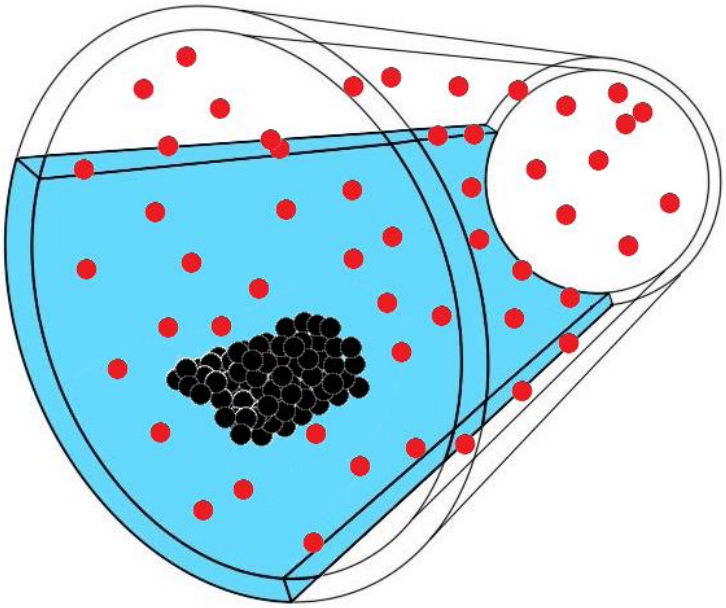

(a)

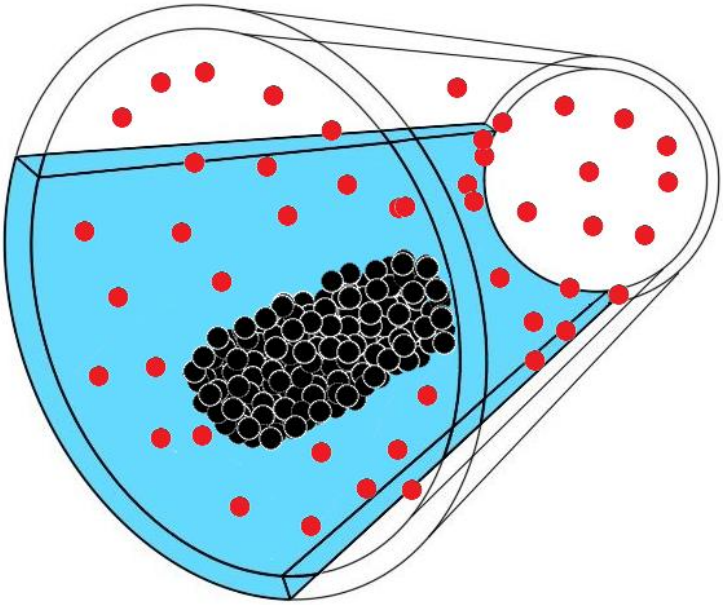

(b)

Figure 6.22 The platelet aggregation for entry velocity =700 µm/s and at (a) *t*=2s (b) *t*=10s

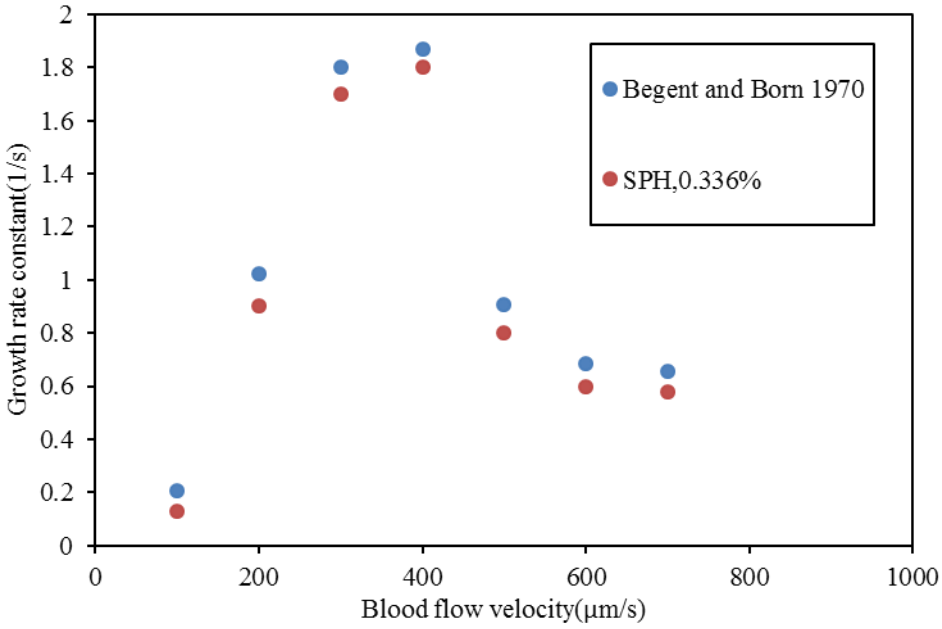

Figure 6. 23 Effect of Blood flow on the number of platelets

6.4 Conclusion

This chapter has focused on the simulation of the thrombogenesis process using the SPH method. The numerical method is developed to model platelets adhesion/aggregation on the surface of the damaged area of blood vessels and to investigate the influence of blood flow rates on thrombus growth. In the numerical simulations, blood flow inside a vessel is discretised by particles that are assumed to have the characteristics of blood constituents, such as plasma and platelets. The platelet adhesion and aggregation processes during the blood flow are modelled by adopting an inter-particle penalty force method. The model proved to be efficient in simulating adhesion and aggregation process without rigorous computational efforts. The potential of the SPH method to simulate the thrombogenesis process is demonstrated via a number of numerical examples. The numerical simulations were able to indicate how blood flow velocity influenced thrombus growth rate in a straight vessel and vessel with a bend. The numerical results also qualitatively agree with experimental observations reported in the literature. This study also demonstrated that the thrombus formation inside vessels of various geometrical shapes (two- and three-dimensional) could also be modelled using the developed numerical procedures. In addition, the Lagrangian nature of SPH enables one to track the history of fluid properties and to track particles (e.g. platelets) suspended in the fluid. This ability of SPH provides huge potential in the modelling of blood flow and thrombus formation in arteries or vessels. The modelling technique presented here can be further developed in to a more sophisticated patient-specific computational tool to predict formation and characteristics of thrombus and to understand the corresponding medical conditions.

Chapter 7

Conclusions and Perspectives

7.1 Conclusions

The major conclusions can be embodied from this work as follows:

- This work attempted to apply a corrected smooth particle hydrodynamics (SPH), a fully Lagrangian meshfree method, to study hemodynamics of blood flow. This method demonstrated significant consistency as a numerical methodology to accurately simulate hemodynamics in the arteries/vessels and was able to capture some interesting flow characteristics.
- The accuracy and convergence of the developed SPH method were evaluated via a number of numerical examples. These examples were chosen in order to explore the accuracy of the methodology in simulating various characteristics and physical conditions. The results of these simulations were compared with existing analytical and experimental results. The results compared well with established quantities and evaluated the accuracy of the developed method.
- SPH method proposed was applied successfully to simulate a pulsatile flow inside a bifurcation artery. The results of the numerical simulations revealed good accuracy and confirmed that the developed methodology could be considered as an effective substitute for traditional mesh-based methods to study hemodynamics inside arteries with complex geometries. The investigation of blood flow behaviour inside bifurcation artery is important from a clinical point of view and the developed method can be easily utilised in understanding blood flow behaviour inside patient specific arteries.
- A numerical methodology was successfully implemented to simulate thrombus inside arteries and vessels, under the influence of varying blood flow rates. An effective algorithm based on spring (or penalty) force method

was developed to simulate adhesion and aggregation of platelets to form a thrombus. The stiffness of the spring force was determined by calibrating it based on platelet aggregation rate reported in the literature. The aforementioned model proved efficient in simulating adhesion and aggregation process without rigorous computational efforts. The potential of the SPH method to simulate thrombogenesis process is demonstrated via a number of numerical examples. The numerical simulations revealed how blood flow velocity influenced the shape and growth rate of thrombus inside vessels with different geometries. The capabilities and accuracy of this methodology were verified by comparing the simulation results with the experimental results. The numerical results were in excellent agreement with experimental results and confirmed that the SPH methodology is effective in accurately predicting thrombus formation inside arteries and vessels.

- The robustness of the computational model used for thrombus formation was assessed in two and three-dimensional vessels with different geometries. The influence of aggregation area on the collapse or separation of thrombus was also observed in this numerical study. In addition, the nature of thrombus formation in stenosis vessel was also investigated. Clinically, the formation of thrombus occlusion occurs in stenotic or non- stenotic arteries leads to irregular heart impulse which is considered one of the most consequences of Sudden Cardiac Death (SCD). The numerical methodology developed in the present work may provide a useful tool to perform such investigations.

7.2 Perspectives

- The cost of computational time can be reduced either by using high-end serial computers or by using high-performance parallel computers. Since the particle methods such as SPH are very conducive for parallelisation, flow inside three-dimensional complex arteries or vessels can be simulated within a reasonable computational time by appropriately parallelising the code.
- In this work, the formation of thrombus was modelled based on adhesion and aggregation of platelets only. The procedure developed can also be extended to other cells (e.g. red blood cell) which participate in the formation of thrombus. In addition, the model developed here can be enhanced by including other factors (e.g. chemical reactions, flow shear rate) involved in thrombus formation.
- It is important to extend the developed model to handle non-Newtonian and turbulent nature of the blood flow. In addition, flow inside arteries with larger diameters (e.g. aorta, coronary arteries) can be modelled with the developed method and the results can be compared with realistic patient-specific data.
- To increase the understanding of mechanisms involved in thrombus formation, several physiologically relevant variations can be incorporated in the present model. For example, the effects of pulsatile flow on the formation of thrombus and the effects of platelet activation by blood flow rate could be explored.

References

World Health Organization (WHO).*SpringerReference*. Springer Nature.

Aarts, P. and Bolhuis, P. A. and Sakariassen, K. S. and Heethaar, R. M. and Sixma, J. J. 1983. Red blood cell size is important for adherence of blood platelets to artery subendothelium. *Blood* 62(1), pp. 214-217.

AL-Rubaye, M. and Kulasegaram, S. and Karihaloo, B. L. 2017. Simulation of self-compacting concrete in an L-box using smooth particle hydrodynamics. *Magazine of Concrete Research*, pp. 1-11.

Amini, Y. and Emdad, H. and Farid, M. 2011. A new model to solve fluid–hypo-elastic solid interaction using the smoothed particle hydrodynamics (SPH) method. *European Journal of Mechanics-B/Fluids* 30(2), pp. 184-194.

Anderson, J. D. 1995. *Computational fluid dynamics*. Springer.

Andrews, R. K. and López, J. and Berndt, M. C. 1997. Molecular mechanisms of platelet adhesion and activation. *The international journal of biochemistry & cell biology* 29(1), pp. 91-105.

Artoli, A. M. and Hoekstra, A. G. and Sloot, P. M. 2006. Mesoscopic simulations of systolic flow in the human abdominal aorta. *Journal of biomechanics* 39(5), pp. 873-884.

Avolio, A. 1980. Multi-branched model of the human arterial system. *Medical and Biological Engineering and Computing* 18(6), pp. 709-718.

Back, M. and Cho, Y. and Back, L. 1985. Fluid dynamic study in a femoral artery branch casting of man with upstream main lumen curvature for steady flow. *ASME JOURNAL OF BIOMECHANICAL ENGINEERING* 107, pp. 240-248.

Baldewsing, R. A. and Mastik, F. and Schaar, J. A. and Serruys, P. W. and van der Steen, A. F. 2006. Young's modulus reconstruction of vulnerable atherosclerotic plaque components using deformable curves. *Ultrasound in medicine & biology* 32(2), pp. 201-210.

Bark, D. L. and Ku, D. N. 2013. Platelet transport rates and binding kinetics at high shear over a thrombus. *Biophysical journal* 105(2), pp. 502-511.

Bark, D. L. and Para, A. N. and Ku, D. N. 2012. Correlation of thrombosis growth rate to pathological wall shear rate during platelet accumulation. *Biotechnology and bioengineering* 109(10), pp. 2642-2650.

Bark Jr, D. L. 2007. Mechanistic numerical study of trhombus growth.

Basa, M. and Quinlan, N. J. and Lastiwka, M. 2009. Robustness and accuracy of SPH formulations for viscous flow. *International Journal for Numerical Methods in Fluids* 60(10), pp. 1127-1148.

Batchelor, G. 1970. K. 1967 An Introduction to Fluid Dynamics. Cambridge University Press.

Bathe, M. and Kamm, R. 1999. A fluid-structure interaction finite element analysis of pulsatile blood flow through a compliant stenotic artery. *Journal of Biomechanical Engineering* 121(4), pp. 361-369.

Bayraktar, S. and Güdükbay, U. and Özgüç, B. 2009. GPU-based neighbor-search algorithm for particle simulations. *Journal of Graphics, GPU, and Game Tools* 14(1), pp. 31-42.

Becker, M. and Teschner, M. eds. 2007. *Weakly compressible SPH for free surface flows*. Proceedings of the 2007 ACM SIGGRAPH/Eurographics symposium on Computer animation. Eurographics Association.

Begent, N. and Born, G. 1970. Growth rate in vivo of platelet thrombi, produced by iontophoresis of ADP, as a function of mean blood flow velocity. *Nature* 227, pp. 926-930.

Berger, S. and Jou, L.-D. 2000. Flows in stenotic vessels. *Annual Review of Fluid Mechanics* 32(1), pp. 347-382.

Bernsdorf, J. and Wang, D. 2009. Non-Newtonian blood flow simulation in cerebral aneurysms. *Computers & Mathematics with Applications* 58(5), pp. 1024-1029.

Bharadvaj, B. and Mabon, R. and Giddens, D. 1982. Steady flow in a model of the human carotid bifurcation. Part II—laser-Doppler anemometer measurements. *Journal of biomechanics* 15(5), pp. 363-378.

Bonet, J. and Kulasegaram, S. 2000a. Correction and stabilization of smooth particle hydrodynamics methods with applications in metal forming simulations. *International journal for numerical methods in engineering* 47(6), pp. 1189-1214.

Bonet, J. and Kulasegaram, S. 2000b. Finite increment gradient stabilization of point integrated meshless methods for elliptic equations. *Communications in numerical methods in engineering* 16(7), pp. 475-483.

Bonet, J. and Lok, T.-S. 1999. Variational and momentum preservation aspects of smooth particle hydrodynamic formulations. *Computer Methods in applied mechanics and engineering* 180(1), pp. 97-115.

Bonet, J. and Peraire, J. 1991. An alternating digital tree (ADT) algorithm for 3D geometric searching and intersection problems. *International Journal for Numerical Methods in Engineering* 31(1), pp. 1-17.

Boryczko, K. and Dzwinel, W. and Yuen, D. A. 2003. Dynamical clustering of red blood cells in capillary vessels. *Journal of molecular modeling* 9(1), pp. 16-33.

Botnar, R. and Rappitsch, G. and Beat Scheidegger, M. and Liepsch, D. and Perktold, K. and Boesiger, P. 2000. Hemodynamics in the carotid artery bifurcation::

a comparison between numerical simulations and in vitro MRI measurements. *Journal of biomechanics* 33(2), pp. 137-144.

Bronzino, J. D. 1999. *Biomedical engineering handbook*. CRC press.

Broos, K. and Feys, H. B. and De Meyer, S. F. and Vanhoorelbeke, K. and Deckmyn, H. 2011. Platelets at work in primary hemostasis. *Blood reviews* 25(4), pp. 155-167.

Cadroy, Y. and Hanson, S. R. 1990. Effects of red blood cell concentration on hemostasis and thrombus formation in a primate model. *Blood* 75(11), pp. 2185-2193.

Carneiro, F. and Ribeiro, V. G. and Teixeira, J. and Teixeira, S. 2008. Numerical study of blood fluid rheology in the abdominal aorta. *Design & Nature IV: Comparing Design in Nature with Science and Engineering* 4, p. 169.

Caro, C. 1982. Arterial fluid mechanics and atherogenesis. *Clinical Hemorheology and Microcirculation* 2(1-2), pp. 131-136.

Caro, C. and Fitz-Gerald, J. and Schroter, R. 1971. Atheroma and arterial wall shear observation, correlation and proposal of a shear dependent mass transfer mechanism for atherogenesis. *Proceedings of the Royal Society of London B: Biological Sciences* 177(1046), pp. 109-133.

Caro, C. G. 2012. *The mechanics of the circulation*. Cambridge University Press.

Casa, L. D. and Ku, D. N. 2014. High shear thrombus formation under pulsatile and steady flow. *Cardiovascular Engineering and Technology* 5(2), pp. 154-163.

Chandran, K. and Yearwood, T. and Wieting, D. 1979. An experimental study of pulsatile flow in a curved tube. *Journal of biomechanics* 12(10), pp. 793-805.

Chen, J. and Beraun, J. and Jih, C. 1999. An improvement for tensile instability in smoothed particle hydrodynamics. *Computational Mechanics* 23(4), pp. 279-287.

Chen, J. and Lu, X.-Y. 2004. Numerical investigation of the non-Newtonian blood flow in a bifurcation model with a non-planar branch. *Journal of biomechanics* 37(12), pp. 1899-1911.

Chen, J. and Lu, X.-Y. 2006. Numerical investigation of the non-Newtonian pulsatile blood flow in a bifurcation model with a non-planar branch. *Journal of biomechanics* 39(5), pp. 818-832.

Chnafa, C. and Mendez, S. and Nicoud, F. 2014. Image-based large-eddy simulation in a realistic left heart. *Computers & Fluids* 94, pp. 173-187.

Cho, Y. I. and Kensey, K. R. 1991. Effects of the non-Newtonian viscosity of blood on flows in a diseased arterial vessel. Part 1: Steady flows. *Biorheology* 28(3-4), pp. 241-262.

Cleary, P. and Ha, J. and Alguine, V. and Nguyen, T. 2002. Flow modelling in casting processes. *Applied Mathematical Modelling* 26(2), pp. 171-190.

Colagrossi, A. and Landrini, M. 2003. Numerical simulation of interfacial flows by smoothed particle hydrodynamics. *Journal of Computational Physics* 191(2), pp. 448-475.

Cole, R. H. and Weller, R. 2009. Underwater explosions. *Physics Today* 1(6), pp. 35-35.

Cummins, S. J. and Rudman, M. 1999. An SPH projection method. *Journal of computational physics* 152(2), pp. 584-607.

Dalrymple, R. and Rogers, B. 2006. Numerical modeling of water waves with the SPH method. *Coastal engineering* 53(2), pp. 141-147.

Dalrymple, R. A. and Knio, O. eds. 2000. *SPH modelling of water waves*. Coastal Dynamics' 01. ASCE.

Darbeau, M. Z. and Lutz, R. J. and Collins, W. E. 2000. Simulated lipoprotein transport in the wall of branched arteries. *ASAIO journal* 46(6), pp. 669-678.

Davies, M. and Bland, J. and Hangartner, J. and Angelina, A. and Thomas, A. 1989. Factors influencing the presence or absence of acute coronary artery thrombi in sudden ischaemic death. *European Heart Journal* 10(3), pp. 203-208.

Deeb, R. (2013). *Flow of self-compacting concrete.* Cardiff University.

Denham, M. 1974. Laminar flow over a downstream-facing step in a two-dimensional flow channel.

Dilts, G. A. 1999. Movement least Square particle Hydrodynamics-I: consistency and stability *Internationa Journal for Numerical Methods in Engineering* 44, pp. 1115-1155.

Dilts, G. A. 2000a. Movement least Square particle Hydrodynamics-II: conservation and boundaries. *Internationa Journal for Numerical Methods in Engineering* 48, pp. 1503-1524.

Ding, E.-J. and Aidun, C. K. 2006. Cluster size distribution and scaling for spherical particles and red blood cells in pressure-driven flows at small Reynolds number. *Physical review letters* 96(20), p. 204502.

Duraiswamy, N. and Schoephoerster, R. T. and Moreno, M. R. and Moore Jr, J. E. 2007. Stented artery flow patterns and their effects on the artery wall. *Annu. Rev. Fluid Mech.* 39, pp. 357-382.

Dyka, C. and Randles, P. and Ingel, R. 1997. Stress points for tension instability in SPH. *International Journal for Numerical Methods in Engineering* 40(13), pp. 2325-2341.

Dzwinel, W. and Boryczko, K. and Yuen, D. A. 2003. A discrete-particle model of blood dynamics in capillary vessels. *Journal of colloid and interface science* 258(1), pp. 163-173.

Eckstein, E. C. and Belgacem, F. 1991. Model of platelet transport in flowing blood with drift and diffusion terms. *Biophysical journal* 60(1), p. 53.

Ellero, M. and Kröger, M. and Hess, S. 2002. Viscoelastic flows studied by smoothed particle dynamics. *Journal of Non-Newtonian Fluid Mechanics* 105(1), pp. 35-51.

Epstein, F. H. and Fuster, V. and Badimon, L. and Badimon, J. J. and Chesebro, J. H. 1992. The pathogenesis of coronary artery disease and the acute coronary syndromes. *New England journal of medicine* 326(4), pp. 242-250.

Filipovic, N. and Kojic, M. and Tsuda, A. 2008. Modelling thrombosis using dissipative particle dynamics method. *Philosophical Transactions of the Royal Society of London A: Mathematical, Physical and Engineering Sciences* 366(1879), pp. 3265-3279.

Flannery, C. J. 2005. Thrombus formation under high shear in arterial stenotic flow.

Fogelson, A. L. 1992. Continuum models of platelet aggregation: formulation and mechanical properties. *SIAM Journal on Applied Mathematics* 52(4), pp. 1089-1110.

Fogelson, A. L. ed. 1993. *Aggregation: Mechanical Properties and Chemically-Induced Phase Transitions*. American Mathematical Soc.

Fogelson, A. L. and Guy, R. D. 2008. Immersed-boundary-type models of intravascular platelet aggregation. *Computer methods in applied mechanics and engineering* 197(25), pp. 2087-2104.

Fogelson, A. L. and Neeves, K. B. 2015. Fluid mechanics of blood clot formation. *Annual review of fluid mechanics* 47, pp. 377-403.

Formaggia, L. and Gerbeau, J.-F. and Nobile, F. and Quarteroni, A. 2001. On the coupling of 3D and 1D Navier–Stokes equations for flow problems in compliant vessels. *Computer Methods in Applied Mechanics and Engineering* 191(6), pp. 561-582.

Formaggia, L. and Gerbeau, J.-F. and Nobile, F. and Quarteroni, A. 2002. Numerical Treatment of Defective Boundary Conditions for the Navier--Stokes Equations. *SIAM Journal on Numerical Analysis* 40(1), pp. 376-401.

Formaggia, L. and Nobile, F. and Quarteroni, A. and Veneziani, A. 1999. Multiscale modelling of the circulatory system: a preliminary analysis. *Computing and visualization in science* 2(2-3), pp. 75-83.

Fox, J. and Hugh, A. 1966. Localization of atheroma: a theory based on boundary layer separation. *British Heart Journal* 28(3), p. 388.

Friedman, M. H. and Brinkman, A. M. and Qin, J. J. and Seed, W. A. 1993. Relation between coronary artery geometry and the distribution of early sudanophilic lesions. *Atherosclerosis* 98(2), pp. 193-199.

Friedman, M. H. and Hutchins, G. M. and Bargeron, C. B. and Deters, O. J. and Mark, F. F. 1981. Correlation between intimal thickness and fluid shear in human arteries. *Atherosclerosis* 39(3), pp. 425-436.

Fry, D. 1973. Responses of the arterial wall to certain physical factors. *Atherogenesis: Initiating Factors*, pp. 93-125.

Fry, D. L. 1968. Acute vascular endothelial changes associated with increased blood velocity gradients. *Circulation research* 22(2), pp. 165-197.

Fry, D. L. 1969. Certain histological and chemical responses of the vascular interface to acutely induced mechanical stress in the aorta of the dog. *Circulation Research* 24(1), pp. 93-108.

Fulk, D. A. and Quinn, D. W. 1996. An analysis of 1-D smoothed particle hydrodynamics kernels. *Journal of Computational Physics* 126(1), pp. 165-180.

Fung, Y.-c. 1993. Mechanical properties and active remodeling of blood vessels.*Biomechanics*. Springer, pp. 321-391.

Fung, Y.-C. 2013. *Biomechanics: mechanical properties of living tissues*. Springer Science & Business Media.

Fuster, V. and Badimon, L. and Cohen, M. and Ambrose, J. A. and Badimon, J. and Chesebro, J. 1988. Insights into the pathogenesis of acute ischemic syndromes. *Circulation* 77(6), pp. 1213-1220.

Ghia, U. and Ghia, K. N. and Shin, C. 1982. High-Re solutions for incompressible flow using the Navier-Stokes equations and a multigrid method. *Journal of computational physics* 48(3), pp. 387-411.

Gijsen, F. and Van de Vosse, F. and Janssen, J. 1999. The influence of the non-Newtonian properties of blood on the flow in large arteries: steady flow in a carotid bifurcation model. *Journal of biomechanics* 32(6), pp. 601-608.

Gijsen, F. F. (1998). *Modeling of wall shear stress in large arteries.* Technische Universiteit Eindhoven.

Gingold, R. A. and Monaghan, J. J. 1977. Smoothed particle hydrodynamics: theory and application to non-spherical stars. *Monthly notices of the royal astronomical society* 181(3), pp. 375-389.

Giordana, S. and Sherwin, S. and Peiró, J. and Doorly, D. and Crane, J. and Lee, K. and Cheshire, N. and Caro, C. 2005. Local and global geometric influence on steady flow in distal anastomoses of peripheral bypass grafts. *Journal of biomechanical engineering* 127(7), pp. 1087-1098.

Gnasso, A. and Irace, C. and Carallo, C. and De Franceschi, M. S. and Motti, C. and Mattioli, P. L. and Pujia, A. 1997. In vivo association between low wall shear stress and plaque in subjects with asymmetrical carotid atherosclerosis. *Stroke* 28(5), pp. 993-998.

Goodman, P. D. and Barlow, E. T. and Crapo, P. M. and Mohammad, S. F. and Solen, K. A. 2005. Computational model of device-induced thrombosis and thromboembolism. *Annals of biomedical engineering* 33(6), pp. 780-797.

Goodman, P. D. and Hall, M. W. and Sukavaneshvar, S. and Solen, K. A. 2000. In vitro model for studying the effects of hemodynamics on device induced thromboembolism in human blood. *ASAIO journal* 46(5), pp. 576-578.

Grotberg, J. B. and Jensen, O. E. 2004. Biofluid mechanics in flexible tubes. *Annual Review of Fluid Mechanics* 36(1), p. 121.

Hale, J. and McDonald, D. and Womersley, J. 1955. Velocity profiles of oscillating arterial flow, with some calculations of viscous drag and the Reynolds number. *The Journal of physiology* 128(3), pp. 629-640.

Harvey, W. 1957. De Motu Cordis. Translated as Movement of the heart and blood in animals. *Blackwell Scientic* 1628(Oxford).

He, S. and Jackson, J. 2000. A study of turbulence under conditions of transient flow in a pipe. *Journal of Fluid Mechanics* 408, pp. 1-38.

Henry, F. and Collins, M. 1993. A novel predictive model with compliance for arterial flows. *ASME-PUBLICATIONS-BED* 26, pp. 131-131.

Hofer, M. and Rappitsch, G. and Perktold, K. and Trubel, W. and Schima, H. 1996. Numerical study of wall mechanics and fluid dynamics in end-to-side anastomoses and correlation to intimal hyperplasia. *Journal of biomechanics* 29(10), pp. 1297-1308.

Hu, X. Y. and Adams, N. A. 2006. A multi-phase SPH method for macroscopic and mesoscopic flows. *Journal of Computational Physics* 213(2), pp. 844-861.

Huikuri, H. V. and Castellanos, A. and Myerburg, R. J. 2001. Sudden death due to cardiac arrhythmias. *New England Journal of Medicine* 345(20), pp. 1473-1482.

Jahangiri, M. and Saghafian, M. and Sadeghi, M. R. 2015. Numerical Study of Turbulent Pulsatile Blood Flow through Stenosed Artery Using Fluid-Solid Interaction. *Computational and Mathematical Methods in Medicine* 2015.

Johnston, B. M. and Johnston, P. R. and Corney, S. and Kilpatrick, D. 2004. Non-Newtonian blood flow in human right coronary arteries: steady state simulations. *Journal of biomechanics* 37(5), pp. 709-720.

Jones, D. 1979. The important of surface area/volume ratio to the rate of oxygen uptake by red cells. *The Journal of general physiology* 74(5), pp. 643-646.

Jou, L.-D. and Berger, S. 1998. Numerical simulation of the flow in the carotid bifurcation. *Theoretical and Computational Fluid Dynamics* 10(1), pp. 239-248.

Kalssen, R. 2002. Astrophysikalishes institute potsdam.[On line] Available at: http://www.ita.uniheidelberg.de/research/klessen/people/klessen/publications/presentations/2002-04-26-SPH-lecture-cardiff.pdf *[Accessed 13/ 04/ 2013]*.

Kamada, H. and Tsubota, K.-i. and Nakamura, M. and Wada, S. and Ishikawa, T. and Yamaguchi, T. 2011. Computational study on effect of stenosis on primary thrombus formation. *Biorheology* 48(2), pp. 99-114.

Kamada, H. and Tsubota, K. i. and Nakamura, M. and Wada, S. and Ishikawa, T. and Yamaguchi, T. 2010. A three-dimensional particle simulation of the formation and collapse of a primary thrombus. *International Journal for Numerical Methods in Biomedical Engineering* 26(3-4), pp. 488-500.

Karino, T. and Goldsmith, H. 1979. Adhesion of human platelets to collagen on the walls distal to a tubular expansion. *Microvascular research* 17(3), pp. 238-262.

Kerber, C. and Hecht, S. and Knox, K. and Buxton, R. and Meltzer, H. 1996. Flow dynamics in a fatal aneurysm of the basilar artery. *American Journal of Neuroradiology* 17(8), pp. 1417-1421.

Keynton, R. S. and Evancho, M. M. and Sims, R. L. and Rodway, N. V. and Gobin, A. and Rittgers, S. E. 2001. Intimal hyperplasia and wall shear in arterial bypass graft distal anastomoses: an in vivo model study. *Journal of biomechanical engineering* 123(5), pp. 464-473.

Khomasuridze, N. and Zirakashvili, N. 2015. Study of Multilayer Flow of Viscous Incompressible Fluid and Application of Its Results for Capillary Blood Flow Simulation.

Kim, H. and Vignon-Clementel, I. and Figueroa, C. and Jansen, K. and Taylor, C. 2010. Developing computational methods for three-dimensional finite element simulations of coronary blood flow. *Finite Elements in Analysis and Design* 46(6), pp. 514-525.

Kleinstreuer, C. 1989. Analysis of particle trajectories in aortic artery bifurcations with stenosis. *Journal of Biomechanicai Engineering NOVEMBER* 111, p. 311.

Kochanek, K. D. and Murphy, S. L. and Anderson, R. N. and Scott, C. 2004. Deaths: final data for 2002. *National vital statistics reports* 53(5), pp. 1-115.

Koshizuka, S., Oka, Y., Tamako, H. 1995. A Particle method for Calculating splashing of incompressible viscous fluid. *proc. Int: International Conference on Mathematics and Computations, Reactor Physics and Environmental Analysis* 2(1514-1521).

Ku, D. N. 1997. Blood flow in arteries. *Annual Review of Fluid Mechanics* 29(1), pp. 399-434.

Ku, D. N. and Giddens, D. P. and Zarins, C. K. and Glagov, S. 1985. Pulsatile flow and atherosclerosis in the human carotid bifurcation. Positive correlation between plaque location and low oscillating shear stress. *Arteriosclerosis, thrombosis, and vascular biology* 5(3), pp. 293-302.

Kuharsky, A. L. and Fogelson, A. L. 2001. Surface-mediated control of blood coagulation: the role of binding site densities and platelet deposition. *Biophysical journal* 80(3), pp. 1050-1074.

Kulasegaram, S. and Bonet, J. and Lewis, R. and Profit, M. 2002. Mould filling simulation in high pressure die casting by meshless method.

Kulasegaram, S. and Karihaloo, B. L. 2012. Fibre-reinforced, self-compacting concrete flow modelled by smooth particle hydrodynamics. *Proceedings of the ICE-Engineering and Computational Mechanics* 166(1), pp. 22-31.

Kulasegaram, S. and Karihaloo, B. L. and Ghanbari, A. 2011. Modelling the flow of self-compacting concrete. *International Journal for Numerical and Analytical Methods in Geomechanics* 35(6), pp. 713-723.

Lassila, R. and Badimon, J. J. and Vallabhajosula, S. and Badimon, L. 1990. Dynamic monitoring of platelet deposition on severely damaged vessel wall in flowing blood. Effects of different stenoses on thrombus growth. *Arteriosclerosis, Thrombosis, and Vascular Biology* 10(2), pp. 306-315.

Lee, D. and Chen, J. 2002. Numerical simulation of steady flow fields in a model of abdominal aorta with its peripheral branches. *Journal of Biomechanics* 35(8), pp. 1115-1122.

Lee, E.-S. and Moulinec, C. and Xu, R. and Violeau, D. and Laurence, D. and Stansby, P. 2008. Comparisons of weakly compressible and truly incompressible algorithms for the SPH mesh free particle method. *Journal of computational physics* 227(18), pp. 8417-8436.

Leiderman Gregg, K. and Fogelson, A. eds. 2009. *A Spatial-Temporal Model of Platelet Deposition and Blood Coagulation Under Flow*. APS Division of Fluid Dynamics Meeting Abstracts.

Lelah, M. D. and Lambrecht, L. K. and Cooper, S. L. 1984. A canine ex vivo series shunt for evaluating thrombus deposition on polymer surfaces. *Journal of biomedical materials research* 18(5), pp. 475-496.

Li, M. and Beech-Brandt, J. and John, L. and Hoskins, P. and Easson, W. 2007. Numerical analysis of pulsatile blood flow and vessel wall mechanics in different degrees of stenoses. *Journal of biomechanics* 40(16), pp. 3715-3724.

Liu, G.-R. and Liu, M. B. 2003. *Smoothed particle hydrodynamics: a meshfree particle method*. World Scientific.

Liu, Q. and Mirc, D. and Fu, B. M. 2008. Mechanical mechanisms of thrombosis in intact bent microvessels of rat mesentery. *Journal of biomechanics* 41(12), pp. 2726-2734.

Longest, P. W. and Kleinstreuer, C. 2003. Comparison of blood particle deposition models for non-parallel flow domains. *Journal of Biomechanics* 36(3), pp. 421-430.

Loth, F. and Jones, S. A. and Zarins, C. K. and Giddens, D. P. and Nassar, R. F. and Glagov, S. and Bassiouny, H. S. 2002. Relative contribution of wall shear stress and injury in experimental intimal thickening at PTFE end-to-side arterial anastomoses. *Journal of biomechanical engineering* 124(1), pp. 44-51.

Lou, Z. and Yang, W.-J. 1991. Biofluid dynamics at arterial bifurcations. *Critical reviews in biomedical engineering* 19(6), pp. 455-493.

Loudon, C. and Tordesillas, A. 1998. The use of the dimensionless Womersley number to characterize the unsteady nature of internal flow. *Journal of theoretical biology* 191(1), pp. 63-78.

Lu, Y. and Lu, X. and Zhuang, L. and Wang, W. 2002. Breaking symmetry in non-planar bifurcations: Distribution of flow and wall shear stress. *Biorheology* 39(4), pp. 431-436.

Lucy, L. B. 1977. A numerical approach to the testing of the fission hypothesis. *The astronomical journal* 82, pp. 1013-1024.

Lutz, R. J. and Cannon, J. N. and Bischoff, K. B. and Dedrick, R. L. and Stiles, R. K. and Fry, D. L. 1977. Wall shear stress distribution in a model canine artery during steady flow. *Circulation Research* 41(3), pp. 391-399.

Mailhac, A. and Badimon, J. J. and Fallon, J. T. and Fernandez-Ortiz, A. and Meyer, B. and Chesebro, J. H. and Fuster, V. and Badimon, L. 1994. Effect of an eccentric severe stenosis on fibrin (ogen) deposition on severely damaged vessel wall in arterial thrombosis. Relative contribution of fibrin (ogen) and platelets. *Circulation* 90(2), pp. 988-996.

Malek, A. M. and Alper, S. L. and Izumo, S. 1999. Hemodynamic shear stress and its role in atherosclerosis. *Jama* 282(21), pp. 2035-2042.

Markou, C. and Hanson, S. and Siegel, J. and Ku, D. 1993. The role of high wall shear rate on thrombus formation in stenoses. *ASME-PUBLICATIONS-BED* 26, pp. 555-555.

Marth, W. and Voigt, A. 2015. Margination of white blood cells-a computational approach by a hydrodynamic phase field model. *arXiv preprint arXiv:1507.01544*.

Matsumoto, T. and Goto, T. and Furukawa, T. and Sato, M. 2004. Residual stress and strain in the lamellar unit of the porcine aorta: experiment and analysis. *Journal of biomechanics* 37(6), pp. 807-815.

Merten, M. and Chow, T. and Hellums, J. D. and Thiagarajan, P. 2000. A new role for P-selectin in shear-induced platelet aggregation. *Circulation* 102(17), pp. 2045-2050.

Michelson, A. D. 2007. Platelets. Second Edition(Academic Press 2007).

Miyazaki, H. and Yamaguchi, T. 2002. Formation and destruction of primary thrombi under the influence of blood flow and von Willebrand factor analyzed by a discrete element method. *Biorheology* 40(1-3), pp. 265-272.

Molteni, D. and Colagrossi, A. 2009. A simple procedure to improve the pressure evaluation in hydrodynamic context using the SPH. *Computer Physics Communications* 180(6), pp. 861-872.

Monaghan, J. 1985. Particle methods for hydrodynamics. *Computer Physics Reports* 3(2), pp. 71-124.

Monaghan, J. and Kos, A. 1999. Solitary waves on a Cretan beach. *Journal of waterway, port, coastal, and ocean engineering* 125(3), pp. 145-155.

Monaghan, J. J. 1982. Why particle methods work. *SIAM Journal on Scientific and Statistical Computing* 3(4), pp. 422-433.

Monaghan, J. J. 1992. Smoothed particle hydrodynamics. *Annual review of astronomy and astrophysics* 30, pp. 543-574.

Monaghan, J. J. 1994. Simulating free surface flows with SPH. *Journal of computational physics* 110(2), pp. 399-406.

Monaghan, J. J. 2000. SPH without a tensile instability. *Journal of Computational Physics* 159(2), pp. 290-311.

Monaghan, J. J., Gingold,R. A,. 1983. Sock Simulation by the Particle method SPH. *Journal of Computation Physics* 55(2), pp. 374-389.

Monaghan, J. J. and Lattanzio, J. C. 1985. A refined particle method for astrophysical problems. *Astronomy and astrophysics* 149, pp. 135-143.

Montecinos, G. I. and Müller, L. O. and Toro, E. F. 2014. Hyperbolic reformulation of a 1D viscoelastic blood flow model and ADER finite volume schemes. *Journal of Computational Physics* 266, pp. 101-123.

Mori, D. and Yano, K. and Tsubota, K.-i. and Ishikawa, T. and Wada, S. and Yamaguchi, T. 2008. Computational study on effect of red blood cells on primary thrombus formation. *Thrombosis research* 123(1), pp. 114-121.

Morris, J. P. and Fox, P. J. and Zhu, Y. 1997. Modeling low Reynolds number incompressible flows using SPH. *Journal of computational physics* 136(1), pp. 214-226.

Morris, M. and Iansek, R. and McGinley, J. and Matyas, T. and Huxham, F. 2005. Three-dimensional gait biomechanics in Parkinson's disease: Evidence for a centrally mediated amplitude regulation disorder. *Movement Disorders* 20(1), pp. 40-50.

Motomiya, M. and Karino, T. 1984. Flow patterns in the human carotid artery bifurcation. *Stroke* 15(1), pp. 50-56.

Moyer, J. D. and Nowak, R. B. and Kim, N. E. and Larkin, S. K. and Peters, L. L. and Hartwig, J. and Kuypers, F. A. and Fowler, V. M. 2010. Tropomodulin 1-null mice have a mild spherocytic elliptocytosis with appearance of tropomodulin 3 in red blood cells and disruption of the membrane skeleton. *Blood* 116(14), pp. 2590-2599.

Mukundakrishnan, K. and Ayyaswamy, P. S. and Eckmann, D. M. 2008. Finite-sized gas bubble motion in a blood vessel: Non-Newtonian effects. *Physical Review E* 78(3), p. 036303.

Müller, K. (2015). *In silico particle margination in blood flow*. Universität zu Köln.

Myerburg, R. J. and Mitrani, R. and Interian, A. and Castellanos, A. 1998. Interpretation of outcomes of antiarrhythmic clinical trials design features and population impact. *Circulation* 97(15), pp. 1514-1521.

Nandalur, K. R. and Baskurt, E. and Hagspiel, K. D. and Finch, M. and Phillips, C. D. and Bollampally, S. R. and Kramer, C. M. 2006. Carotid artery calcification on CT may independently predict stroke risk. *American Journal of Roentgenology* 186(2), pp. 547-552.

Naylor, A. and Mehta, Z. and Rothwell, P. and Bell, P. 2002. Carotid artery disease and stroke during coronary artery bypass: a critical review of the literature. *European journal of vascular and endovascular surgery* 23(4), pp. 283-294.

Nerem, R. 1992. Vascular fluid mechanics, the arterial wall, and atherosclerosis. *Journal of Biomechanical Engineering, Transactions of the ASME* 114(3), pp. 274-282.

Nikparto, A. and Firoozabadi, B. 2011. Numerical study on effects of Newtonian and Non-newtonian blood flow on local hemodynamics in a multi-layer carotid artery Bifurcation. CMM.

Nithiarasu, P. 2016. Robust Finite Element Approaches to Systemic Circulation Using the Locally Conservative Galerkin (LCG) Method. *Proceedings of the Indian National Science Academy* 82(2).

Noordergraaf, A. and Verdouw, P. D. and Boom, H. B. 1963. The use of an analog computer in a circulation model. *Progress in Cardiovascular Diseases* 5(5), pp. 419-439.

Nuyttens, B. P. and Thijs, T. and Deckmyn, H. and Broos, K. 2011. Platelet adhesion to collagen. *Thrombosis research* 127, pp. S26-S29.

O'Brien, V. and Ehrlich, L. W. 1977. Simulation of unsteady flow at renal branches. *Journal of biomechanics* 10(10), pp. 623-631.

Obidowski, D. and Jozwik, K. 2010. *Comparison of Numerical Simulations and Ultrasonography Measurements of the Blood Flow through Vertebral Arteries*. INTECH Open Access Publisher.

Ouared, R. and Chopard, B. 2005. Lattice Boltzmann simulations of blood flow: non-Newtonian rheology and clotting processes. *Journal of statistical physics* 121(1-2), pp. 209-221.

Palmen, D. and Gijsen, F. and Vosse, v. d. F. and Janssen, J. 1997. Diagnostic minor stenoses in carotid artery bifurcation models using the disturbed velocity field. *Journal of Vascular Investigation* 3(1), p. 26.

Panteleev, M. and Sveshnikova, A. and Belyaev, A. and Nechipurenko, D. and Gudich, I. and Obydenny, S. and Dovlatova, N. and Fox, S. and Holmuhamedov, E. 2014. Systems biology and systems pharmacology of thrombosis. *Mathematical Modelling of Natural Phenomena* 9(6), pp. 4-16.

Para, A. N. and Ku, D. N. 2013. A low-volume, single pass in-vitro system of high shear thrombosis in a stenosis. *Thrombosis research* 131(5), pp. 418-424.

Perktold, K. and Florian, H. and Hilbert, D. and Peter, R. 1988. Wall shear stress distribution in the human carotid siphon during pulsatile flow. *Journal of biomechanics* 21(8), pp. 663-671.

Perktold, K. and Hilbert, D. 1986. Numerical simulation of pulsatile flow in a carotid bifurcation model. *Journal of biomedical engineering* 8(3), pp. 193-199.

Perktold, K. and Nerem, R. and Peter, R. 1991. A numerical calculation of flow in a curved tube model of the left main coronary artery. *Journal of biomechanics* 24(3), pp. 175-189.

Perktold, K. and Peter, R. and Gürtl, R. and Bracale, M. and Denoth, F. eds. 1992. *Computer simulation of flow phenomena in distensible arterial bifurcation models*. Proceedings of the VI Mediterranean Conference on Medical and Biological Engineering, MEDICON.

Perktold, K. and Rappitsch, G. 1993. Numerical analysis of arterial wall mechanics and local blood flow phenomena. *ASME-PUBLICATIONS-BED* 26, pp. 127-127.

Perktold, K. and Rappitsch, G. 1995. Computer simulation of local blood flow and vessel mechanics in a compliant carotid artery bifurcation model. *Journal of biomechanics* 28(7), pp. 845-856.

Peskin, C. S. 1977. Numerical analysis of blood flow in the heart. *Journal of computational physics* 25(3), pp. 220-252.

Pivkin, I. V. and Richardson, P. D. and Karniadakis, G. 2006. Blood flow velocity effects and role of activation delay time on growth and form of platelet thrombi. *Proceedings of the National Academy of Sciences* 103(46), pp. 17164-17169.

Pocock, G. and Richards, C. D. and Richards, D. A. 2013. *Human physiology*. Oxford university press.

Pries, A. R. and Secomb, T. W. and Gaehtgens, P. and Gross, J. 1990. Blood flow in microvascular networks. Experiments and simulation. *Circulation research* 67(4), pp. 826-834.

Quarteroni, A. 2001. Modeling the cardiovascular system: a mathematical challenge.*Mathematics Unlimited—2001 and Beyond*. Springer, pp. 961-970.

Rappitsch, G. and Perktold, K. 1996. Computer simulation of convective diffusion processes in large arteries. *Journal of biomechanics* 29(2), pp. 207-215.

Reasor, D. A. and Mehrabadi, M. and Ku, D. N. and Aidun, C. K. 2013. Determination of critical parameters in platelet margination. *Annals of biomedical engineering* 41(2), pp. 238-249.

Reininger, A. 2008. Function of von Willebrand factor in haemostasis and thrombosis. *Haemophilia* 14(s5), pp. 11-26.

Reorowicz, P. and Obidowski, D. and Klosinski, P. and Szubert, W. and Stefanczyk, L. and Jozwik, K. 2014. Numerical simulations of the blood flow in the patient-specific arterial cerebral circle region. *Journal of biomechanics* 47(7), pp. 1642-1651.

Reuderink, P. and Hoogstraten, H. and Sipkema, P. and Hillen, B. and Westerhof, N. 1989. Linear and nonlinear one-dimensional models of pulse wave transmission at high Womersley numbers. *Journal of biomechanics* 22(8), pp. 819-827.

Reuderink, P. J. 1991. Analysis of the flow in a 3D distensible model of the carotid artery bifurcation. *Eindhoven Technical University Thesis*.

Rindt, C. and Steenhoven, A. v. 1996. Unsteady flow in a rigid 3-D model of the carotid artery bifurcation. *Journal of biomechanical engineering* 118(1), pp. 90-96.

Rindt, C. and Van Steenhoven, A. and Janssen, J. and Reneman, R. and Segal, A. 1990. A numerical analysis of steady flow in a three-dimensional model of the carotid artery bifurcation. *Journal of biomechanics* 23(5), pp. 461-473.

Ritchie, B. W. and Thomas, P. A. 2001. Multiphase smoothed-particle hydrodynamics. *Monthly Notices of the Royal Astronomical Society* 323(3), pp. 743-756.

Robert A. Dalrymple , F. A., Omar Knio 2000. SPH Modelling of Water Waves. *Proc. Coastal Dynamics, Lund* (2000), pp. 779-787.

Robinson, M. 2009. Turbulence and Viscous Mixing using Smoothed Particle Hydrodynamics. *PhD thesis,Monash University, Austratia.*

Ruggeri, Z. 2003. Von Willebrand factor, platelets and endothelial cell interactions. *Journal of Thrombosis and Haemostasis* 1(7), pp. 1335-1342.

Ruggeri, Z. M. 2002. Platelets in atherothrombosis. *Nature medicine* 8(11), pp. 1227-1234.

Ruggeri, Z. M. and Dent, J. A. and Saldívar, E. 1999. Contribution of distinct adhesive interactions to platelet aggregation in flowing blood. *Blood* 94(1), pp. 172-178.

Sanyal, A. and Han, H.-C. 2015. Artery buckling affects the mechanical stress in atherosclerotic plaques. *Biomedical engineering online* 14(1), p. S4.

Savage, B. and Saldívar, E. and Ruggeri, Z. M. 1996. Initiation of platelet adhesion by arrest onto fibrinogen or translocation on von Willebrand factor. *Cell* 84(2), pp. 289-297.

Schmugge, M. and Rand, M. L. and Freedman, J. 2003. Platelets and von Willebrand factor. *Transfusion and apheresis science* 28(3), pp. 269-277.

Shahriari, S. and Kadem, L. and Rogers, B. and Hassan, I. 2012. Smoothed particle hydrodynamics method applied to pulsatile flow inside a rigid two-dimensional model of left heart cavity. *International journal for numerical methods in biomedical engineering* 28(11), pp. 1121-1143.

Shao, S. and Gotoh, H. 2004. Simulating coupled motion of progressive wave and floating curtain wall by SPH-LES model. *Coastal Engineering Journal* 46(02), pp. 171-202.

Shao, S. and Lo, E. Y. 2003. Incompressible SPH method for simulating Newtonian and non-Newtonian flows with a free surface. *Advances in Water Resources* 26(7), pp. 787-800.

Shi, L. and Zhang, L. and Cao, W. and Chen, G. 2017. Analysis Enhanced Particle-based Flow Visualization. *Electronic Imaging* 2017(1), pp. 12-21.

Siljander, P. and Lassila, R. 1999. Studies of adhesion-dependent platelet activation. *Arteriosclerosis, thrombosis, and vascular biology* 19(12), pp. 3033-3043.

Sorensen, E. N. and Burgreen, G. W. and Wagner, W. R. and Antaki, J. F. 1999. Computational simulation of platelet deposition and activation: I. Model development and properties. *Annals of biomedical engineering* 27(4), pp. 436-448.

Sousa, L. C. and Castro, C. F. and António, C. C. and Chaves, R. 2012. Blood flow simulation and vascular reconstruction. *Journal of biomechanics* 45(15), pp. 2549-2555.

Springer, T. A. 1995. Traffic signals on endothelium for lymphocyte recirculation and leukocyte emigration. *Annual review of physiology* 57(1), pp. 827-872.

Stamatelos, F. G. and Anagnostopoulos, J. S. 2008. Simulation of Viscous Flows with a Gridless Particle Method.

Stangeby, D. K. and Ethier, C. R. 2002. Computational analysis of coupled blood-wall arterial LDL transport. *Journal of biomechanical engineering* 124(1), pp. 1-8.

Steinman, D. and Frayne, R. and Zhang, X.-D. and Rutt, B. and Ethier, C. 1996. MR measurement and numerical simulation of steady flow in an end-to-side anastomosis model. *Journal of biomechanics* 29(4), pp. 537-542.

Stergiopulos, N. 1990. Computer simulation of arterial blood flow.

Stiehm, M. and Wüstenhagen, C. and Grabow, N. and Schmitz, K.-P. 2016. Transient Euler-Lagrange/DEM simulation of stent thrombosis. *Current Directions in Biomedical Engineering* 2(1), pp. 297-300.

Strony, J. and Beaudoin, A. and Brands, D. and Adelman, B. 1993. Analysis of shear stress and hemodynamic factors in a model of coronary artery stenosis and thrombosis. *American Journal of Physiology-Heart and Circulatory Physiology* 265(5), pp. H1787-H1796.

Stubley, G. and Strong, A. and Hale, W. and Absolom, D. 1987. A review of mathematical-models for the prediction of blood-cell adhesion. *Physicochemical Hydrodynamics* 8(2), pp. 221-235.

Sultanov, R. A. and Guster, D. 2008. Computer Simulations of Pulsatile Human Blood Flow Through 3D-Models of the Human Aortic Arch, Vessels of Simple Geometry and a Bifurcated Artery: Investigation of Blood Viscosity and Turbulent Effects. *arXiv preprint arXiv:0811.1363*.

Sultanov, R. A. and Guster, D. eds. 2009. *Full dimensional computer simulations to study pulsatile blood flow in vessels, aortic arch and bifurcated veins: Investigation of blood viscosity and turbulent effects*. 2009 Annual International Conference of the IEEE Engineering in Medicine and Biology Society. IEEE.

Sultanov, R. A. and Guster, D. and Engelbrekt, B. and Blankenbecler, R. eds. 2008. *3D Computer Simulations of Pulsatile Human Blood Flows in Vessels and in the Aortic Arch: Investigation of Non-Newtonian Characteristics of Human Blood*. Computational Science and Engineering, 2008. CSE'08. 11th IEEE International Conference on. IEEE.

Swegle, J. and Hicks, D. and Attaway, S. 1995. Smoothed particle hydrodynamics stability analysis. *Journal of computational physics* 116(1), pp. 123-134.

Tafazzoli-Shadpour, M. 1999. Analysis of mechanical stress in arteries with changes in wall structural properties. *Graduate School of Biomedical Engineering*.

Takeda, H. and Miyama, S. M. and Sekiya, M. 1994. Numerical simulation of viscous flow by smoothed particle hydrodynamics. *Progress of Theoretical Physics* 92(5), pp. 939-960.

Tamagawa, M. and Matsuo, S. 2004. Predictions of thrombus formation using lattice Boltzmann method (modeling of adhesion force for particles to wall). *JSME International Journal Series C Mechanical Systems, Machine Elements and Manufacturing* 47(4), pp. 1027-1034.

Tang, D. and Yang, C. and Zheng, J. and Woodard, P. K. and Saffitz, J. E. and Sicard, G. A. and Pilgram, T. K. and Yuan, C. 2005. Quantifying effects of plaque structure and material properties on stress distributions in human atherosclerotic plaques using 3D FSI models. *Journal of biomechanical engineering* 127(7), pp. 1185-1194.

Tangelder, G. and Teirlinck, H. C. and Slaaf, D. W. and Reneman, R. S. 1985. Distribution of blood platelets flowing in arterioles. *American Journal of Physiology-Heart and Circulatory Physiology* 248(3), pp. H318-H323.

Tapson, V. F. 2008. Acute pulmonary embolism. *New England Journal of Medicine* 358(10), pp. 1037-1052.

Taylor, C. A. and Cheng, C. P. and Espinosa, L. A. and Tang, B. T. and Parker, D. and Herfkens, R. J. 2002. In vivo quantification of blood flow and wall shear stress in the human abdominal aorta during lower limb exercise. *Annals of biomedical engineering* 30(3), pp. 402-408.

Taylor, C. A. and Hughes, T. J. and Zarins, C. K. 1998a. Finite element modeling of blood flow in arteries. *Computer methods in applied mechanics and engineering* 158(1), pp. 155-196.

Taylor, C. A. and Hughes, T. J. and Zarins, C. K. 1998b. Finite element modeling of three-dimensional pulsatile flow in the abdominal aorta: relevance to atherosclerosis. *Annals of biomedical engineering* 26(6), pp. 975-987.

Texon, M. 1960. The hemodynamic concept of atherosclerosis. *Bulletin of the New York Academy of Medicine* 36(4), p. 263.

Ting, T. S. and Prakash, M. and Cleary, P. and Thompson, M. 2006. Simulation of high Reynolds number flow over a backward facing step using SPH. *ANZIAM Journal* 47, pp. 292-309.

Tosenberger, A. and Ataullakhanov, F. and Bessonov, N. and Panteleev, M. A. and Tokarev, A. and Volpert, V. 2012. The role of platelets in blood coagulation during thrombus formation in flow.

Tsubota, K.-i. and Wada, S. and Yamaguchi, T. 2006. Particle method for computer simulation of red blood cell motion in blood flow. *Computer methods and programs in biomedicine* 83(2), pp. 139-146.

Turitto, V. T. and Hall, C. L. 1998. Mechanical factors affecting hemostasis and thrombosis. *Thrombosis research* 92(6), pp. S25-S31.

Vandegriff, K. and Olson, J. 1984. Morphological and physiological factors affecting oxygen uptake and release by red blood cells. *Journal of Biological Chemistry* 259(20), pp. 12619-12627.

Varghese, S. S. and Frankel, S. H. 2003. Numerical modeling of pulsatile turbulent flow in stenotic vessels. *Journal of biomechanical engineering* 125(4), pp. 445-460.

Viles-Gonzalez, J. F. and Fuster, V. and Badimon, J. J. 2004. Atherothrombosis: a widespread disease with unpredictable and life-threatening consequences. *European heart journal* 25(14), pp. 1197-1207.

Violeau, D. and Issa, R. 2007. Numerical modelling of complex turbulent free-surface flows with the SPH method: an overview. *International Journal for Numerical Methods in Fluids* 53(2), pp. 277-304.

Wada, S. and Karino, T. 2002. Theoretical prediction of low-density lipoproteins concentration at the luminal surface of an artery with a multiple bend. *Annals of biomedical engineering* 30(6), pp. 778-791.

Waite, L. and Fine, J. M. 2007. Applied biofluid mechanics.

Welton, W. C. 1998. Two-dimensional PDF/SPH simulations of compressible turbulent flows. *Journal of Computational Physics* 139(2), pp. 410-443.

Wensing, P. and Scholten, F. and Buijs, P. and Hartkamp, M. and Mali, W. and Hillen, B. 1995. Arterial tortuosity in the femoropopliteal region during knee flexion: a magnetic resonance angiographic study. *Journal of anatomy* 187(Pt 1), p. 133.

Westerhof, N. and Noordergraaf, A. 1970. Arterial viscoelasticity: a generalized model: effect on input impedance and wave travel in the systematic tree. *Journal of Biomechanics* 3(3), pp. 357IN15371-15370IN16379.

Williams, J. and Holmes, D. and Tilke, P. 2011. Parallel Computation Particle Methods for Multi-Phase Fluid Flow with Application Oil Reservoir

Characterization. In: Oñate, E. and Owen, R. eds. *Particle-Based Methods*. Vol. 25. Springer Netherlands, pp. 113-134.

Womersley, J. R. 1955. Method for the calculation of velocity, rate of flow and viscous drag in arteries when the pressure gradient is known. *The Journal of physiology* 127(3), pp. 553-563.

Womersley, J. R. (1957). *An elastic tube theory of pulse transmission and oscillatory flow in mammalian arteries*. DTIC Document.

Woodside, D. and Liu, S. and Ginsberg, M. H. 2001. Integrin activation. *Thrombosis and haemostasis* 86(1), pp. 316-323.

Wootton, D. M. and Ku, D. N. 1999. Fluid mechanics of vascular systems, diseases, and thrombosis. *Annual review of biomedical engineering* 1(1), pp. 299-329.

Wróblewski, P. and Boryczko, K. and Kopeæ, M. 2007. SPH-a comparison of neighbor search methods based on constant number of neighbors and constant cut-off radius. *TASK Quart* 11, pp. 275-285.

Wu, Y. and Cai, X.-C. 2011. A parallel two-level method for simulating blood flows in branching arteries with the resistive boundary condition. *Computers & Fluids* 45(1), pp. 92-102.

Wylie, E. B. and Streeter, V. L. and Suo, L. 1993. *Fluid transients in systems*. Prentice Hall Englewood Cliffs, NJ.

Xiong, G. and Figueroa, C. A. and Xiao, N. and Taylor, C. A. 2011. Simulation of blood flow in deformable vessels using subject-specific geometry and spatially varying wall properties. *International journal for numerical methods in biomedical engineering* 27(7), pp. 1000-1016.

Xu, Z. and Chen, N. and Kamocka, M. M. and Rosen, E. D. and Alber, M. 2008. A multiscale model of thrombus development. *Journal of the Royal Society Interface* 5(24), pp. 705-722.

Yazdani, S. K. (2003). *Geometry induced flow disturbances.* Virginia Polytechnic Institute and State University.

Yokoi, K. and Xiao, F. and Liu, H. and Fukasaku, K. 2005. Three-dimensional numerical simulation of flows with complex geometries in a regular Cartesian grid and its application to blood flow in cerebral artery with multiple aneurysms. *Journal of computational physics* 202(1), pp. 1-19.

Zarins, C. K. and Giddens, D. P. and Bharadvaj, B. and Sottiurai, V. S. and Mabon, R. F. and Glagov, S. 1983. Carotid bifurcation atherosclerosis. Quantitative correlation of plaque localization with flow velocity profiles and wall shear stress. *Circulation research* 53(4), pp. 502-514.

Zhao, H. and Shaqfeh, E. S. 2011. Shear-induced platelet margination in a microchannel. *Physical Review E* 83(6), p. 061924.

Zheng, X. and Duan, W.-y. 2010. Numerical simulation of dam breaking using smoothed particle hydrodynamics and viscosity behavior. *Journal of Marine Science and Application* 9(1), pp. 34-41.

Zheng, Y. and Chen, J. and López, J. A. 2015. Flow-driven assembly of VWF fibres and webs in in vitro microvessels. *Nature communications* 6.

APPENDIX A

A.1 Corrected SPH Integration

The origin equation of the SPH approximations is given by Equation (3.9). However, it cannot approximate the functions $\phi(\mathbf{x})$ and $\nabla\phi(\mathbf{x})$ accurately. Therefore, corrected SPH equations have been modified to address these problems (Bonet and Lok 1999; Bonet and Kulasegaram 2000a). The main purpose of the correction techniques is to investigate the conservation of angular momentum, which is not similar to linear momentum.

A.1.1 Preservation of Momentum

The total motion of the particles is preserved, such as linear and angular momentum.

The motion of each particle can be integrated from the instantaneous acceleration vector $\boldsymbol{a}$. Newton's Second Law of Motion represents the particle movement:

$$m_a \boldsymbol{a}_a = \boldsymbol{T}_a^{int} - \boldsymbol{T}_a^{ext} \tag{A.1}$$

where $\boldsymbol{T}_a^{ext}$ represents the external forces acting on a particle 'a', and $\boldsymbol{T}_a^{int}$ represents the internal forces due to the state of stress inside the material. Meanwhile, the most common expression used for the internal forces is:

$$\boldsymbol{T}_a^{int} = \sum_{b=1}^{N} V_a V_b (p_b \pm p_a) \nabla W_a(\mathbf{x}_b) \tag{A.2}$$

where the stress tensor $\sigma = p\mathbf{I}$, p is the mean stress and $\mathbf{I}$ is the identity tensor.

A.1.1.1 Linear Momentum

The linear momentum of the particles is

$$\boldsymbol{G} = \sum_{a=1}^{N} m_a \mathbf{v}_a \qquad (A.3)$$

By adding the derivative of time of (A.3) with equation of (A.2), we find that the rate of change of the linear momentum is

$$\boldsymbol{G}' = \sum_{a=1}^{N} m_a \boldsymbol{a}_a = -\sum_{a=1}^{N} \boldsymbol{T}_a^{int} \qquad (A.4)$$

where the condition of the preservation of the linear momentum is

$$\sum_{a=1}^{N} \boldsymbol{T}_a^{int} = 0 \qquad (A.5)$$

Thus, the internal forces on particle *a* are equal to

$$\boldsymbol{T}_a^{int} = \sum_{b=1}^{N} \boldsymbol{T}_{ab} \qquad (A.6)$$

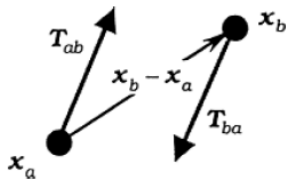

Figure A. 1 The forces between two particles

Depending on equation (A.2), and as shown in $\nabla W_a(\mathbf{x}_b) = -\nabla W_b(\mathbf{x}_a)$, we find that $\boldsymbol{T}_{ab} = -\boldsymbol{T}_{ba}$ and then the sum of the all interaction pairs will vanish and consequently equation (A.4) will be satisfied.

A.1.1.2 Angular Momentum

The total angular momentum of the particles is given by:

$$\boldsymbol{H} = \sum_{a=1}^{N} \mathbf{x}_a * m_a \mathbf{v}_a \qquad (A.7)$$

While the time differentiation is shown as:

$$\boldsymbol{H}' = \sum_{a=1}^{N} \mathbf{x}_a * m_a \boldsymbol{a}_a = -\sum_{a=1}^{N} \mathbf{x}_a * \boldsymbol{T}_a^{int} \qquad (A.8)$$

Where the angular momentum can be preserved as long as the total moment of the internal forces vanishes, and is:

$$\sum_{a=1}^{N} \mathbf{x}_a * \boldsymbol{T}_a^{int} = 0 \qquad (A.9)$$

The origin of the total moment of the two forces as shown in Figure (A.1) can be shown as:

$$\mathbf{x}_a * \boldsymbol{T}_{ab} + \mathbf{x}_b * \boldsymbol{T}_{ba} = -(\mathbf{x}_b - \mathbf{x}_a) * \boldsymbol{T}_{ab} \qquad (A.10)$$

As above, $\boldsymbol{T}_{ab} = -\boldsymbol{T}_{ba}$ is used. This expression will give a chance to vanish whenever the interaction force is collinear with the vector $(\mathbf{x}_b - \mathbf{x}_a)$ which joins two

particles, consequently it is not always satisfied. In this situation, more derivation is required to provide the preservation of angular momentum.

Another option is that the invariance of the potential energy with respect to rigid body rotations can lead to the preservation of angular momentum. To prove this point, consider a rigid body rotation about the origin as described by a set of velocities which are given in terms of an angular velocity vector $\boldsymbol{w}$ with the components $[w_x \quad w_y \quad w_z]^{\mathrm{T}}$, where the vector of velocity at any point as is:

$$\mathbf{v}(\mathbf{x}) = \boldsymbol{w} * \mathbf{x} \tag{A.11}$$

The gradient of the velocity can be shown by derivation to give

$$\nabla \mathbf{v} = \boldsymbol{W} \tag{A.12}$$

$$\boldsymbol{W} = \begin{bmatrix} 0 & -w_z & w_y \\ w_z & 0 & -w_x \\ -w_y & w_x & 0 \end{bmatrix} \tag{A.13}$$

where the rate of deformation tensor $\boldsymbol{\varepsilon}'$ as shown in Eq. (A.14) vanishes and given the skew symmetric nature of $\boldsymbol{W}$

$$\boldsymbol{d} = \frac{1}{2}(\nabla \mathbf{v} + \nabla \mathbf{v}^T) \tag{A.14}$$

The total potential energy would be independent of rigid body translations. Meanwhile, if the SPH approximation is applied, then the gradient of the velocity can be calculated as:

$$\nabla \mathbf{v}_a = \sum_{b=1}^{N} V_b (W\mathbf{x}_b - W\mathbf{x}_a) \otimes \nabla W_b(\mathbf{x}_a) \tag{A.15}$$

The correct skew-symmetric tensor can only be obtained if the gradient of the kernel function investigates the following matrix condition:

$$\sum_{b=1}^{N} V_b(W\mathbf{x}_b - W\mathbf{x}_a) \otimes \nabla W_b(\mathbf{x}_a) = \mathbf{I} \qquad (A.16)$$

where $\mathbf{x}_a$, $\mathbf{x}_b$ are the position vectors of particles *a* and *b*, respectively.

Because the standard SPH algorithm does not generally accept this condition, the angular momentum will not be preserved. A number of correction techniques can be used and, therefore, can overcome this shortcoming. Either the gradient of the kernel is addressed directly (Bonet and Lok 1999) or the kernel function itself is modified (Li and Liu, 1996). Another possibility is to mix the kernel and gradient corrections (Bonet and Lok 1999; Bonet and Kulasegaram 2000a).

A.2 Gradient Correction

The kernel gradient has been modified by introducing a correction matrix $\boldsymbol{L}$ as:

$$\widetilde{\nabla} W_b(\mathbf{x}) = \boldsymbol{L}\nabla W_b(\mathbf{x}) \qquad (A.17)$$

Every term in Equation (A.16) without subscript *a* is used and the term $\nabla W_b(\mathbf{x})$ is changed by its corrected one in Eq. (A.17), which is

$$\sum_{b=1}^{N} \frac{m_b}{\rho_b}(\mathbf{x}_b - \mathbf{x}) \otimes \boldsymbol{L}\nabla W_b(\mathbf{x}) = \mathbf{I} \qquad (A.18)$$

where, $\boldsymbol{L}$ is given by

$$\boldsymbol{L} = \left(\sum_{b=1}^{N} \frac{m_b}{\rho_b} \nabla W_b(\mathbf{x}) \otimes (\mathbf{x}_b - \mathbf{x}) \right)^{-1} \qquad (A.19)$$

A.2.1 Kernel Correction

The kernel is corrected and modified to confirm that polynomial functions up to a given degree are exactly interpolated. The linear kernel correction is given by,

$$\widetilde{W}_b = W_b(\mathbf{x})\alpha(\mathbf{x})\{1 + \boldsymbol{\beta}(\mathbf{x}).(\mathbf{x} - \mathbf{x}_b)\} \qquad (A.20)$$

The correction formulation for velocity, which represents the linear field formulation is,

$$\mathbf{v}_0 + \mathbf{v}_1.\mathbf{x} \quad = \sum_{b=1}^{N} \frac{m_b}{\rho_b}(\mathbf{v}_0 + \mathbf{v}_1.\mathbf{x}_b)\widetilde{W}_b(\mathbf{x}) \qquad (A.21)$$

The following supplement conditions must be pleased,

$$\sum_{b=1}^{N} \frac{m_b}{\rho_b}\widetilde{W}_b(\mathbf{x}) = 1 \qquad (A.22)$$

$$\sum_{b=1}^{N} \frac{m_b}{\rho_b}(\mathbf{x} - \mathbf{x}_b)\,\widetilde{W}_b(\mathbf{x}) = 0 \qquad (A.23)$$

by substituting (A.20) into (A.23) to get the vector parameter$\boldsymbol{\beta}(\mathbf{x})$,

$$\boldsymbol{\beta}(\mathbf{x}) = \frac{\sum_{b=1}^{N} \frac{m_b}{\rho_b}\widetilde{W}_b(\mathbf{x} - \mathbf{x}_b)}{\sum_{b=1}^{N} \frac{m_b}{\rho_b}(\mathbf{x} - \mathbf{x}_b)\otimes\widetilde{W}_b(\mathbf{x} - \mathbf{x}_b)} \qquad (A.24)$$

The scaler parameter $\alpha(\mathbf{x})$can get from substituting (A.20) into (A.22),

$$\alpha(\mathbf{x}) = \frac{1}{\sum_{b=1}^{N} \frac{m_b}{\rho_b}\{1 + \boldsymbol{\beta}(\mathbf{x}).(\mathbf{x} - \mathbf{x}_b)\}W_b(\mathbf{x})} \qquad (A.25)$$

It can be seen from (A.24) and (A.25) that both $\alpha(\mathbf{x})$ and $\boldsymbol{\beta}(\mathbf{x})$ are functions of **x** and this will make the correction expensive in terms of computational time. It can follow that one

way to make the correction less time consuming is by ignoring $\boldsymbol{\beta}(\mathbf{x})$; that is, the kernel is corrected by using a constant rather than a linear correction. Thus, the interpolation of the field function $\mathbf{v}(\mathbf{x})$ is,

$$\mathbf{v}(\mathbf{x}) = \sum_{b=1}^{N} \frac{m_b}{\rho_b} \mathbf{v}_b \widetilde{W}_b(\mathbf{x}) \qquad (A.26)$$

where,

$$\widetilde{W}_b(\mathbf{x}) = \frac{W_b}{\sum_{b=1}^{N} \frac{m_b}{\rho_b} W_b(\mathbf{x})} \qquad (A.27)$$

A.2.2 Combined Kernel and Gradient Correction

Mixing the kernel and gradient corrections is considered to be another correction technique. Where the corrected gradient of the corrected kernel is shown by,

$$\widetilde{\nabla}\widetilde{W}_b(\mathbf{x}) = \boldsymbol{L}\nabla\widetilde{W}_b(\mathbf{x}) \qquad (A.28)$$

Here the term $\widetilde{W}_b(\mathbf{x})$ can be achieved by differentiating Equation (A.28) to give,

$$\widetilde{W}_b(\mathbf{x}) = \frac{\nabla W_b(\mathbf{x}) - \boldsymbol{\varepsilon}(\mathbf{x})}{\sum_{b=1}^{N} \frac{m_b}{\rho_b} W_b(\mathbf{x})} \qquad (A.29)$$

where,

$$\boldsymbol{\varepsilon}(\mathbf{x}) = \frac{\sum_{b=1}^{N} \frac{m_b}{\rho_b} \nabla W_b(\mathbf{x})}{\sum_{b=1}^{N} \frac{m_b}{\rho_b} W_b(\mathbf{x})} \qquad (A.30)$$

The same applies to Equation (A.19), the correction matrix $\boldsymbol{L}$ is given by,

$$\boldsymbol{L} = \left(\sum_{b=1}^{N} \frac{m_b}{\rho_b} \nabla \widetilde{W}_b(\mathbf{x}) \otimes \mathbf{x}_b \right)^{-1} \tag{A.31}$$

It is very important to note that in Equation (A.31) the term of **x** is not required only if the constant kernel is used instead of a linear kernel. By using the corrected gradient of the corrected kernel, the equations of the SPH such as (3.20) and (3.21) can be rewritten as follows,

$$\phi(\mathbf{x}) = \sum_{b=1}^{N} V_b \, \phi(\mathbf{x}_b) \widetilde{W}_b(\mathbf{x}) \tag{A.32}$$

$$\nabla\phi(\mathbf{x}) = \sum_{b=1}^{N} V_b \, \phi(\mathbf{x}_b) \widetilde{\nabla} \, \widetilde{W}_b(\mathbf{x}) \tag{A.33}$$

APPENDIX B

B.1 Basic concepts and assumptions

B.1.1 Finite control volume

The finite control volume will be considered to be a finite region of a flow field, as presented in Figure B.1. Let a control volume be appointed as V, and a control surface as S, to this flow. The control volume has two movements. The first will be fixed in space, and the flow passes through it. The second can move with the flow in such a way that a constant number of fluid particles are always inside it. The fundamental physical principles are applied to the fluid inside the control volume, which derives the equations of fluid flow in an integral form. The final form of the integral fluid equations will be converted to partial differential equations. The conservation form of the governing equations will represent the concept of a fixed control volume, while the non-conservation form of the governing equations will be shown in the concept of a moving control volume in either integral or partial differential form.

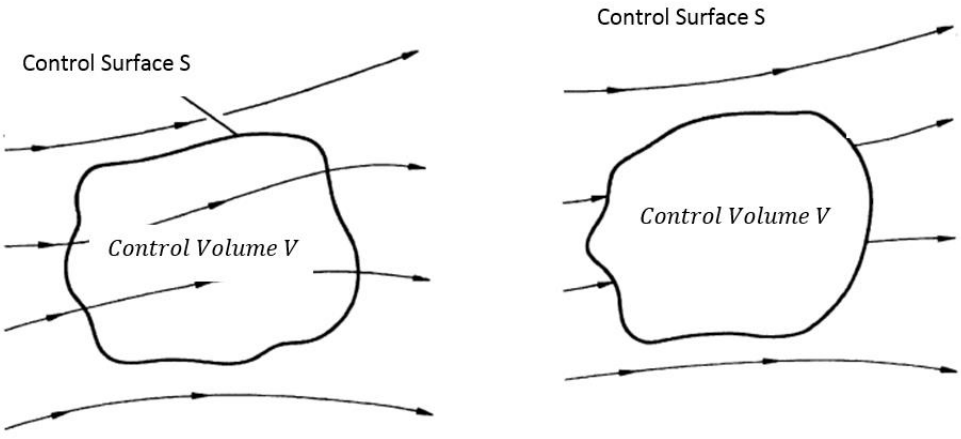

Figure B.1 Fixed control volume (left) and moving control volume (right)

B.1.2 Infinitesimal fluid element

Consider a general flow field as shown in Figure B.2. On the one hand, the small fluid element with a differential volume dV can be considered. On the other hand, this volume has to be large enough to get a massive number of molecules in order to consider it as a continuous medium. It can also be considered that the movement of the fluid element can be fixed in space and the flow through it or it can move with the flow in such a way that a constant number of fluid particles are always inside it. This approach can directly give the partial differential equations. These equations can be obtained based on fixed or moving fluid elements, which yield the conservation and non-conservation forms of the equations, respectively.

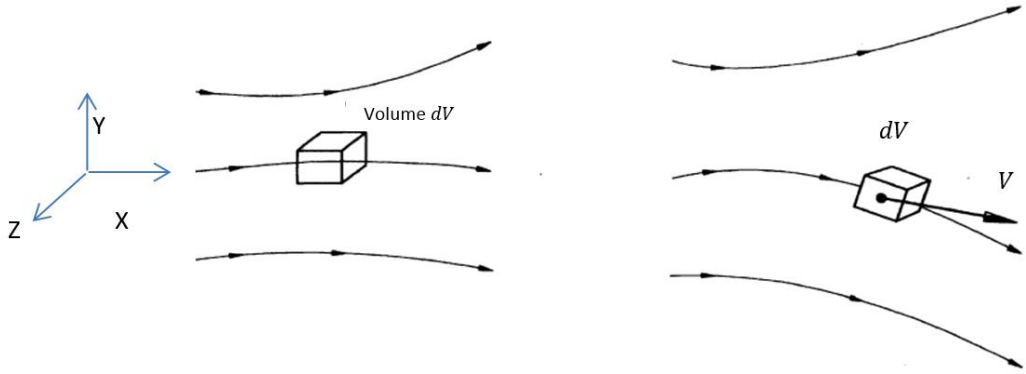

Figure B. 2 Infinitesimal fluid element approach with fixed (left) and moving control element (right)

B.1.3 Material derivatives

The substantial derivative (i.e. time rate of change following a moving fluid element) is an important physical concept in fluid dynamics. The infinitesimal fluid cell moving with the flow (right of Figure B.2) at instants, t_1 and t_2 can be considered, where the scalar density field at time t_1 can be given by:

$$\rho_1 = \rho(x_1, y_1, z_1, t_1) \tag{B.1}$$

While at the second time t_2 the density will be:

$$\rho_2 = \rho(x_2, y_2, z_2, t_2) \tag{B.2}$$

The expression in Equation (B.2) can be expanded in Taylor's series about point t_1 (Anderson 1995) to get:

$$\rho_2 = \rho_1 + \left(\frac{\partial \rho}{\partial x}\right)_1 (x_2 - x_1) + \left(\frac{\partial \rho}{\partial y}\right)_1 (y_2 - y_1) + \left(\frac{\partial \rho}{\partial z}\right)_1 (z_2 - z_1) + \left(\frac{\partial \rho}{\partial t}\right)_1 (t_2 - t_1) + (higher\ order\ terms) \tag{B.3}$$

By dividing both sides of Equation (B.3) by $(t_2 - t_1)$ and neglecting the higher order terms, gives:

$$\frac{\rho_2 - \rho_1}{t_2 - t_1} = \left(\frac{\partial \rho}{\partial x}\right)_1 \left(\frac{x_2 - x_1}{t_2 - t_1}\right) + \left(\frac{\partial \rho}{\partial y}\right)_1 \left(\frac{y_2 - y_1}{t_2 - t_1}\right) + \left(\frac{\partial \rho}{\partial z}\right)_1 \left(\frac{z_2 - z_1}{t_2 - t_1}\right) \left(\frac{\partial \rho}{\partial t}\right)_1 \tag{B.4}$$

Usually, the left-hand side of Equation (B.4) is represented physically by the average time rate of change in density of the fluid element. Where it moves from point 1 to point 2. When t_2 approaches t_1, the term comes to the limit

$$\lim_{t_2 \to t_1} \left(\frac{\rho_2 - \rho_1}{t_2 - t_1}\right) \equiv \frac{D\rho}{Dt} \tag{B.5}$$

Where the expression $\frac{D\rho}{Dt}$ represents the time rate of change of the fluid element which refers to the change of density, when it moves through point 1. Meanwhile, the term $\frac{\partial \rho}{\partial t}$ represents the time rate of change of the density at a fixed point 1. Again, taking the limit of the other terms in the RHS of Equation (B.4) will give:

$$\lim_{t_2 \to t_1} \left(\frac{x_2 - x_1}{t_2 - t_1}\right) \equiv v_x$$

$$\lim_{t_2 \to t_1} \left(\frac{y_2 - y_1}{t_2 - t_1}\right) \equiv v_y \qquad \text{(B. 6)}$$

$$\lim_{t_2 \to t_1} \left(\frac{z_2 - z_1}{t_2 - t_1}\right) \equiv v_z$$

Thus, Equation (B.4) becomes:

$$\frac{D\rho}{Dt} \equiv v_x \frac{\partial \rho}{\partial x} + v_y \frac{\partial \rho}{\partial y} + v_z \frac{\partial \rho}{\partial z} + \frac{\partial \rho}{\partial t} \qquad \text{(B. 7)}$$

Equation (B.7) is considered to be a general expression which can be used for substantial derivatives

$$\frac{D\rho}{Dt} \equiv v_x \frac{\partial}{\partial x} + v_y \frac{\partial}{\partial y} + v_z \frac{\partial}{\partial z} + \frac{\partial}{\partial t} \qquad \text{(B. 8)}$$

where the vector operator ∇ is defined as follows:

$$\nabla \equiv \vec{\imath} \frac{\partial}{\partial x} + \vec{\jmath} \frac{\partial}{\partial y} + \vec{k} \frac{\partial}{\partial z} \qquad \text{(B. 9)}$$

Equation (B.8) can be rewritten in the Cartesian coordinates as:

$$\frac{D}{Dt} \equiv \frac{\partial}{\partial t} + (\mathbf{v}.\nabla) \qquad \text{(B. 10)}$$

Where $\mathbf{v}.\nabla$ is called the convective derivative, which represents the physical term of the time rate of change where the fluid element moves from one place to another in the flow field. The substantial derivative can be applied for any flow field variable (e.g. pressure, temperature, etc.).

B.1.4 Physical meaning of the divergence of velocity

The divergence of the velocity is considered to be a term which frequently becomes clear when dealing with fluid dynamics problems. A moving control volume in a flow field can be considered as in the right side of figure B.1. This control volume contains the same particles as it moves through the flow. Where the control volume moves to a different location of the fluid, its volume V and control surface S can be changed because at its new position a different value of ρ exists. The shape and volume of the moving control volume with a constant mass is constantly changed and it will depend on the characteristics of the flow. An infinitesimal element can be considered moving at local velocity **v**, with surface dS and volume ΔV. Figure B.3 presents the change in volume of the control volume ΔV over a time increment Δt.

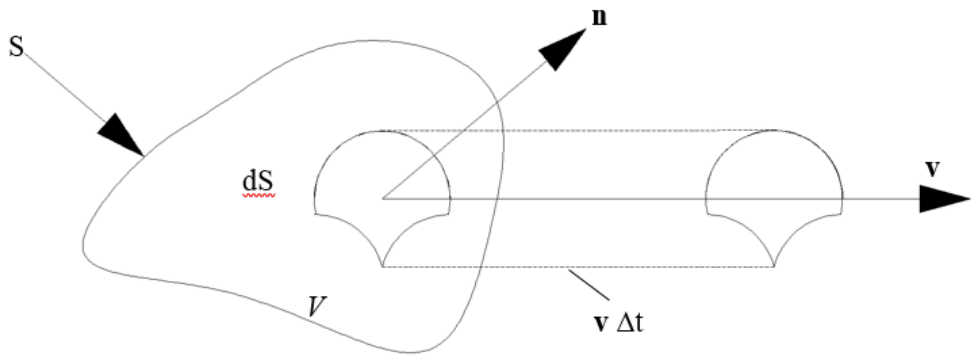

Figure B.3 Physical meaning of the divergence of velocity

Figure B.3 shows that the change in volume is equal to the volume of the cylinder with the base area dS and an upturn $(\mathbf{v}\Delta t).\mathbf{n}$, where, **n** is a unit vector perpendicular to the surface. The change in volume is equal to

$$\Delta V = [(\mathbf{v}\Delta t).\mathbf{n}]\mathrm{dS} \qquad (\mathrm{B}.11)$$

The total volume change of the complete control volume is the integral over the total control surface S

$$\Delta V = \int_{S} \mathbf{v}\Delta t.\mathbf{n}\mathrm{d}S \qquad (\mathrm{B}.12)$$

By dividing both sides of Equation (B.12) by Δt and applying the divergence theorem yields:

$$\frac{\Delta V}{\Delta t} = \int_{V} \nabla.\mathbf{v}dV \qquad (\mathrm{B}.13)$$

Here, the symbol ∇ represents the divergence operator (B.9)

The left-hand side of Equation (B.13) refers to the substantial derivative of V, which in this case deals with the time rate of change of the control volume as the volume moves with the flow.

Equation (B.13) is written in another form if the control volume is shrunk to an infinitesimal fluid element with volume δV, as follows

$$\frac{\Delta(\delta V)}{\Delta t} = (\nabla.\mathbf{v})\int_{V} d(\delta V) = (\nabla.\mathbf{v})\delta V \qquad (B.14)$$

Therefore, the divergence of the velocity is:

$$\nabla.\mathbf{v} = \frac{1}{\delta V}\frac{D(\delta V)}{Dt} \qquad (\mathrm{B}.15)$$

The RHS of Equation (B.15) physically interprets the divergence of the velocity. In the real sense, it represents the fact that $\nabla.\mathbf{v}$ is the time rate of change of the volume of a moving fluid element per unit volume.

B.1.5 The continuity equation

A moving fluid element with a fixed mass δm and a time - dependent volume δV is considered, where

$$\delta m = \rho \delta V \tag{B.16}$$

And ρ is the mass-density of the fluid. The mass conservation law will represent the change rate of δm, which will be zero where the element moves along the flow. The substantial derivative of the physical principle is introduced, where:

$$\frac{D(\delta m)}{Dt} = 0 \tag{B.17}$$

Here, the substantial derivative of (B.17) is by replacing the mass by the density and volume, i.e.

$$\frac{D(\delta m)}{Dt} = \frac{D(\rho \delta V)}{Dt} = \delta V \frac{D\rho}{Dt} + \rho \frac{D(\delta V)}{Dt} = 0 \tag{B.18}$$

After rearranging Equation (B.18) gives:

$$\frac{D\rho}{Dt} + \rho \frac{1}{\delta V} \frac{D(\delta V)}{Dt} = 0 \tag{B.19}$$

Where the second term in Equation (B.19) is the divergence of the velocity (see Equation B.15). Thus,

$$\frac{D\rho}{Dt} + \rho\nabla.\mathbf{v} = \mathbf{0} \qquad (B.20)$$

Equation (B.20) expresses the continuity equation or the mass conservation equation in a Lagrangian form.

B.1.6 The momentum equations

The momentum equations can be derived here, depending on the conservation of momentum. Newton's second law represents the physical principle (i.e. it is applied for very small fluid element moving with the flow), which states that the total force on a fluid element is equal to its mass times the acceleration of the fluid element considered. It can be treated as a moving fluid element, shown in figure B.2. Figure B.4 shows more details of the fluid element with the components of force in the x-direction.

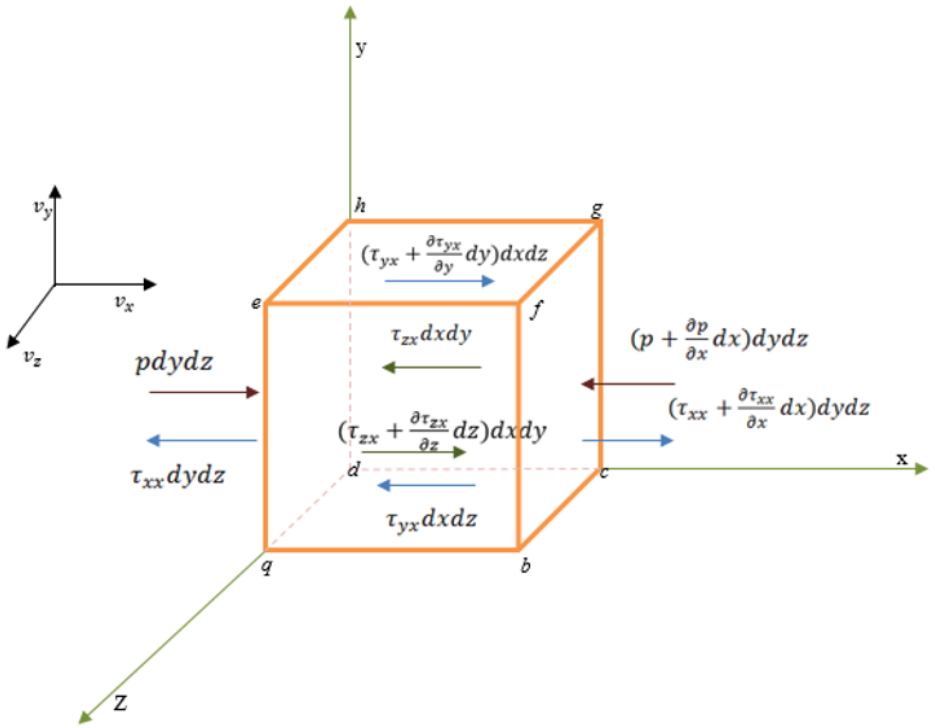

Figure B. 4 Forces applied on a fluid element with components of the force in the x-direction

The acceleration of the fluid element can be written as $\frac{Dv_x}{Dt}$, $\frac{Dv_y}{Dt}$, and $\frac{Dv_z}{Dt}$ in the directions x, y, and z, respectively; where the components of velocity in the same directions are v_x, v_y, and v_z, respectively.

There two sources of the force acting on the element, which is the body force ($\mathbf{F_b}$) and the surface force ($\mathbf{F_s}$).

- Body forces ($\mathbf{F_b}$) include the gravitational, electric, and magnetic forces which perform directly on the volumetric mass of the fluid.
- Surface forces ($\mathbf{F_s}$) act directly on the surface of the fluid element. The forces are divided into two types: the first type is the force of the outside fluid surrounding the fluid element, which is imposed by the pressure; and the second type is the shear and normal stress distributions on the surface, which are related to the time rate of change of the deformation of the element that results in a shear deformation and volume change, respectively.

In Figure B.4, the face *bfgc* represents the negative face of *x* while face *aehd* represents the positive face of *x*, where the x value for the face *dhgc* is less than that for the face *aefb*. Face *abed* represents the negative face of y and *ehgf* represents the positive face of *y*. The negative and positive faces of z are *hgcd* and *efba*. It can be seen here that the stress on the positive face is equal to the stress on the negative face in addition to the rate of change of that stress multiplied by the distance between the faces. An agreement can be reached here, whereby a stress will be positive when it is on the positive face in the positive direction, and it will be negative on the negative face in the negative direction. In addition, the shear stress τ_{ij} refers to the stress in the j-direction, which is exerted on a plane perpendicular to the i-axis.

The shear and normal stresses depend on the velocity gradients in the flow. In most viscous flows, normal stresses such as τ_{xx} are neglected for being much smaller than the shear stresses; however, because the normal velocity gradients such as $\frac{\partial v_y}{\partial x}$ are very large, the normal stresses have to be taken into account (such as the stresses inside a shock wave).

As mentioned above, all the forces acting on the infinitesimal fluid element in the x-direction are:

$$-\left[\left(P+\frac{\partial P}{\partial x}dx\right)-P\right]dydz+\left[\left(\tau_{xx}+\frac{\partial \tau_{xx}}{\partial x}dx\right)-\tau_{xx}\right]dydz+$$

$$\left[\left(\tau_{yx}+\frac{\partial \tau_{yx}}{\partial y}dy\right)-\tau_{yx}\right]dxdz+\left[\left(\tau_{zx}+\frac{\partial \tau_{zx}}{\partial z}dz\right)-\tau_{zx}\right]dxdy \qquad (B.21)$$

$$=-\frac{\partial P}{\partial x}dxdydz+\frac{\partial \tau_{xx}}{\partial x}dxdydz+\frac{\partial \tau_{yx}}{\partial y}dxdydz+\frac{\partial \tau_{zx}}{\partial z}dxdydz$$

Where *P* is the pressure force of the surrendering fluid.

According to Newton's second law, the body force in the x-direction is F_x:

$$m\frac{dv_x}{dt}=\rho dxdydz\frac{dv_x}{dt}=-\frac{\partial P}{\partial x}dxdydz+\frac{\partial \tau_{xx}}{\partial x}dxdydz$$

$$+\frac{\partial \tau_{yx}}{\partial y}dxdydz+\frac{\partial \tau_{zx}}{\partial z}dxdydz+F_x(\rho dxdydz) \qquad (B.22)$$

In addition, the momentum equation in the x-direction due to the Lagrangian approach is given by:

$$\rho\frac{Dv_x}{Dt}=-\frac{\partial P}{\partial x}+\frac{\partial \tau_{xx}}{\partial x}+\frac{\partial \tau_{yx}}{\partial y}+\frac{\partial \tau_{zx}}{\partial z}+\rho F_x\ . \qquad (B.23)$$

Similarly, the y and z components of momentum are written as:

$$\rho \frac{Dv_y}{Dt} = -\frac{\partial P}{\partial y} + \frac{\partial \tau_{xy}}{\partial x} + \frac{\partial \tau_{yy}}{\partial y} + \frac{\partial \tau_{zy}}{\partial z} + \rho F_y \qquad (B.24)$$

$$\rho \frac{Dv_z}{Dt} = -\frac{\partial P}{\partial z} + \frac{\partial \tau_{xz}}{\partial x} + \frac{\partial \tau_{yz}}{\partial y} + \frac{\partial \tau_{zz}}{\partial z} + \rho F_z \qquad (B.25)$$

Equations (B.23) to (B.25) are called the Navier-Stokes equations. Navier and Stokes independently found these equations in the first half of the nineteenth century.

The momentum Equations (B.23) to (B.25) can be written in a more compact form, which will consider the gravitational force on a particle only, as:

$$\frac{Dv}{Dt} = \frac{1}{\rho}\frac{\partial \sigma_{ij}}{\partial x_j} + \mathbf{g}\,. \qquad (B.26)$$

Here, the total stress tensor is in the first term of the RHS of Equation (B.26), which refers to two parts: the isotropic pressure *P* and the viscous stress $\boldsymbol{\tau}$, as follows:

$$\sigma_{ij} = -P\delta_{ij} + \tau_{ij}\,. \qquad (B.27)$$

Thus, a summary of the momentum conservation equations (governing equations) can be given as

$$\frac{D\mathbf{v}}{Dt} = -\frac{1}{\rho}\nabla P + \frac{1}{\rho}\nabla.\boldsymbol{\tau} + \mathbf{F}\,. \qquad (B.28)$$